Poznań University of Technology
Faculty of Computing and Telecommunications
Institute of Radiocommunications

Doctor of Philosophy Dissertation

New Two-Way Relaying Transmission Schemes for 5G Wireless Communication Systems

Nowe techniki transmisji dwukierunkowej przez stację przekaźnikową w systemach 5G

mgr inż. Karolina Lenarska

Supervisor: prof. dr hab. inż. Krzysztof Wesołowski

Poznań, 2024

In memory of my father, Jacek Ratajczak,
whose guidance and love shall remain with me always.

Abstract

Wireless communications is one of the fastest developing technologies in our time, with new products and services emerging on an almost daily basis. These developments present enormous challenges for communications engineers, as the demand for increased wireless capacity grows explosively.

One of the key technology components proposed to meet these expectations is the introduction of Relay Nodes (RN), which play an important role in 5G mobile networks. Relays have the ability to increase the reliability and capacity of the system while at the same time reducing operational costs. A particularly promising relay technology is bidirectional communication through the relay. The classic approach of the so-called two-way relaying involves two users exchanging messages; however, in the literature extended communication flows are also introduced such as MIMO Y channel that considers three users instead of two.

Due to the broadcast nature of the wireless medium, simultaneous transmission within the same frequency band from multiple transmitters to the relay, as well as multi-user transmission from the relay to all users inevitably result in interference among them. Consequently, effectively managing this interference at the receiver emerges as one of the primary challenges. This dissertation addresses the problem of interference management in the bidirectional communication through the relay by means of multiple antenna transmission (MIMO) with user-specific, advanced precoders and dedicated receivers.

First, a new method for the broadcast phase of two-way relaying is introduced, incorporating MU-MIMO with the proposed Maximum Ratio Transmission (MRT) and Codebook Maximum Ratio Transmission (CB-MRT) precoders, along with an interference cancelation receiver. Simulation results show that this advanced beamforming approach effectively reduces interference during the broadcast phase, achieving both low Block Error Rate (BLER) and high throughput. Furthermore, compared to the traditional network coding scheme, this new transceiver design offers flexibility in selecting modulation and coding schemes for each message and accommodating asymmetric traffic.

In the second research problem addressed in this dissertation, the focus shifts to a more advanced communication flow: the MIMO Y channel with a Signal Space Alignment (SSA) technique utilized in the multiple access phase. The SSA scheme, when combined with well-designed beamforming vectors, effectively aligns the data signals received by the relay to match its receiving capabilities. However, its robustness against an additional interference source, such as an adversarial jammer that intentionally interrupts legitimate transmissions, degrading reception performance, has not been considered in the literature.

This dissertation presents two antijamming strategies designed to mitigate the jammer signal at the relay. The first strategy introduces a new precoding algorithm, called Antijamming SSA (AJ-SSA), which projects the jamming signal and interference onto the null space of each signal pair. The second strategy, named Jammer's Interference Cancellation (J-IC), applies standard SSA at the transmitter and then removes jammer-induced interference at the relay by subtracting an estimate of the disturbance, based on minimizing received signal energy, from the incoming signal. The performance of these strategies in terms of BLER in various channel configurations is verified through link-level simulations, demonstrating their effectiveness in mitigating jamming signals in the SSA-based MIMO Y channel.

The author constructed the simulation package which models the physical layer of the 5G system and was used in simulation experiments to validate the proposed solutions. For that reason, the chapters containing the reports on the performed research have been preceded by the chapter introducing basic features of the 5G physical layer that are further needed in the investigations. It should be noted that the main results reported in this thesis have already been partially verified in the review process due to previous publications in the international journal and the international conference.

Streszczenie

Komunikacja bezprzewodowa jest jedną z najszybciej rozwijających się technologii naszych czasów z regularnie pojawiającymi się nowymi usługami i produktami. Ten dynamiczny rozwój stawia przed projektantami systemów bezprzewodowych znaczące wyzwania i niesie za sobą rosnące wymagania w zakresie przepustowości, niskiego opóźnienia i niezawodności sieci komunikacyjnych.

Jedną z kluczowych idei zaproponowanych w celu sprostania tym oczekiwaniom jest wprowadzenie stacji przekanikowych (ang. *Relay Nodes*, RN), które odgrywają istotną rolę w sieciach komórkowych 5G, ponieważ przyczyniają się do zwiększenia niezawodności i pojemności systemu, przy jednoczesnym obniżeniu kosztów operacyjnych. Szczególnie obiecującym wykorzystaniem przekaźników jest transmisja dwukierunkowa (ang. *Two Way Relaying*, TWR), w której dwie oddalone od siebie stacje wymieniają się wiadomościami za pośrednictwem stacji przekaźnikowej. W literaturze zaproponowo wiele rozszerzeń schematu TWR, w tym transmisję dwukierunkową z trzema stacjami nadawczymi, określaną jako schemat „MIMO Y".

Ze względu na specyfikę komunikacji bezprzewodowej, jednoczesna transmisja w tym samym paśmie częstotliwości od wielu stacji do przekaźnika, a także transmisja z przekaźnika do wszystkich użytkowników nieuchronnie prowadzi do wystąpienia zakłóceń między sygnałami różnych użytkowników. W związku z tym, efektywne zarządzanie interferencją staje się jednym z podstawowych wyzwań tego typu technik. Niniejsza dysertacja poświęcona została problemowi zarządzania interferencją w komunikacji dwukierunkowej przez przekaźnik poprzez wykorzystanie transmisji wieloantenowej (ang. *Multiple-Input-Multiple-Output*, MIMO), zaawansowanych technik prekodowania oraz korekcji sygnałów w odbiorniku.

W rozprawie przedstawiono dwie nowe metody realizacji fazy rozgłoszeniowej schematu TWR, bazujące na technice MU-MIMO (ang. *Multi-User MIMO*. Zaproponowano dwa algorytmy kodowania wstępnego - MRT (ang. *Maximum Ratio Transmission*) oraz CB-MRT (ang. *Codebook-MRT*) mające na celu ukształtowanie wiązek dedykowanych do każdej stacji odbiorczej w taki sposób, aby maksymalizować sygnał pożądany. Zakłócenia pochodzące od sygnału przeznaczonego dla drugiej stacji, usuwano w korektorze każdego odbiornika. Przeprowadzone badania pozwoliły na zwery-

fikowanie zaprezentowanej techniki transmisyjnej dla fazy rozgłoszeniowej schematu TWR i potwierdziły skuteczność zaproponowanych algorytmów.

Kolejnym zagadnieniem rozważanym w tej rozprawie jest wieloantenowa dwukierunkowa transmisja przez stację przekaźnikową z trzema użytkownikami (model MIMO Y), transmitującymi po jednej wiadomości do każdego z dwóch pozostałych użytkowników. Faza wielodostępu została zrealizowana z wykorzystaniem techniki SSA (ang. *Signal Space Alignment*), której zadaniem jest takie ukształtowanie sygnałów transmitowanych przez każdego użytkownika, aby w odbiorniku stacji przekaźnikowej nałożyły się one na siebie w taki sposób, by dopasować się do jego zdolności odbiorczych. Technika SSA z dobrze zaprojektowanymi wektorami prekodowania wstępnego efektywnie zarządza interferencją między użytkownikami, natomiast jej odporność na dodatkowe źródła zakłóceń nie była rozważana w literaturze. W związku z tym, w niniejszej rozprawie zaproponowano dwie strategie eliminacji interferencji pochodzącej od zewnętrznego urządzenia zakłócającego. W ramach pierwszego rozwiązania o nazwie AJ-SSA (ang. *Antijamming Signal Space Alignment*), wektory kodowania wstępnego oraz korektor w odbiorniku, zaprojektowane są w taki sposób, aby zarówno interferencja pochodząca od innych sygnałów danych jak i ta pochodząca od stacji zakłócającej zostały wyzerowane. W drugiej strategii o nazwie J-IC (ang. *Jammer's Interference Cancellation*) eliminacja zakłóceń pochodzących od stacji zewnętrznej odbywa się tylko w odbiorniku poprzez odjęcie estymaty sygnału zakłócającego. Jakość obu metod kompensacji wpływu zakłóceń mierzona poziomem BLER w różnych konfiguracjach została zweryfikowana za pomocą symulacji na poziomie łącza. Wyniki symulacji pokazują ich skuteczność w eliminacji wpływu sygnałów zakłócających w kanale MIMO Y.

Autorka skonstruowała pakiet symulacyjny, który modeluje warstwę fizyczną systemu 5G New Radio i który był używany w eksperymentach symulacyjnych mających na celu oszacowanie jakości proponowanych rozwiązań. Z tego powodu rozdziały, w których przedstawione są raporty na temat przeprowadzonych badań są poprzedzone rozdziałem wprowadzającym podstawowe własności warstwy fizycznej systemu 5G, które są następnie wykorzystywane w badaniach. Warto dodać, że główne wyniki przedstawione w tej rozprawie zostały już częściowo zweryfikowane w procesie recenzyjnym z powodu ich wcześniejszego przedstawienia w czasopiśmie międzynarodowym oraz na międzynarodowej konferencji o dużym zasięgu.

Acknowledgements

I would like to express my sincere gratitude to my supervisor, Professor Krzysztof Wesołowski, for his invaluable support and guidance throughout this dissertation. I am deeply thankful for the insightful feedback and encouragement, which played a significant role in the completion of my thesis.

I am also deeply grateful to my parents for instilling in me the importance of education and always encouraging my pursuit of knowledge. Their support has been the foundation of my journey.

A special thanks to my husband, for providing me with the space and support needed to complete this dissertation, despite the very demanding period in our lives.

Last but not least, I am deeply thankful to my three wonderful children, Zuzia, Lilka, and Karol - for being a constant source of love and motivation. They inspire me every day, and I hope that by completing this dissertation, I can one day inspire them in return.

Part of the work presented in this dissertation was carried out as part of the European Commission's Seventh Framework Program FP7-ICT under grant agreement No. 317669 also referred to as METIS (Mobile and Wireless Communications Enablers for the 2020 Information Society).

Contents

Acronyms

1G	1st Generation
2G	2nd Generation
3G	3rd Generation
3GPP	3rd Generation Partnership Project
4G	4th Generation
5G	5th Generation
5G-A	5G-Advanced
6G	6th Generation
AF	Amplify and Forward
AI	Artificial Intelligence
AMPS	Advanced Mobile Phone System
ANC	Analog Network Coding
ANs	Access Nodes
API	Application Programming Interface
ARQ	Automatic Repeat Request
ASN.1	Abstract Syntax Notation One
AWGN	Additive White Gaussian Noise
BC	Broadcast
BC	Broadcast Channel
BCH	Broadcast Channel
BD	Block Diagonalization
BER	Bit Error Rate
BLER	Block Error Rate
BS	Base Station
BWP	Bandwidth Part

CA	Carrier Aggregation
CB-MRT	Codebook-based Maximum Ratio Transmission
CO-MIMO	Cooperative MIMO
CoMP	Coordinated Multi-Point
CP	Cyclic Prefix
CP-OFDM	Cyclic Prefix OFDM
CQI	Channel Quality Indicator
CRBs	Common Resource Blocks
CRC	Cyclic Redundancy Check
CSI	Channel State Information
CSI-RS	Channel State Information Reference Signals
CSIT	Channel State Information at the Transmitter
D2D	Device-to-Device
DC	Dual Connectivity
DCI	Downlink Control Information
DeNB	Donor eNB
DF	Decode and Forward
DFT	Discrete Fourier Transform
DL-SCH	Downlink Shared Channel
DMRS	Demodulation Reference Signals
DOF	Degrees Of Freedom
DPC	Dirty Paper Coding
DSS	Dynamic Spectrum Sharing
EDGE	Enhanced Data rates for GSM Evolution
eMBB	Enhanced Mobile Broadband
eNB	evolved Node B
EPA	Extended Pedestrian A model
FD	Full Duplex
FDD	Frequency Division Duplex
FFT	Fast Fourier Transform
FR1	Frequency Range 1
FR2	Frequency Range 2
FSTD	Frequency Switched Transmit Diveristy

gNB	5th generation Node B
GPRS	General Packet Radio Service
GSA	Generalized Signal Alignment
GSM	Global System for Mobile communication
HARQ	Hybrid ARQ
HD	Half Duplex
HSPA	High Speed Packet Access
IA	Interference Alignment
IAB	Integrated Access and Backhaul
IC	Interference Cancellation
IMT	International Mobile Telecommunications
IoT	Internet of Things
ITU-R	ITU Radiocommunication Sector
LDPC	Low Density Parity Check
LTE	Long-Term Evolution
LTE-A	LTE-Advanced
MA	Multiple Access
MAC	Medium Access Control
MAC	Multiple-Access Channel
MBS	Multicast and Broadcast Service
MF	Matched Filter
MIMO	Multiple-Input Multiple-Output
MinIL	Minimizing Interference Leakage
MISO	Multiple-Input Single-Output
ML	Machine Learning
ML	Maximum Likelihood
MMSE	Minimum Mean Square Error
mMTC	massive Machine Type Communication
MRT	Maximum Ratio Transmission
MS	Mobile Station
MSE	Mean Squared Error
MTC	Machine-Type Communication
MU-BDBF	Multi User Block Diagonalization Beamforming

MU-MIMO	Multi-User Multiple Input Multiple Output
NB	Node B
NC	Network Coding
NMT	Nordic Mobile Telephony
NR	New Radio
NSA	Non-Standalone
NTN	Non-Terrestial Network
OFDM	Orthogonal Frequency-Division Multiplexing
OFDMA	Orthogonal Frequency-Division Multiple Access
PCH	Paging Channel
PDCP	Packet Data Convergence Protocol
PDSCH	Physical Downlink Shared Channel
PDU	Protocol Data Unit
PHY	Physical
PLMN	Public Land Mobile Network
PMI	Precoding Matrix Index
PNC	Physical-Layer Network Coding
PRB	Physical Resource Block
PRBs	Physical Resource Blocks
PUSCH	Physical Uplink Shared Channel
QoS	Quality of Service
RAN	Radio Access Network
RedCap	Reduced Capability
RI	Rank Indicator
RLC	Radio Link Control
RN	Relay Node
RNs	Relay Nodes
RS	Relay Station
RV	Redundancy Version
SA	Standalone
SC-FDMA	Single-Carrier Frequency-Division Multiple Access

SDAP	Service Data Adaptation Protocol
SFBC	Space-Frequency Block Codes
SINR	Signal to Interference and Noise Ratio
SISO	Single-Input Single-Output
SMS	Short Message Service
SNR	Signal-to-Noise-Ratio
SRI	SRS Resource Indicator
SRS	Sounding Reference Signal
SSA	Signal Space Alignment
STBC	Space-Time Block Codes
SU-MIMO	Single-User Multiple Input Multiple Output
SVD	Singular Value Decomposition
TDD	Time Division Duplex
TTI	Transmission Time Interval
TWR	Two-Way Relaying
UDNs	Ultra-Dense Networks
UE	User Equipment
UEs	User Equipments
UL-SCH	Uplink Shared Channel
UMTS	Universal Mobile Telecommunications System
URLLC	Ultra Reliable Low Latency Communication
V2X	Vehicle-To-Everything
VRB	Virtual Resource Block
VRBs	Virtual Resource Blocks
WCDMA	Wideband Code Division Multiple Access
XR	eXtended Reality
ZF	Zero Forcing
ZFBF	Zero Forcing Beamforming

Chapter 1

Introduction

The evolution of mobile communication systems revolutionized the way people communicate and exchange information.

The first generation of mobile communication (1^{st} Generation (1G)) emerged in the mid-1980s, carried mainly voice and was based on analog transmission with the main standards being Advanced Mobile Phone System (AMPS) in the USA and Nordic Mobile Telephony (NMT) in Scandinavia.

The second generation of cellular communication (2^{nd} Generation (2G)) replaced analog transmission with the first digital communication scheme in the mid to late 1990s. Initially, there were several different second-generation technologies, including Global System for Mobile communication (GSM) in Europe and digital-AMPS in the US, but as time went by, GSM became a dominant standard. At that time, Short Message Service (SMS) was introduced, being the first widely used non-voice application in the mobile network. In order to support higher data rate, an upgrade in GSM was made, which introduced the packet network and became known as 2.5G. The standards included General Packet Radio Service (GPRS) and Enhanced Data rates for GSM Evolution (EDGE).

The third generation of mobile communication (3^{rd} Generation (3G)) was introduced in the early 2000 by the 3^{rd} Generation Partnership Project (3GPP) consortium, The 3G Universal Mobile Telecommunications System (UMTS) standard exploited Wideband Code Division Multiple Access (WCDMA) technology in the 5 MHz bandwidth. The 3G technology enabled fast wireless Internet access (High Speed Packet Access (HSPA)) and with some advances in mobile user equipment added multimedia facilities to 3G phones by allowing video, audio and graphics applications to be transmitted over the network.

The fourth generation (4^{th} Generation (4G)) of mobile communication is represented by the Long-Term Evolution (LTE) technology. Initiated in 2009, when the first technical specification was released, it is an IP-based network system that exploits Or-

thogonal Frequency-Division Multiplexing (OFDM)-based transmission. OFDM provides wider transmission bandwidths and more advanced multi-antenna techniques that allow high speed, high quality, and high capacity to users while improving security and reducing the cost of voice, data services, multimedia, and the Internet over IP. LTE-Advanced (LTE-A) which is an extension of LTE introduced further enhancements such as carrier aggregation, heterogeneous network deployments, and improved support for Coordinated Multi-Point (CoMP). LTE was the first global technology for mobile communication, used by all mobile network operators that prevailed as the dominant cellular network standard and has become the basis of the transition to 5^{th} Generation (5G) mobile communications.

The standardization work on the fifth generation of mobile communication (5G) began around 2012, when ITU Radiocommunication Sector (ITU-R) started a program called "IMT for 2020 and beyond" to develop the requirements for a 5G mobile communications air interface. To meet these requirements, 3GPP initiated work on a new radio access technology, called the 5G New Radio (New Radio (NR)). Fig. 1.1 presents the timeline of the 5G development within the 3GPP consortium. The 3GPP's submission to IMT-2000 included functionalities from both Release 15 and Release 16, which the ITU-R approved as 5G technology in 2020. The technical work on NR started in the spring of 2016 as a part of Release 14, and was preceded by a workshop in the fall of 2015. The work continued in Release 15, giving the first version of the NR specifications ready by the end of 2017. In Release 15, 3GPP introduced a new 5G air interface (NR), designed to support use cases ranging from Enhanced Mobile Broadband (eMBB) to Ultra Reliable Low Latency Communication (URLLC) and massive Machine Type Communication (mMTC). NR accommodates both Non-Standalone (NSA) mode, which uses LTE for initial access and mobility management, and the Standalone (SA) mode, which operates independently of LTE. Key features of NR include high frequency operation, spectrum flexibility, low latency capabilities, ultra-lean design, forward compatibility, advanced antenna technologies, and more.

Release 16 marks the first phase in the evolution of 5G, bringing significant enhancements that not only refine existing features, but also support new use cases and deployment scenarios. Key improvements to existing features include enhanced Dynamic Spectrum Sharing (DSS), reduced latency in Dual Connectivity (DC) and Carrier Aggregation (CA), advances in Multiple-Input Multiple-Output (MIMO) and beamforming, and better power savings for user equipment (UE). The new use cases and deployment scenarios addressed in Release 16 include operation in unlicensed spectrum, enhanced support for industrial Internet of Things (IoT) and URLLC, positioning services, Vehicle-To-Everything (V2X) communications and Integrated Access and Backhaul (IAB).

The work on the 5G system continued in Release 17, which includes enhancements to existing features such as User Equipment (UE) power saving, DSS, MIMO, cov-

erage, positioning, and URLLC. The major new use cases and deployment scenarios in Release 17 include support for Reduced Capability (RedCap) UE, extending NR operation up to 71 GHz, Multicast and Broadcast Service (MBS) and Non-Terrestial Network (NTN)s.

Release 18 marks the beginning of the work on 5G-Advanced (5G-A) and acts as a bridge between 5G and 6G. Its final stage-2 specification was finalized in June 2023, the protocol design was finalized in March 2024. The Open Application Programming Interface (API) and Abstract Syntax Notation One (ASN.1) will be released in June 2024. Release 18 enhances local networking capabilities by supporting local access for roaming UE, inter Public Land Mobile Network (PLMN) edge server access, and the selection of a common edge service server. Additionally, Release 18 improves network slicing by allowing third-party use of slices based on factors such as the maximum number of UEs accessing the network, load prediction, and time restrictions. The latest release also provides systematic support for immersive eXtended Reality (XR) and multimedia services by offering application-layer parameters to assist RAN scheduling, power savings for XR services and capacity improvements covering improvements to resource allocation and scheduling for XR services to support multi-modality flows and reduce jitter. 5G-A provides also an intelligent network platform that utilizes Artificial Intelligence (AI) / Machine Learning (ML) for the NR air interface. The initial set of use cases for AI/ML-based algorithms include Channel State Information (CSI) feedback enhancement, beam management, and positioning accuracy [1]. Release 18 is considered the first phase of 5G Advanced, builds on the existing 5G standard defined in Releases 15, 16, and 17. 5G Advanced will then continue to evolve up to Release 20, expected in 2027.

As the journey to evolve 5G-Advanced begins, research on the 6^{th} Generation (6G) of mobile communications is accelerating. The International Telecommunication Union (ITU) has released the framework for developing standards and radio interface technologies for the sixth generation of mobile systems, known as 6G. The specifics of this 6G framework are detailed in Recommendation ITU-R M.2160, entitled "IMT-2030 Framework" [2]. This recommendation was approved during the ITU Radiocommunication Assembly (RA-23) meeting in Dubai, United Arab Emirates, in November 2023. The IMT-2030 Framework Recommendation specifies 15 capabilities for 6G technology, nine of these originating from existing 5G systems. The standardization of 6G is anticipated to begin in 3GPP around 2025 as a part of Release 20.

1.1 Introduction to the topics considered in the thesis

Mobile connectivity continues to play a crucial role in fostering digital innovation, providing individuals, businesses, and governments with transformative technologies that generate positive social impacts. By the end of 2023, 5.6 billion people (69% of

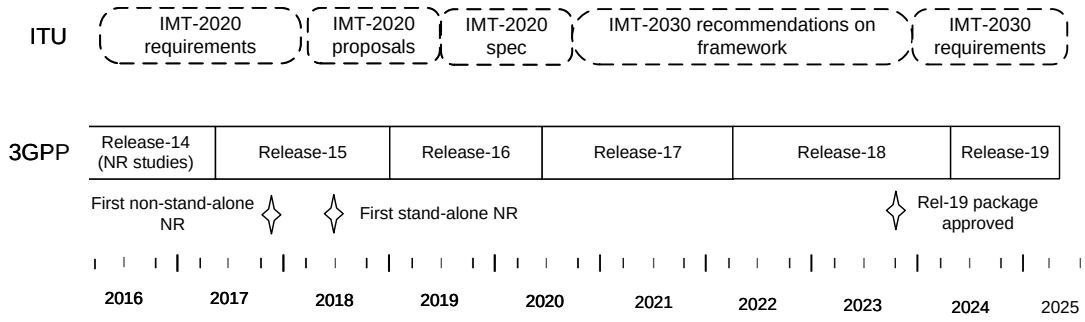

Figure 1.1: 3GPP timeline

the global population) were subscribed to mobile services, marking an increase of 1.6 billion since 2015. Mobile internet penetration has grown even more rapidly, with 4.7 billion users (58% of the global population) by 2023, an increase of 2.1 billion since 2015. Although high-income countries have largely reached saturation, substantial growth potential remains in low- and middle-income countries. As a result, global mobile subscriptions are expected to reach 6.3 billion by 2030, covering 74% of the population. In addition, 5G connections are predicted to increase from 1.6 billion in 2023 to 5.5 billion by 2030 [3]. The latest report also reveals that 5G will become Europe's dominant mobile technology within the next three years, driven by uptake in Germany and the UK. By 2030 5G is expected to reach 87% of all users.

One of the primary challenges in addressing the demands of future services and markets is the scarcity of available radio resources. Digital communication using MIMO systems is one of the most significant technical breakthroughs in modern communication that cope with both the impairments in wireless channels and the constraints of resources. In addition to the time and frequency dimensions that are exploited in conventional single antenna (Single-Input Single-Output (SISO)) wireless systems, the leverages of MIMO are realized by exploiting the spatial dimension (provided by the multiple antennas at a transmitter and a receiver). Communication theories show that MIMO systems can provide a potentially very high capacity that, in many cases, grows approximately linearly with the number of antennas. MIMO technology has been a subject of research since the last decade of the twentieth century and has become an essential element of wireless communication standards including IEEE 802.11n (Wi-Fi), IEEE 802.11ac (Wi-Fi), HSPA+ (3G), WiMAX (4G), LTE (4G) and NR (5G).

Another technology component that can help overcome the problem of limited radio resources in mobile networks is the concept of Relay Nodes (RNs). The idea of relay nodes was first considered as an information-theoretical scenario, where an upper bound was determined for the capacity of the relay channel. The 3GPP consortium incorporated relays in Release 10 of the LTE standard and since then relays

have played an important role in next-generation 5G mobile networks. Low power RNs improve system reliability and capacity while reducing operational costs. Relays enhance the link between the base station and user equipment by providing additional spatial diversity, which when exploited at the receiver, increases transmission reliability. Relays at the cell borders fill coverage gaps and extend coverage, while those within the cell increase capacity. They also help offload traffic by balancing loads between congested and less congested cells. Additionally, deploying low-power relays lowers operational costs, as they reduce power requirements due to shorter transmission distances and provide a cost-effective way to extend coverage without the need for backhaul installation.

A particularly promising RNs technology that has been proposed in the literature and investigated to satisfy high end-user requirements is Two-Way Relaying (TWR). In a two-way communication channel, two end nodes exchange messages through the relay. Numerous transceiver designs have been investigated to maximize the throughput of such a system model. Among all proposed schemes, Network Coding (NC), where the relay combines the received messages before sending them, gained particular interest. Network coding improves bandwidth efficiency and reduces the number of required transmissions. However, several challenges arise, including error propagation, as errors in one of the messages may propagate through the network due to combined transmission, making error correction challenging. Moreover, network coding imposes an equal data requirement, that is, both nodes need to exchange data of equal size, limiting flexibility when asymmetric traffic is present. In addition, NC forces the modulation and coding scheme to be the same for both messages and determined according to the weakest link, resulting in a lower achievable data rate.

This dissertation addresses the challenge of developing a flexible two-way relaying scheme that maintains comparable performance while overcoming the limitations associated with network coding. Motivated by the above, the author of this dissertation proposes a new transceiver design for a TWR scheme, where, by exploiting multiple antennas in the relay, the Multi-User Multiple Input Multiple Output (MU-MIMO) technique is employed and novel precoding techniques are introduced. The proposed solution provides flexibility in selecting different modulation and coding schemes and data block sizes, thus supporting asymmetric traffic.

Relaying techniques have gained recognition for their effectiveness in improving the reliability and throughput of wireless networks. To support more than two users in the two-way relay channel, the concept of a three-user relay channel, known as the MIMO Y channel, was introduced. Alongside this, a new signaling scheme, called Signal Space Alignment (SSA), was proposed for the multiple access phase. SSA enhance network capacity by allowing multiple MIMO transmitters to transmit data simultaneously. Using calculated precoding, SSA reduces the perceived signal space in

a relay to match its receivng capability, allowing the demodulation of linearly combined data packets.

As our dependence on wireless services increases, concerns about privacy, reliability, and accessibility in wireless communications have become increasingly prominent. Among various security threats, including eavesdropping and data fabrication, wireless networks are especially vulnerable to radio jamming attacks. The goal of an adversarial jammer is to create interference signals that intentionally disrupt legitimate wireless transmission and decrease reception quality. During recent decades, considerable effort has been devoted to developing antijamming strategies to reduce the impacts of jamming and ensure uninterrupted legitimate transmission.

The SSA for the MIMO Y channel is a prospective technique for interference management, but despite the substantial advances in the SSA scheme, its resilience to jamming attacks has not been thoroughly explored. This dissertation looks at the challenge of achieving reliable and efficient transmission in the MIMO Y channel in the presence of an adversarial jammer. Two novel antijamming strategies are proposed and compared.

1.2 Problem statements and theses formulation

The author of this dissertation has investigated two problems, namely:

- multiple-antenna two-way relaying with network coding versus MU-MIMO with proposed precoding algorithms in broadcast phase
- antijamming strategies for MIMO Y channel

Consequently, the theses of this dissertation can be formulated as follows:

1. **User-specific beamforming together with advanced receivers can be efficiently used in terms of achievable Block Error Rate (BLER) and throughput, for interference mitigation in the broadcast phase of two-way relaying, with the ability to support asymmetric traffic and flexible selection of transport layer parameters for each link.**

2. **User-specific beamforming together with advanced receivers can efficiently eliminate the interference originating from the jammer maintaining lower computational complexity than the well-known Interference Cancellation (IC) receiver.**

1.3 Outline of Contents

The content of the thesis is the following. After the introductory chapter, our attention is directed in Chapter 2 to an overview of 5G mobile and wireless communication systems, focusing on key components such as rate matching, scrambling, modulation, and precoding for uplink and downlink. Multiple-antenna systems, resource mapping, and relay technologies are also discussed, highlighting their classification, benefits, and applications in 5G networks. The reason for this 5G system overview is to sketch the landscape in which the problems considered in this dissertation are addressed.

The discussion then shifts in Chapter 3 to two-way relaying transmission schemes, where network coding, physical-layer network coding, and signal space alignment techniques are introduced. These methods are crucial to improving the efficiency of data exchange in relay-based systems.

Following this, in Chapter 4 the thesis delves into Maximum Ration Transmission (MRT) precoding for two-way relaying, including an analysis of related works, the system model, and key transmission phases such as the multiple access phase and the broadcast phase. Various equalization methods, network coding, and Multi-User Multiple-Input Multiple-Output (MU-MIMO) transmission are examined. Particular attention is paid to MRT precoding. Chapter 4 also includes detailed simulation results for different transmission phases.

In Chapter 5, antijamming schemes for generalized MIMO Y channels are explored, including an in-depth look at the system model and various jamming suppression techniques. These antijamming strategies are analyzed for multiple access along with their computational complexity. The effectiveness of the proposed algorithms is demonstrated by the simulation results.

Finally, the thesis concludes in Chapter 6 by summarizing the main findings and suggesting potential directions for future research.

Chapter 2

The 5G mobile and wireless communication systems

2.1 5G overview

The purpose of the 5G system overview is to sketch the basic features of the systems to such an extent that a description of the new ideas presented in this thesis is possible.

2.1.1 5G usage scenarios

Three usage scenarios for the 5G system were defined by ITU-R and became part of International Mobile Telecommunications (IMT) Vision recommendation [4]:

- eMBB corresponds to extremely high data-rate communications with extremely high coverage.
- mMTC enables wireless connectivity between a massive number of devices and efficient transmission of small messages in wide area.
- URLLC corresponds to services that require very low latency and extremely high reliability, such as V2X communication and factory automation.

The usage scenarios are illustrated in Fig. 2.1. Generic services may use different air interfaces, depending on service requirements. The three above use cases are not meant to cover all possible scenarios, but they group a majority of all current use cases and thus may be used to find the key capabilities needed for next generation radio interface technology for IMT-2020 [5].

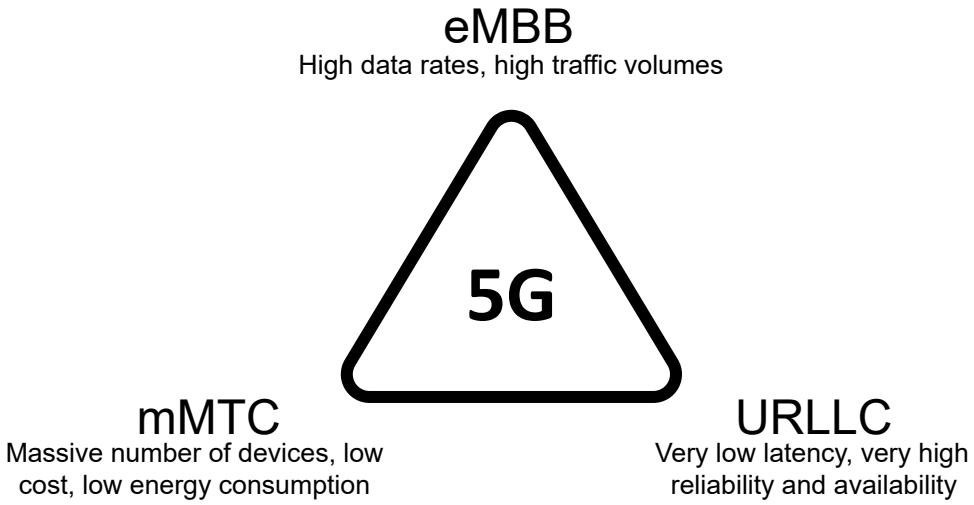

Figure 2.1: High-level 5G use-case classification [5]

2.1.2 IMT-2020 requirements

Apart from the generic use cases, a set of 13 capabilities needed to support these use cases was defined by ITU-R in the IMT Vision recommendation [4]. Eight of them were selected as "key capabilities" and are shown in Fig. 2.2. Each key capability is characterized by the absolute indicative target number or relative values corresponding to the capabilities of the IMT-Advanced system (4G). ITU-R does not require simultaneously reaching all target values of each key capability, since different subsets of key capabilities are important for different use cases defined by ITU-R.

Based on the scenarios and usage capabilities presented in the IMT Vision recommendation, ITU-R [6] proposed a set of minimum technical performance requirements. These requirements were supposed to be used as a baseline for candidates for 5G technology. Table 2.1 presents 14 minimum technical requirements taken from ITU-R document [6].

2.1.3 Frequency bands for NR

5G system needs to handle demanding eMBB usage scenarios and related new services that require very high data rates and capacity in dense deployments. To meet these requirements, besides the bands used for previous generations, the fifth generation will also support very high frequencies, from below 1 GHz up to 52.6 GHz. The main reason for this is the large amount of spectrum with large bandwidths available in the range of several GHz. Although using the millimeter-wave spectrum seems very attractive, it comes with a price of new propagation challenges such as lower system coverage due to substantial transmission loss, which is frequency dependent, or degradation of RF hardware performance in terms of phase noise and output power. Thus, operation in lower-frequency bands remains indispensable. Moreover, substantial benefits can be

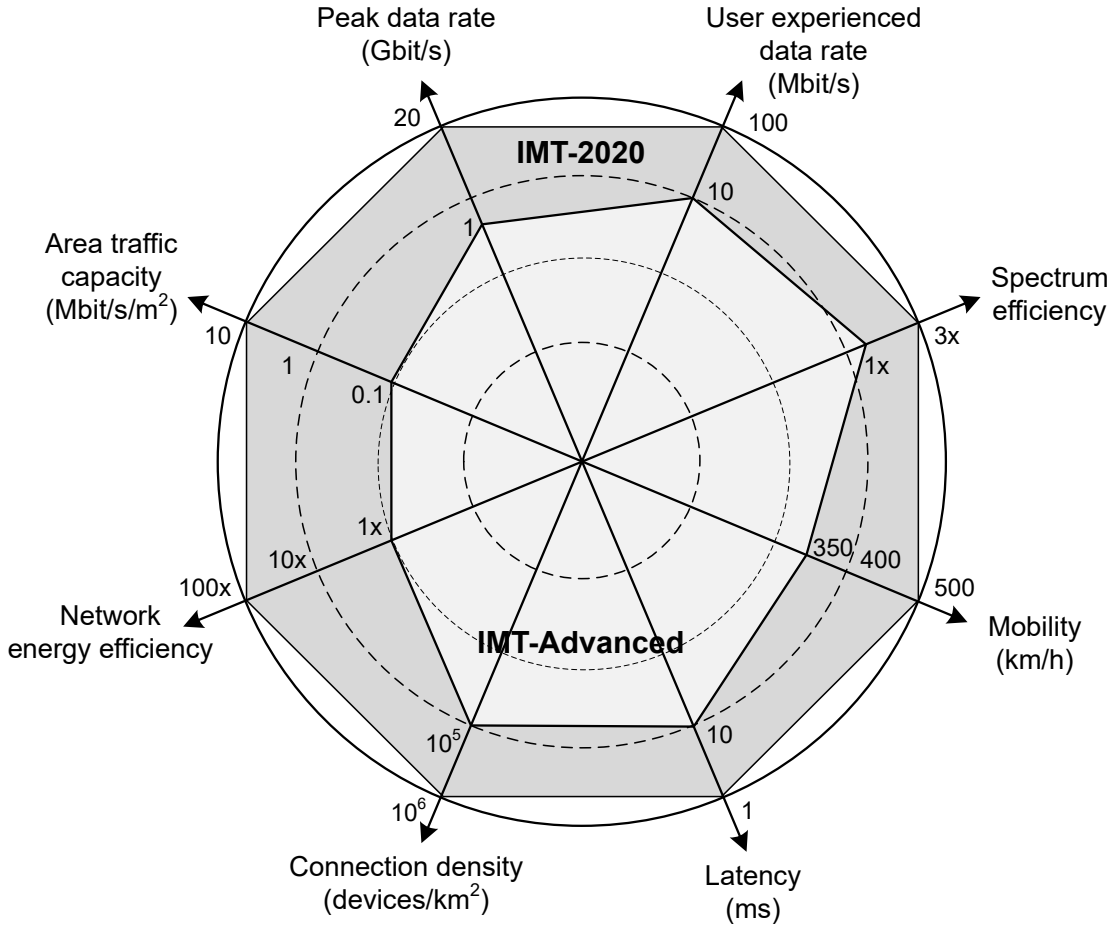

Figure 2.2: Key capabilities of IMT-2020 [5]

provided, when joint operation in lower and higher frequency is performed. In general, the 3GPP Release 18 divides all frequency bands into two ranges:

- Frequency Range 1 (FR1) – frequency range 410–7125 MHz
- Frequency Range 2 (FR2):
  - FR2–1 – frequency range 24250–52600 MHz
  - FR2–2 – frequency range 52600–71000 MHz

2.1.4 5G key technology components

To meet the IMT recommendations for the 5G network, new technologies were required. Some of them are extensions of the 4G system technologies, and some were developed explicitly for 5G. The technologies being developed for 5G and 5G-Ainclude:

- **Millimeter-Wave communications** – as mentioned in Section 2.1.3, using millimeter-waves provides the possibility of having a much wider channel bandwidth (even up to 2 GHz).

Table 2.1: Overview of Minimum Technical Performance Requirements for IMT-2020 [5]

Parameter	Minimum Technical Performance Requirement
Peak data rate	Downlink: 20 Gbit/s
	Uplink: 10 Gbit/s
Peak spectral efficiency	Downlink: 30 bit/s/Hz
	Uplink: 10 bit/s/Hz
User-experienced data rate	Downlink: 100 Mbit/s
	Uplink: 50 Mbit/s
Fifth percentile spectral efficiency	3 × IMT-Advanced
Average spectral efficiency	3 × IMT-Advanced
Area traffic capacity	10 Mbit/s/m^2
User plane latency	4 ms for eMBB
Control place latency	20 ms
Connection density	1000000 devices per km^2
Energy efficiency	Related to two aspects for eMBB:
	a. Efficient data transmission in a loaded case
	b. Low energy consumption when there is no data
	The technology shall have the capability to support a high sleep ratio and long sleep duration
Reliability	$1 - 10^{-5}$ success probability of transmitting a layer 2 Protocol Data Unit (PDU) of 32 bytes within 1 ms, at coverage edge in Urban Macro for URLLC
Mobility	Normalized traffic channel data rates defined for 10, 30 and 120 km/h at $\sim$ 1.5× IMT-Advanced numbers
	Requirement for high-speed vehicular defined for 500 km/h (compared to 350 km/h for IMT-Advanced)
Mobility interruption time	0 ms
Bandwidth	At least 100 MHz and up to 1 GHz in higher-frequency bands. Scalable bandwidth shall be supported

- **Beamforming** – is an attractive method to improve the performance of the mobile network. Although it has been researched for many years, it was not included in the initial LTE specifications of 3GPP Release 8. However, beamforming was incorporated into the 5G specifications starting with 3GPP Release 15. The advantages of beamforming are realized in practice through the use of massive MIMO technology. Massive MIMO extends traditional MIMO technology to antenna arrays with a large number of controllable transmitters, which 3GPP defines as more than eight of them. Compared to LTE, the 5G system offers greater gains through beamforming, as it supports beam sweeping for common channels, user-specific reference signals that allow for user-specific beamforming, lacks legacy device constraints, and supports more transmission branches.

- **Waveforms** – Orthogonal Frequency-Division Multiple Access (OFDMA) was chosen as a basic transmission scheme for both downlink and uplink of 5G system. The Single-Carrier Frequency-Division Multiple Access (SC-FDMA) option, fre-

quently called DFT-spread OFDM, is also included in 5G uplink for maximum coverage.

- **Ultra-dense network** – is another promising solution to increase the network capacity. The density of access nodes in 5G system is expected to reach the value comparable to the density of user equipment or even exceed it. Ultra-Dense Networks (UDNs) will be deployed both outdoors and indoors, with the range down to a few meters. Realization of such challenging concept will be achieved by utilizing user deployed Access Nodes (ANs) (e.g. Wi-Fi, femtocells), as well as mobile devices that thanks to their computational and storage capabilities will act as infrastructure ANs ("infrastructure prosumers" User Equipments (UEs)) (Fig. 2.3). UDNs operating in cm-wave and mm-wave bands will meet the requirement of high (local) area capacity and high throughput, enabling data rates on the order of 10 Gbps.

- **Network Slicing** – 5G networks are designed to support a wide range of diverse and extreme requirements for latency, throughput, capacity, and availability. Network slicing provides a way to address the needs of various use cases within a common network infrastructure. The network slice is a logically separated, self-contained, independent, and secured part of the network, targeting different services with specific requirements on speed, latency, and reliability. The slicing principles in 5G allow a UE to belong to more than a single slice, while still maintaining only a single signaling connection with a network.

- **Relays** – have been introduced in Release 10 of the LTE standard and play an important role in next-generation 5G mobile networks. Relaying is a powerful technique that can be promising in the following applications: provisioning of wireless backhaul in UDNs, wireless backhauling for nomadic nodes, supporting Device-to-Device (D2D) links, and improving the network performance, providing sufficient coverage for mm-wave communication and traffic aggregation in Machine-Type Communication (MTC). Relaying technology in the context of 5G networks is the main topic of this dissertation, and thus it is presented in detail in the later part of this chapter (see Section 2.4).

2.2 NR physical layer overview

The physical layer is responsible for channel coding, hybrid-ARQ processing, modulation, multi-antenna processing, and mapping of the signal to the appropriate physical time-frequency resources. Since NR has to support a wide range of spectrum (being the first mobile system operating in the mm-wave frequency range) and use cases with

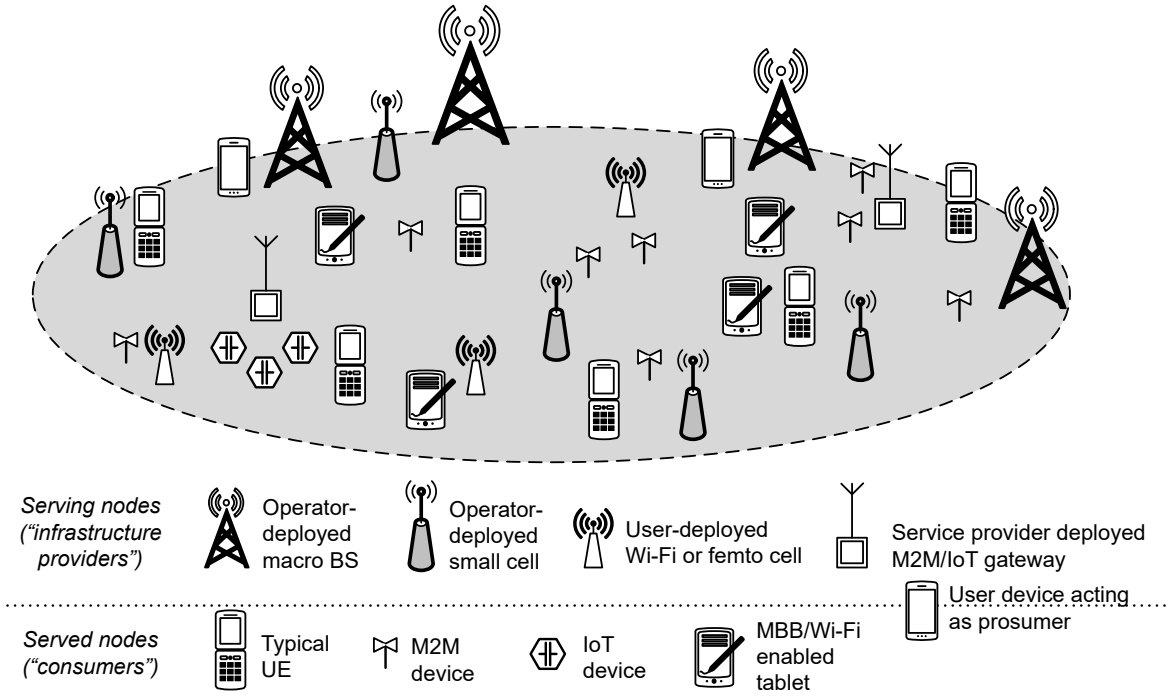

Figure 2.3: A UDN infrastructure composed by operator- and user-deployed heterogenous serving access nodes (ANs), multiple types of user and machine served nodes, and disruptive devices acting as prosumers [7]

extreme and sometimes contradictory requirements, its physical layer has to be flexible. This section provides an overview of the physical layer NR based on Release 18 of 3GPP NR that was published in March 2024 [8].

2.2.1 Radio protocol architecture

The radio protocol architecture for NR consists of a control-plane architecture, responsible for the connection setup, mobility, and security, and a user-plane architecture whose main task is to deliver user data. According to 3GPP terminology, 5th generation Node B (gNB) is an implementation of the logical radio access network in the 5G NR system. In 3G UMTS and 4G LTE the network nodes were termed Node B (NB) and evolved Node B (eNB), respectively. The user plane protocol stack is presented in Fig. 2.4 and can be separated into the following layers: Physical (PHY) layer, Medium Access Control (MAC) layer, Radio Link Control (RLC) layer, Packet Data Convergence Protocol (PDCP) layer, and Service Data Adaptation Protocol (SDAP) layer. The PHY layer is responsible for channel coding, modulation, multi-antenna processing, and resource mapping. The Multiple-Access Channel (MAC) layer handles error correction in the Hybrid ARQ (HARQ) mechanism, uplink/downlink scheduling, and multiplexing data across multiple carriers in the carrier aggregation technique. The RLC layer is responsible for error correction in the Automatic Repeat Request (ARQ) mechanism, segmentation of IP packets, and in-sequence delivery of data units to

higher layers. The PDCP layer handles IP header compression, ciphering, integrity protection, reordering, and duplicate detection. The SDAP layer is responsible for mapping IP packets to radio bearers according to their Quality of Service (QoS) requirements [9].

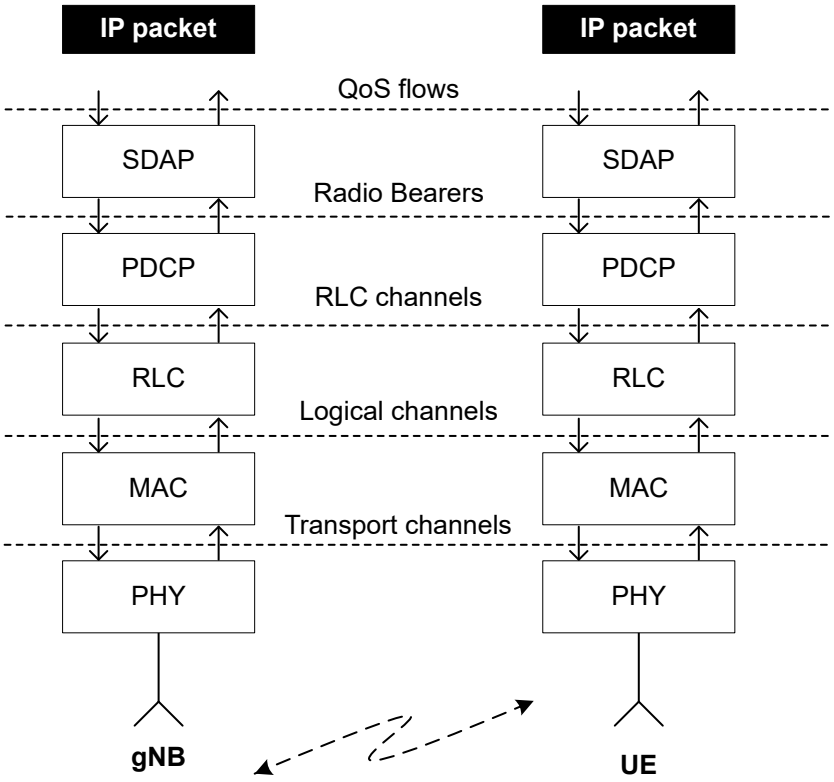

Figure 2.4: NR user-plane protocol stack [9]

2.2.2 Waveform

NR employs Cyclic Prefix OFDM (CP-OFDM) as the basic transmission scheme for both downlink and uplink, unlike LTE, where Discrete Fourier Transform (DFT)-spread OFDM was used for uplink transmissions. Having the same waveform in both directions simplifies the overall design in particular in the case of wireless backhauling and D2D. However, to reduce cubic metric and obtain higher power-amplifier efficiency in uplink single stream transmissions, the DFT-spread OFDM may be used.

Since NR is designed to enable diverse services in a wide range of frequencies, 3GPP proposed a scalable numerology with a range of subcarrier spacings, specified as 15×2^n (where n is an integer), as shown in Table 2.2. The choice of a baseline subcarrier spacing equal to 15 kHz ensures compatibility with the LTE system. For each of the specified subcarrier spacing, Cyclic Prefix (CP) overhead is equal to 7% (the same as in LTE). For 60 kHz numerology, an extended CP is also defined. Each proposed subcarrier spacing is dedicated to different frequency bands; however, since currently there is no spectrum identified for NR in the range between 7.125 and 24.25 GHz, the

corresponding numerology was not defined. For all proposed subcarrier spacing, the number of active subcarriers is 3300, thus the maximum bandwidths available in each numerology are different and range from 50 MHz for 15 kHz spacing up to 2000 MHz for 960 kHz. To further increase the bandwidth, carrier aggregation can be used. The 240 kHz subcarrier spacing is reserved for L1 control information.

Table 2.2: Scalable OFDM numerology for 5G NR [8]

OFDM numerology	15 kHz	30 kHz	60 kHz	120 kHz	240 kHz	480 kHz	960 kHz
Frequency band	FR1	FR1	FR1, FR2-1	FR2-1	N/A	FR2-1, FR2-2	FR2-2
OFDM symbol duration [μs]	66.67	33.33	16.67	8.33	4.17	2.08	1.04
Cyclic prefix duration [μs]	4.69	2.34	1.17	0.59	0.3	0.15	0.07
OFDM symbol with CP [μs]	71.35	35.68	17.84	8.91	4.46	2.23	1.12
Maximum bandwidth [MHz]	50	100	200	400	N/A	1600	2000

2.2.3 Duplexing scheme

NR supports both Time Division Duplex (TDD) and Frequency Division Duplex (FDD), depending on the spectrum allocation. At lower-frequency bands, spectrum allocations are often paired, implying FDD, whereas at higher frequencies, unpaired spectrum allocations are increasingly common, implying TDD. In order to enable following rapid traffic variations in dense deployments, NR supports dynamic TDD, where assignment of time-domain resources for downlink and uplink can be changed over time, taking into account current needs. Dynamic TDD is one of the key NR technology components that was not available in previous 3GPP releases. TDD can also be set as semi-static, with predefined uplink/downlink switching periodicities, depending on the applied OFDM numerology (Table 2.3).

Table 2.3: Semi-static TDD periodicities [10]

OFDM numerology	Uplink/downlink switching periodicities [ms]
15 kHz	0.5, 1, 2, 5, 10
30 kHz	0.5, 1, 2, 2.5, 5, 10
60 kHz	0.5, 1, 1.25, 2, 2.5, 5, 10
120 kHz	0.5, 0.625, 1, 1.25, 2, 2.5, 5, 10
240 kHz	0.5, 1, 2, 5
480 kHz	0.5, 0.625, 1, 1.25, 2, 2.5, 5, 10
960 kHz	0.5, 0.625, 1, 1.25, 2, 2.5, 5

2.2.4 Physical time-frequency resources

The transmitted signal in each slot is described by a resource grid, consisting of subcarriers and OFDM symbols, as illustrated in Fig. 2.5. The smallest physical resource

is called a resource element and is represented by a single subcarrier on a single OFDM symbol. Transmissions are scheduled in groups of 12 consecutive subcarriers, known as Physical Resource Block (PRB). In contrast to LTE, a NR PRB is a one-dimensional measure that spans the frequency domain only, while in LTE PRB consists of 12 subcarriers in the frequency domain and one slot (7 OFDM symbols) in the time domain. Defining resource blocks only in the frequency domain enables a flexible number of OFDM symbols to be allocated for different transmissions, while in LTE transmission it has to occupy a complete slot.

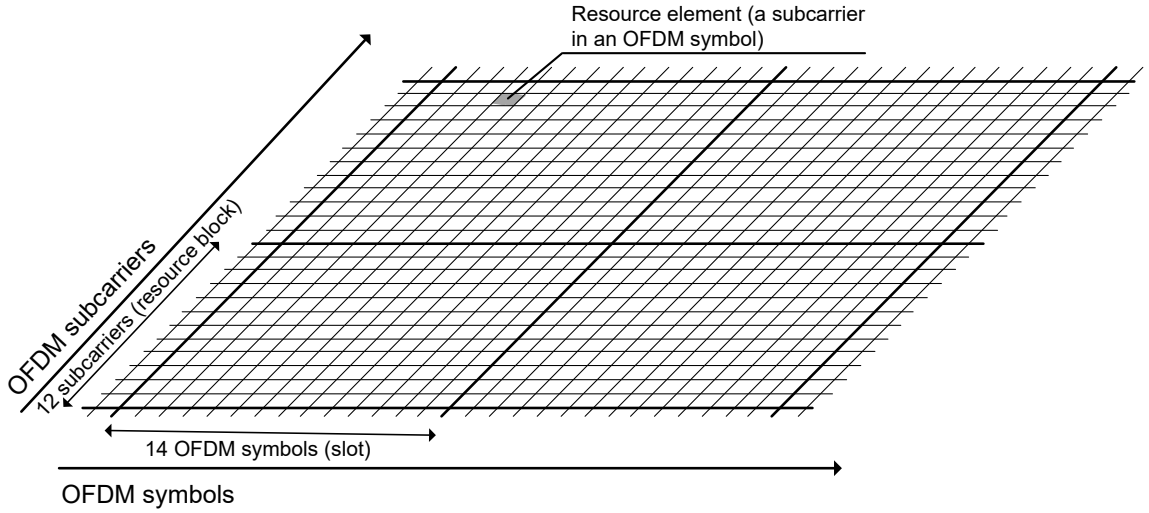

Figure 2.5: NR physical time-frequency structure [9]

In the time domain, radio transmissions are organized into frames of 10 ms length, consisting of 10 subframes of 1 ms length (Fig. 2.6). A subframe comprises one or more adjacent slots, where each slot contains 14 OFDM symbols. To ensure low latency, NR supports occupying only a part of a slot, which is referred to as "mini-slot transmission". A mini-slot structure with lengths between 1 and 13 OFDM symbols is supported. As shown in Fig. 2.6, the duration of a slot in miliseconds depends on numerology and is inversely proportional to its subcarrier spacing. The numbers of slots per frame and slots per subframe for all available OFDM numerology are presented in Table 2.4.

Table 2.4: Frame structure for different OFDM numerology [8]

Subcarrier spacing	15 kHz	30 kHz	60 kHz	120 kHz	240 kHz	480 kHz	960 kHz
Number of slots per subframe	1	2	4	8	16	32	64
Number of slots per frame	10	20	40	80	160	320	640

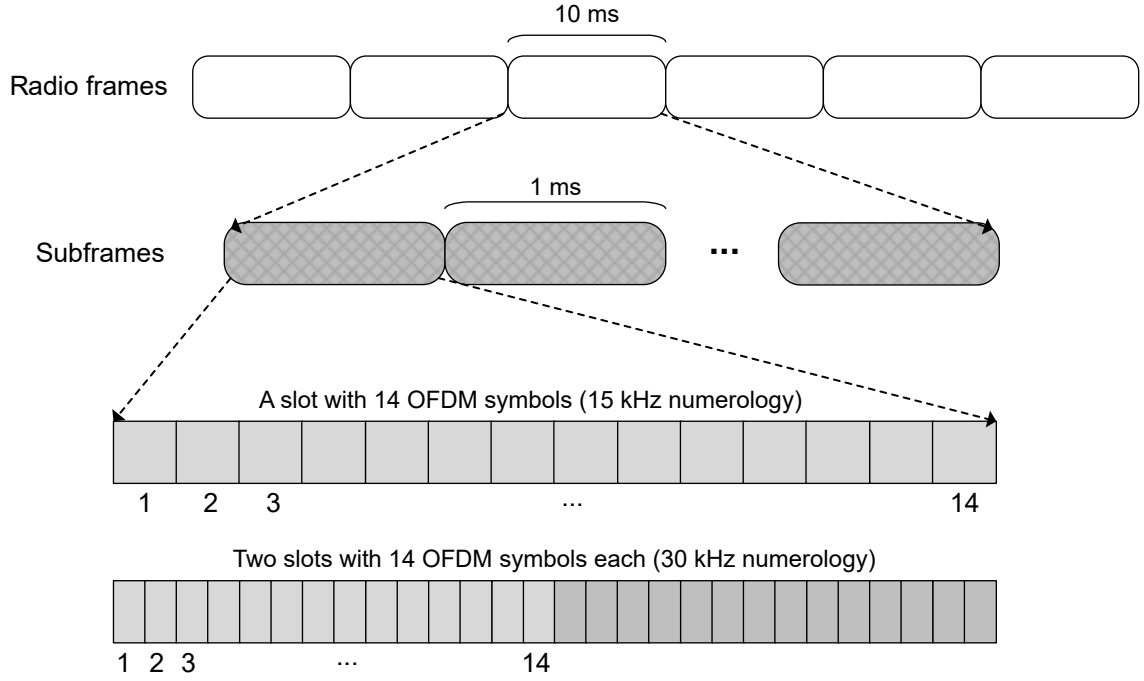

Figure 2.6: NR frame structure [9]

2.3 Transport channel processing

The physical layer transport channels offer information transfer to the MAC layer and higher layers. There are three different downlink transport channels defined for NR: Downlink Shared Channel (DL-SCH), Paging Channel (PCH) and Broadcast Channel (BCH) and one uplink transport channel called Uplink Shared Channel (UL-SCH). DL-SCH and UL-SCH channels are dedicated to data transmission and their overall processing is illustrated in Fig. 2.7. Up to two dynamic-sized transport blocks are delivered to the PHY layer within a single Transmission Time Interval (TTI). The case of two transport blocks is available only in the downlink, for spatial multiplexing with more than four layers, and is dedicated to scenarios with very high Signal-to-Noise-Ratio (SNR).

According to Fig. 2.7, the processing of the transport block starts with the attachment of Cyclic Redundancy Check (CRC), done for error detection purposes, followed by the Low Density Parity Check (LDPC) base graph selection. Then, code block segmentation and another CRC attachment are performed. Next, each block is encoded separately using the LDPC encoder. After that, the rate matching, including the physical layer HARQ changes the number of coded bits to fit the number of available resource elements. Finally, code block concatenation is performed to create up to two codewords for transmission on the physical channel. A physical channel corresponds to a group of time and frequency resources used for the transmission of a particular transport channel. The DL-SCH and UL-SCH transport channels are mapped onto the following physical channels: Physical Downlink Shared Channel (PDSCH) and Phys-

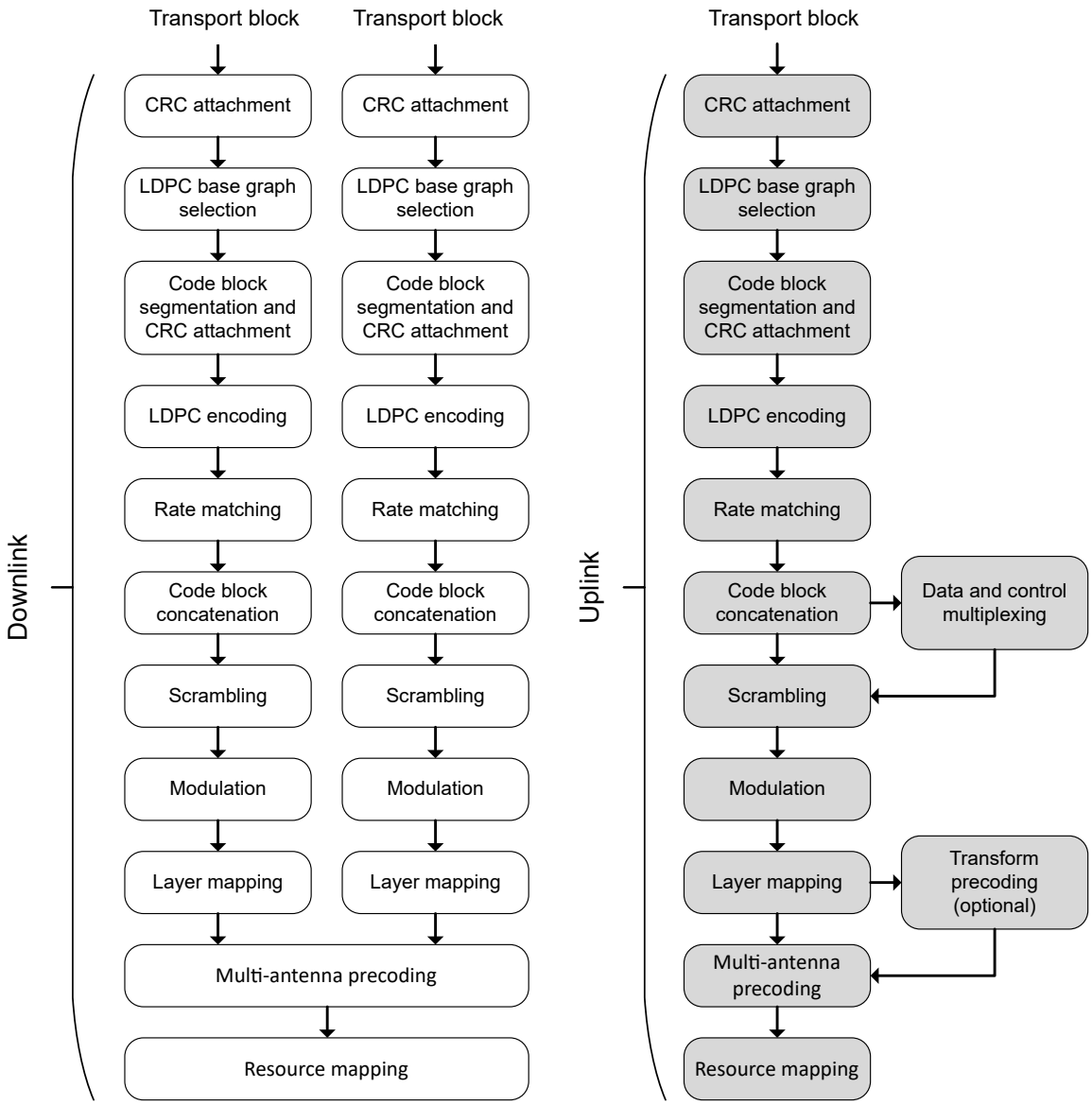

Figure 2.7: Transport channel processing for 5G NR DL-SCH and UL-SCH

ical Uplink Shared Channel (PUSCH), respectively. The content of each codeword is scrambled, then modulated, and finally mapped onto the physical resources, including the spatial domain. In the case of uplink, transform precoding (DFT-spread) is also possible before multiantenna precoding is performed.

In the following subsections, each of the processing steps will be described in more detail.

2.3.1 Transport block CRC attachment

A CRC is an error detection code that allows receiver-side detection of errors in the decoded transport block. Based on the CRC check, the HARQ retransmission may be requested. The length of CRC depends on the size of the transport block. When the

number of input bits is higher than 3824, 24 parity bits will be generated, in other cases there will be 16 parity bits added to a transport block.

2.3.2 LDPC base graph selection

NR supports two LDPC base graphs, one optimized for small transport blocks and the second for larger transport blocks. Each code block of the transport block is encoded with either LDPC base graph 1 or 2 according to the following rule:

- if the transport block size is less than or equal to 292, or if transport block size is less than or equal to 3824 and coding rate $R \leq 0.67$, or if $R \leq 0.25$, LDPC base graph 2 is used,
- otherwise, LDPC base graph 1 is used [11].

2.3.3 Code block segmentation and code block CRC attachment

The maximum code block size accepted by the LDPC encoder in NR is equal to 8448 for base graph 1 and 3840 for base graph 2. If the size of the code block exceeds the maximum length, the transport block including CRC is divided into multiple code blocks of equal size. That division is called code block segmentation. Furthermore, an additional CRC of length 24 is calculated and appended to each new code block.

2.3.4 Channel coding

After code block segmentation, code blocks are delivered to the channel coding block, where each code block is individually encoded. The channel coding in NR is based on LDPC codes. From an error-correcting capability point of view, LDPC codes can achieve similar performance as turbo codes but offer lower complexity, especially at higher code rates. The core of LDPC codes is created by a sparse (low-density) parity check matrix $\boldsymbol{H}$, where for each valid code word $\boldsymbol{c}$ the relation $\boldsymbol{H}\boldsymbol{c}^T = 0$ holds. In the NR standard the parity check matrix is represented by a graph connecting n variable nodes at the top with $(n-k)$ constraint nodes at the bottom of the graph (the so-called base graph). A detailed description of LDPC codes can be found in the literature, for example, in [12]. In NR, quasi-cyclic LDPC codes with a dual-diagonal structure of the kernel part of the parity check matrix are used, which enables simple encoding and gives a linear decoding complexity in the number of coded bits.

2.3.5 Rate matching

Coded bits for each code block are delivered to the rate matching block, where a specified number of coded bits is extracted to match the number of available resources assigned for transmission or to generate different redundancy versions needed for the HARQ protocol. Rate matching is performed separately for each code block, starting with the puncturing of a fixed number of systematic bits. Then, the remaining systematic and parity bits are copied into a circular buffer as shown in Fig. 2.8. The selection of bits to be transmitted depends on the current Redundancy Version (RV) which corresponds to the possible starting position in the circular buffer. It can be seen that during the first transmission attempt (RV0) all systematic bits from the circular buffer are included in the transmission. The rate matching is finished with an interleaver that writes bits from the circular buffer row-by-row and outputs reading them column-by-column. This results in spreading the systematic bits across the modulation symbols and improving transmission reliability.

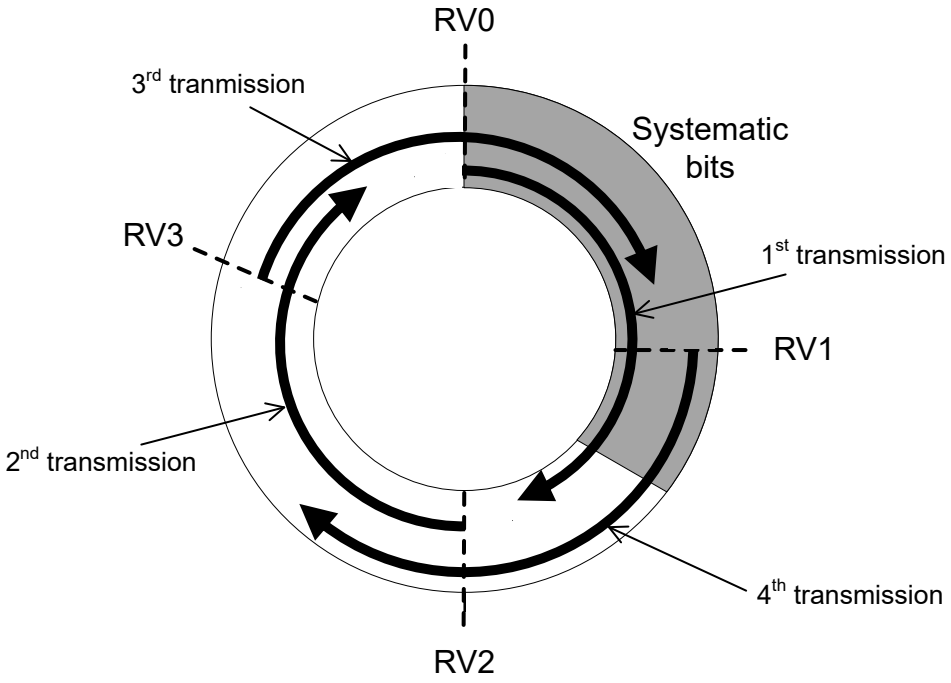

Figure 2.8: Example of circular buffer for incremental redundancy [5]

2.3.6 Scrambling

After rate matching, each codeword is delivered to the scrambler, where the sequence of coded bits is multiplied by a bit-level scramble sequence. The scrambling sequence in all cases uses an order-31 Gold code, which can provide 2^{31} sequences that are not cyclic shifts from each other. The purpose of scrambling is to properly reject interference

from a neighboring cell in the downlink or from other devices in the uplink, by applying different scrambling sequences.

2.3.7 Modulation

The modulation step transforms the block of scrambled bits into a block of complex symbols. Modulation schemes in NR include QPSK, 16QAM, 64QAM, 256QAM in uplink and downlink and 1024 QAM for just downlink. In addition, to reduce a cubic metric and improve power amplifier efficiency, $\pi/2$ -BPSK is supported in uplink in the case where DFT-precoding is used.

2.3.8 Layer mapping

Once codewords have been scrambled and modulated, they are mapped onto transmission layers so that every n-th symbol is mapped to the n-th layer. One codeword can be mapped on up to four layers. To map transmitted data onto five to eight layers, which is supported for both uplink and downlink in the latest Release 18, two codewords are required. Multilayer transmission is possible only with the CP-OFDM waveform. The DFT-spread-OFDM scheme supports only single-layer transmission.

2.3.9 Uplink DFT precoding

As we have mentioned, the DFT-precoding is supported only in uplink in combination with a single layer. The locks of M symbols, where M is the number of subcarriers assigned for transmission, are fed to the DFT of size M, as shown in Fig. 2.9. To decrease the complexity of DFT implementation, but at the same time maintain flexibility in the number of resources scheduled for transmission, the size of DFT in NR is limited to products of integers 2, 3 and 5.

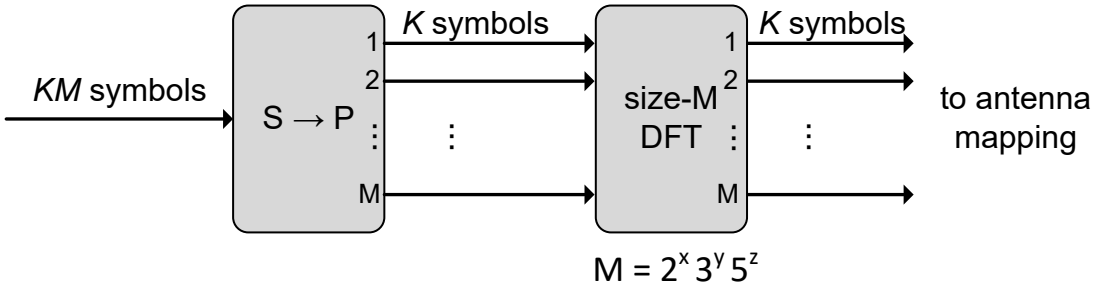

Figure 2.9: DFT precoding [5]

2.3.10 Multi-antenna precoding

The purpose of precoding is to allow a portion of each signal layer to be transmitted through each antenna and, depending on the channel conditions, to provide some flexibility to improve Signal to Interference and Noise Ratio (SINR) at each MIMO receiver. The multi-antenna precoding in NR differs depending on the direction of transmission. The codebook-based precoding, widely used in the LTE system, is supported only in uplink, however, in most cases the precoding is not explicitly visible to the receiver and is seen as a part of a radio channel since the Demodulation Reference Signals (DMRS), used for channel estimation, are subject to the same precoding as the PDSCH and PUSCH. Consequently, there is no need to inform the receiver which precoder was applied. However, the receiver must still know the number of transmission layers.

2.3.10.1 Downlink precoding

The downlink precoder supports transmission on up to eight layers and, using Channel State Information Reference Signals (CSI-RS), can provide the measurements and reporting done by the device to support the network selection of the precoder for downlink PDSCH transmission. The CSI report may include a Rank Indicator (RI), indicating what the device believes would be the most suitable number of transmission layers, a Precoding Matrix Index (PMI) indicating the most suitable (according to the device) precoder chosen from the predefined codebook for a selected rank, and a Channel Quality Indicator (CQI), which provides information about the most suitable channel coding rate and modulation scheme, given the selected precoding matrix. It is worth highlighting that a CSI report does not impose any restrictions on the reporting device on the precoding matrix that is eventually used for downlink transmission and that the chosen precoding matrix does not have to be part of any predefined codebook. In many cases the precoder indicated in the CSI report may be useful and applied by the transmitter, however, in some cases, such as MU-MIMO transmission, the selected precoding matrix should not only focus the energy towards the reporting destination device, but also limit the interference to other devices that were scheduled to use the same time and frequency resources. The NR specification defines two types of CSI: Type I CSI and Type II CSI that differ in size and codebook spatial granularity. Type I CSI was designed to target a high number of layers in the single user scenarios (Single-User Multiple Input Multiple Output (SU-MIMO)), whereas in Type II CSI up to two layers MU-MIMO transmissions can be applied.

2.3.10.2 Uplink precoding

The uplink precoder supports transmission on up to eight layers with CP-OFDM or on one layer with DFT-spread-OFDM. Two different precoding modes can be chosen: codebook-based and non-codebook based, depending on what can be assumed in terms of uplink/downlink channel reciprocity.

In the codebook-based precoding, the device has to follow network recommendations regarding an uplink transmission rank and corresponding precoding matrix. The RI and PMI are sent to the device as part of the uplink scheduling grant and are chosen based on the channel knowledge acquired by the measurements of the Sounding Reference Signal (SRS) transmitted by the device. The precoder suggested by the network is chosen from a predefined codebook with respect to device capabilities in terms of antenna-port coherence. The NR standard supports three different inter-antenna-port coherence capabilities, referred to as full coherence, partial coherence, and no coherence. Full coherence means that the device can fully control the relative phases between its antenna ports, partial coherence that the device can control the relative phase only between a pair of selected ports (out of four) and no coherence means that the relative phase between any two ports cannot be guaranteed. Fig. 2.10 illustrates the available precoder matrices for the single-layer transmission on four antenna ports with respect to the device coherence capabilities. It can be noted that matrices corresponding to no coherence, map the transmitted signal onto one antenna port at a time, which can be treated as simple antenna selection. The extended set of precoding matrices corresponding to partial coherence allows for a linear combination within pairs of antenna ports with selection between the pairs. Full coherence supports a linear combination over all four antenna ports.

In addition to more extensive codebooks, the codebook-based precoding in NR compared to the codebook-based precoding in LTE supports transmission of multiple multi-port SRS that enable the network to choose between several beams that refer to the different antenna panels with different directions, where each panel includes a set of antenna elements, corresponding to antenna ports of each multi-port SRS. The information indicating one of the configured SRSs is provided in the scheduling grant as a one-bit SRS Resource Indicator (SRI). The selected precoder determines how the transmission should be performed within the chosen beam.

The noncodebook-based precoding is illustrated in Fig. 2.11. Similarly to downlink, the transmitting device chooses a precoding matrix based on its measurements and indications sent by the network in the uplink scheduling grant. Device measurements are performed on a configured CSI-RS, assuming that the channel in both directions is reciprocal. Since the precoder chosen by the device may not be the best from a network point of view, the network has a possibility to remove some precoding matrix columns, which can be seen as digital "beams" for the corresponding layers. Information about the selected beams is sent to the device within SRI, included in the

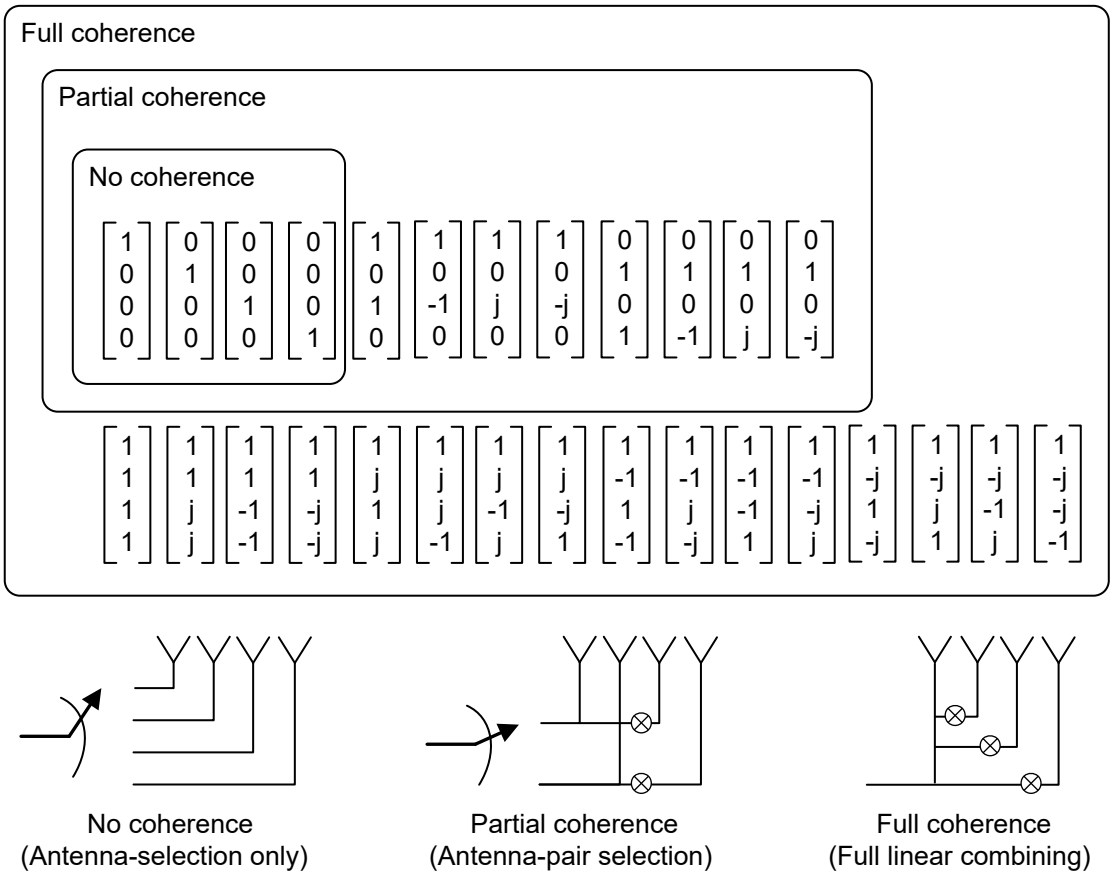

Figure 2.10: Single-layer uplink codebooks for the case of four antenna ports [5]

scheduling grant, based on the measurements of SRS transmitted on each layer. The PUSCH transmission is carried out using a reduced precoder with columns indicated in the SRI feedback.

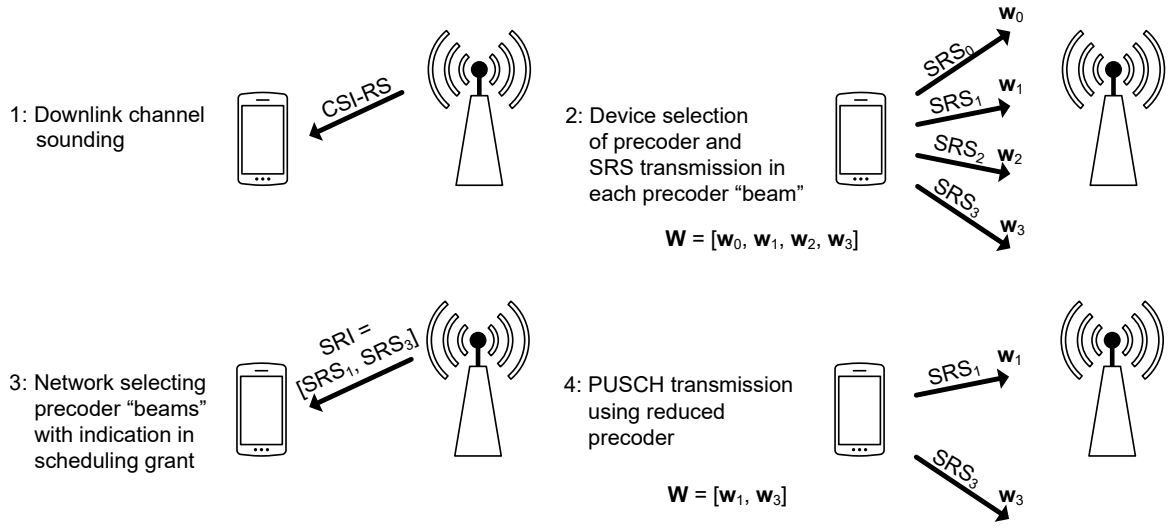

Figure 2.11: Non-codebook based precoding [5]

2.3.11 Resource mapping

After multi-antenna precoding, the complex signals from each antenna port are mapped to the set of available resource elements within scheduled Virtual Resource Blocks (VRBs). The VRBs are defined within a Bandwidth Part (BWP) (a bandwidth being a subset of contiguous Common Resource Blocks (CRBs), over which a device is currently assumed to receive transmissions of a certain numerelogy). The mapping to resource elements, not reserved for other purposes, shall be in increasing order of first the frequency (subcarriers) over the assigned virtual resource blocks and then the time (OFDM symbols). The VRBs are further mapped to Physical Resource Blocks (PRBs) according to indicated mapping scheme: non-interleaved or interleaved (supported only in PDSCH) (Fig. 2.12). If no scheme is indicated, non-interleaved mapping is assumed.

For non-interleaved VRB-to-PRB mapping, virtual resource block n is mapped to physical resource block n^*.

For interleaved VRB-to-PRB mapping, the mapping process uses an interleaver that spans the whole BWP. Pairs/quadruplets of resource blocks are written into a block interleaver with two rows column-by-column and read out row-by-row to achieve frequency diversity.

The PRBs are further mapped to CRBs which corresponds to the concrete RF carriers and are spanned over the whole bandwidth of the system.

2.4 Relay Technology for 5G Networks

The concept of RNs originated as an information theoretical scenario in [13], where an upper bound on the relay channel capacity was found. RNs have been standardized by 3GPP LTE-A for efficient heterogeneous network planning. The Relay Node (RN) was defined as a low power eNB that can be deployed underneath macro Base Station (BS) (Donor eNB (DeNB)), forming small cell and providing coverage and capacity at cell edge. The RN is connected to DeNB by a wireless backhaul link and to Mobile Station (MS) by an access link (Fig. 2.13).

2.4.1 Relay Classification

Relays can be categorized according to several criteria. Since RNs may perform their operations in different protocol stack layers, we can distinguish [14]:

*Except for PDSCH transmission with Downlink Control Information (DCI) format 1_0 in a common search space, where virtual resource block n is mapped to physical resource block $n + N_{start}^{CORESET}$, where $N_{start}^{CORESET}$ is the lowest-numbered physical resource block in the control resource set, where the corresponding DCI was received.

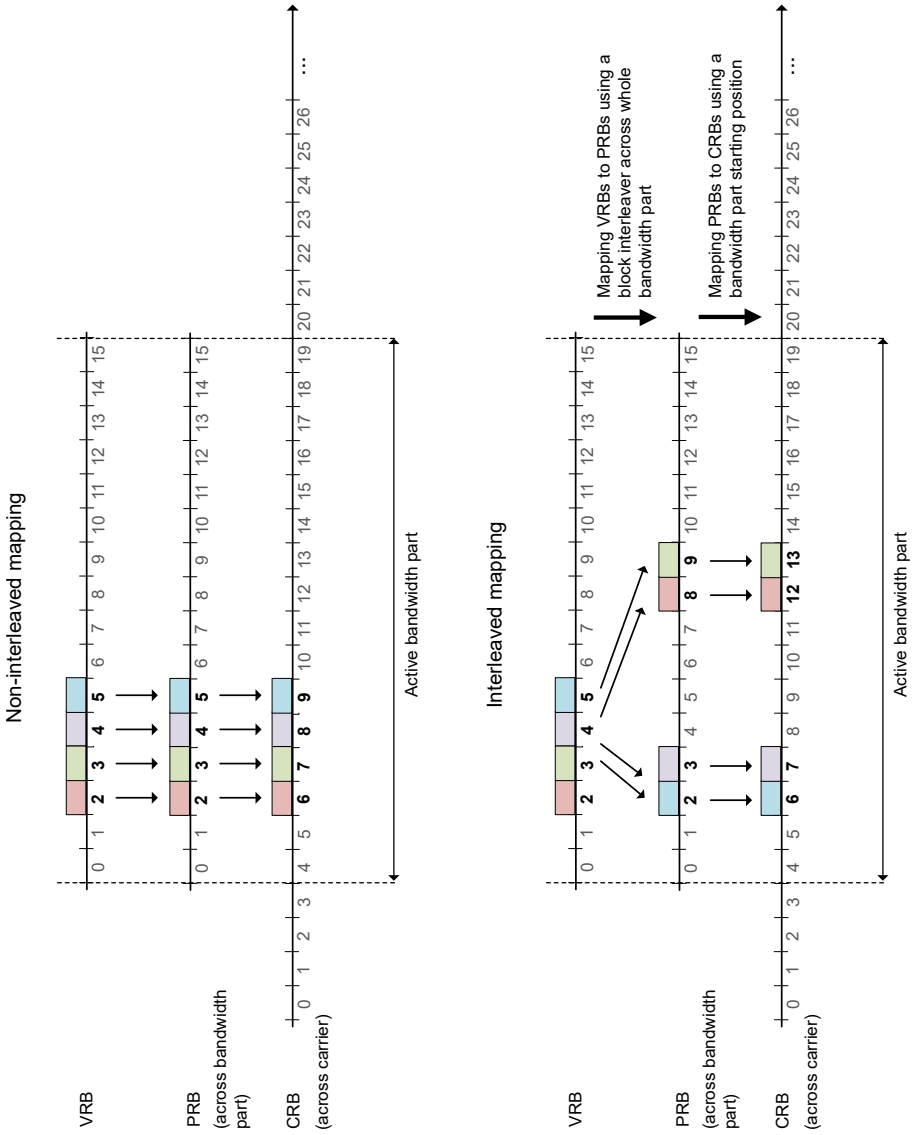

Figure 2.12: Resource mapping in NR [5]

- Layer 1 relays that operate in physical layer and utilize an Amplify and Forward (AF) strategy in which the received signal is simply amplified and retransmitted without decoding.
- Layer 2 relays called Decode and Forward (DF) relays, decode, re-modulate and retransmit the received signal. Compared to the AF strategy, the DF protocol can eliminate the noise signal; however, the complexity of the DF strategy and the delay introduced by it are significantly higher.
- Layer 3 relays also called DF relay, can be seen as regular BS with wireless backhaul link instead of wired. In addition to layer 2 relays, relays operating in layer 3 eliminate intercell interference and noise, and thus improve throughput.

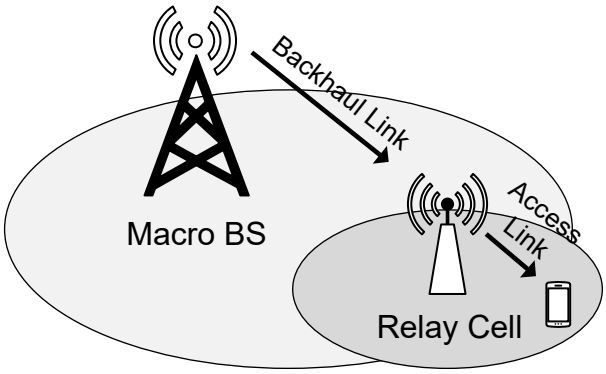

Figure 2.13: Relay cell [14]

Moreover, depending on the resource assignment scheme for backhaul link we can distinguish:

- Inband relays, where the backhaul link between BS and RN uses the same frequency as the access link between RN and MS.
- Outband relays, where separate frequencies are utilized for backhaul and access link.

The RNs can be also divided with respect to their transceivers' capabilities into following categories:

- Half Duplex (HD) relays, where two orthogonal time/frequency channels are allocated for the reception and transmission at a relay.
- Full Duplex (FD) relays, where transmission and reception are performed simultaneously on the same time/frequency resources.

Regardless of aforementioned classifications, the 3GPP consortium defined their own two types of relays that combine different characteristics at once:

- Type-1 relays are non-transparent to the system and assist in the communication between BS and UEs when UE is located at the cell edge. Type-1 relays transmit their own control messages, forming a relay cell that extends DeNB coverage. Type-1 relays can be further specialized into:
  - Type-1a - outband relays with FD scheme.
  - Type-1b - inband relays with HD scheme.
- Type-2 relays are transparent to the system and their main goal is to improve the link capacity and transmission quality between BS and UEs that are located within BS coverage area. Since type-2 relays are part of DeNB cell, the cell control message is not transmitted by the relay.

2.4.2 Potential Benefits of Relays

The performance of the cellular communication system is affected by fading, path loss, and shadowing factors. The deployment of low power RNs has attracted considerable attention due to its ability to increase the reliability and capacity of the system, while at the same time reducing operational costs.

The reliability of the link between BS and UE can be improved by exploiting the additional spatial diversity introduced by relay that forwards data from BS towards UE. As illustrated in Fig. 2.14, UE receives additional copies of the transmitted signal from RNs, which combined properly at the receiver, increases transmission reliability.

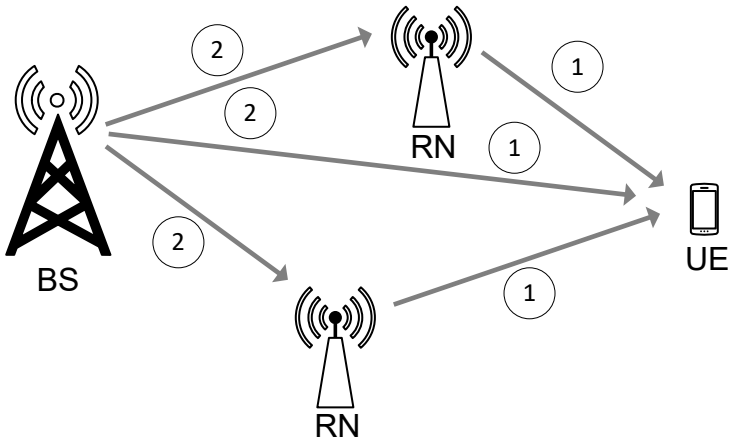

Figure 2.14: Spatial diversity for reliability improvement [14]

Relays placed at the border of a cell served by the base station can efficiently fill coverage holes and extend donor cell coverage. In Fig. 2.15 when the signal from BS is too weak, the transmission can still be maintained using a relay path as a substitute for the path between BS and UE. On the other hand, relays located within the BS cell can increase its capacity.

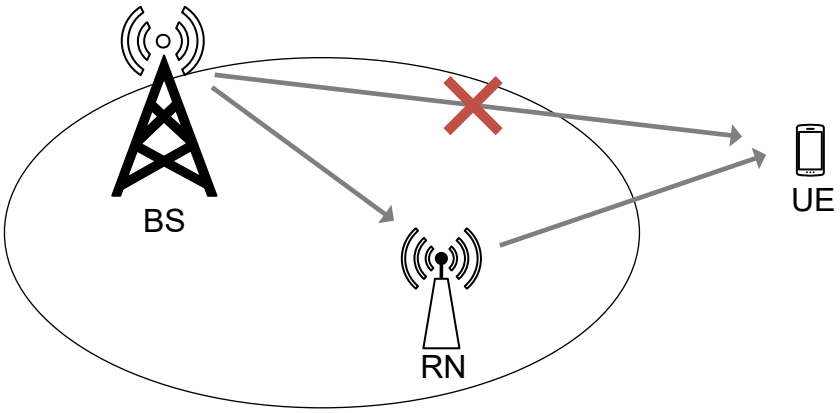

Figure 2.15: Relay for coverage extension [14]

Considering the utilization of radio resources, RNs add a traffic offloading functionality by balancing a traffic load among highly and lightly loaded cells. As shown

in Fig. 2.16, the relay station located at the cell edge of its DeNB may accept a set of UEs within its coverage from adjacent more congested cell and shift them to be served by its DeNB.

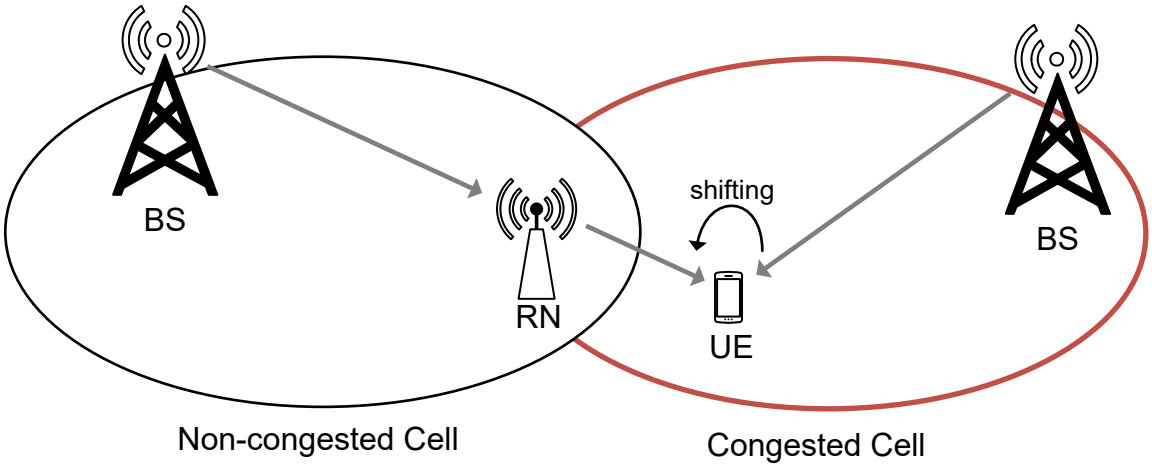

Figure 2.16: Relay for traffic load balance [14]

Finally, the deployment of low power RNs can reduce operational costs for service providers. Due to the lower distances between UE and RNs compared to BS (which results in a lower path loss), transmitted power can be significantly reduced. Relay deployment is also an easier, faster, and cheaper way to extend coverage since, unlike regular base stations, there is no need to install a backhaul link.

2.4.3 Key Applications in 5G

Standardization activities are continuously performed at 3GPP on NR with the aim of achieving high-speed, high-capacity communications beyond LTE-A. 3GPP proposed various scenarios in which the role of relaying can be foreseen and potentially useful, such as [15]):

- **Small Cells with wireless backhaul**, where relays can play a significant role in network densification. Using RN, the small cell BS can be connected to the infrastructure by wireless backhaul, instead of wired. Wireless backhaul is a preferred solution when it comes to flexible and rapid deployment, cost efficiency, and increased connectivity. In fact, using an in-band relay that acts as a small cell BS transforms this small cell into a relay cell without the need for an additional spectrum (as would take place in the case of out-of-band relay). Moreover, application of techniques such as wireless network coding recovers spectral efficiency, that is decreased by wireless backhaul, and brings forward in-band RNs as a feasible solution for wireless backhaul.

- **Wireless backhauling for nomadic nodes**, where the nomadic node is a low-power access node that has a flexible backhaul, is movable and can be temporarily

activated to provide additional system capacity and coverage on demand. Nomadic nodes and dynamic network topology are important parts of the concept of the 5G system and can be enabled by RNs. A typical example of a nomadic node is a parked vehicle that creates a cell for all UEs nearby. In that case, the relay acts as a BS for connected UEs and as a UE for the fixed infrastructure. Nomadic relays can be especially promising in urban areas, integrated into vehicles such as city buses, car sharing fleets, or taxi services.

- **Device-to-Device communication** which is a vital part of 5G as it exploits the proximity of the user to offload the traffic from the core network, offers spectral efficiency, energy efficiency, increased throughput, and reduced latency for the end nodes. Communication between two devices can be performed directly or through the relay, depending on the channel conditions between the D2D devices. Relay thus can efficiently enhance the performance of D2D communication, ranging from the support of multiple simultaneous D2D links by a single relay to the cooperation of multiple relays.

- **Millimeter wave communications** which due to substantial transmission losses, suffer from a significantly reduced coverage, especially in indoor scenarios. Therefore, RNs are one of the emerging components to enable mm-wave communication by providing sufficient coverage.

- **Machine-Type Communications** which seeks spectrally and energy efficient ways to provide ubiquitous connectivity among massive number of low-cost devices. A large number of autonomous devices create problems for the access protocol. A feasible solution to mitigate Radio Access Network (RAN) congestion is the usage of relay nodes, that can deal with an access problem of MTC devices in their proximity and thus lessen the access burden put on BS. Furthermore, since relays bring the infrastructure closer to MTC, the transmitted power may be decreased, which meets the energy efficiency requirements of MTC.

Fig. 2.17 presents the aforementioned key 5G applications.

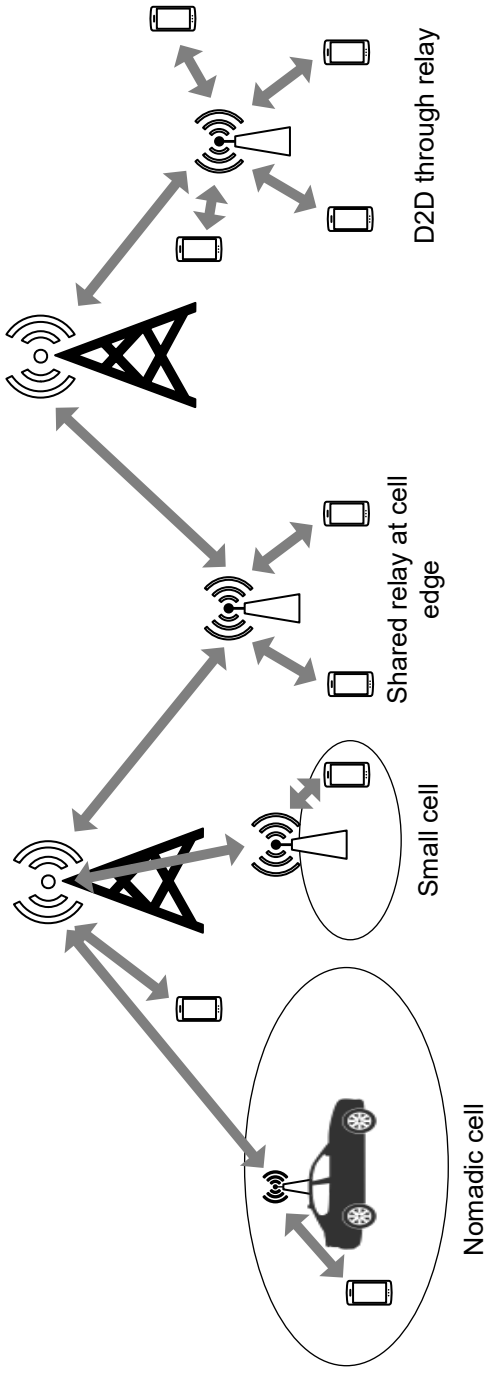

Figure 2.17: Use of relays in 5G landscapes [15]

Chapter 3

Two-way relaying transmission schemes

3.1 Introduction

The 5G system need to handle the demanding requirements of the end user in data rate and error performance. Numerous potential technologies have been proposed and investigated to satisfy these requirements. One particularly promising example is TWR, which can theoretically introduce a data rate 100% higher than that of current systems with orthogonal access. The example of a two-way relay channel is illustrated in Fig. 3.1. The basic idea is that two source nodes (A and B) have data to exchange with each other, but for some reason (e.g. the distance between nodes is too high) they wish to use an intermediate relay node for that purpose.

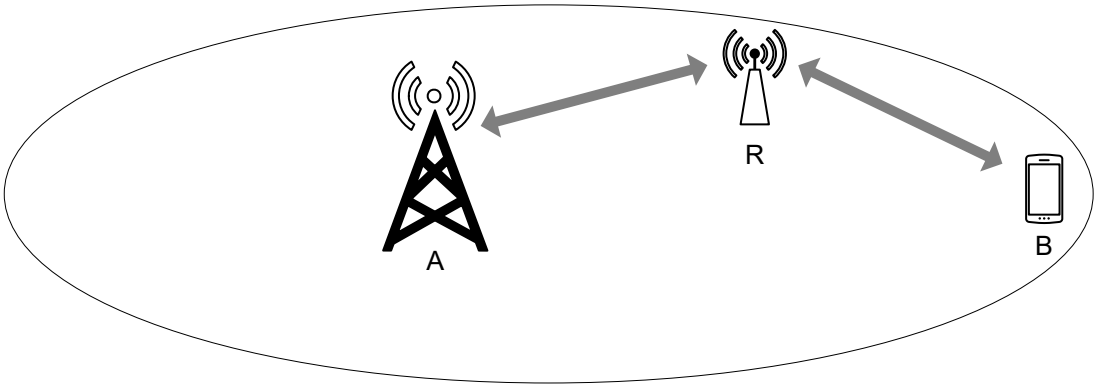

Figure 3.1: Two-way relay channel

The TWR channel was first studied by Shannon in [16] and its capacity was theoretically analyzed in [13]. The TWR channel can operate in a variety of modes, involving different schedules for activation of the nodes that are part of it. Fig. 3.2 presents possible activation schedules for the TWR channel. In the conventional approach (Fig.

3.2a), four phases (time slots) are needed to exchange data blocks between two stations. First, node A transmits its bit packet (X_A) to relay node R, then R retransmits the message from A to node B (X_A). After that, node B transmits its data block (X_B) to R, and finally R retransmits B's data to terminal A (X_B). In conventional four-phase relaying, it is assumed that none of these phases can take place concurrently, either because of the half-duplex constraint on the relay or the interference between different links.

3.2 Network Coding

The concept of network coding was originally introduced by Ahlswede in [17] to enhance the throughput of multi-hop wired networks. In wireless networks, NC is considered an effective approach to controlling the interference problem in the two-way relay channel. In the network layer NC presented in Fig. 3.2b, instead of simply forwarding the received data, the relay calculates a function of both bit packets X_A and X_B and then retransmits the result. The function is referred to as the network code function or mapping, and in the presented example, where the data are binary, it is represented by an exclusive OR (XOR) operation. As seen in Fig. 3.2b with the network coding scheme, transmission may be reduced to three phases: node A transmits its data to the relay in the first phase, then in the second phase node B transmits its data to the relay and in the third phase the relay forms the function $X_R = X_A \oplus X_B$ and transmits the result simultaneously to source nodes A and B. After receiving the joint message $X_R = X_A \oplus X_B$, terminal A performs an XOR operation with its message X_A to decode the message X_B (equation (3.1)), while terminal B calculates the XOR of the received message $X_R = X_A \oplus X_B$ with the message X_B and as a result, obtains message X_A (equation (3.2)). The aforementioned scheme operates under the assumption that both end nodes possess side information, including the data packets they have sent during the multiple-access phase.

$$X_A \oplus X_R = X_A \oplus X_A \oplus X_B = X_B \tag{3.1}$$

$$X_B \oplus X_R = X_B \oplus X_A \oplus X_B = X_A \tag{3.2}$$

To compare the classical TWR and TWR-NC, the spectral and energy efficiency of these two schemes will be derived. Defining the spectral efficiency as the number of bits transmitted from both source nodes over the required time slots, the spectral efficiency of these two schemes can be expressed as follows [18]:

$$\zeta_{TWR} = \frac{2\log_2 M}{4} = \frac{1}{2}\log_2 M \quad \text{[bps/Hz]} \tag{3.3}$$

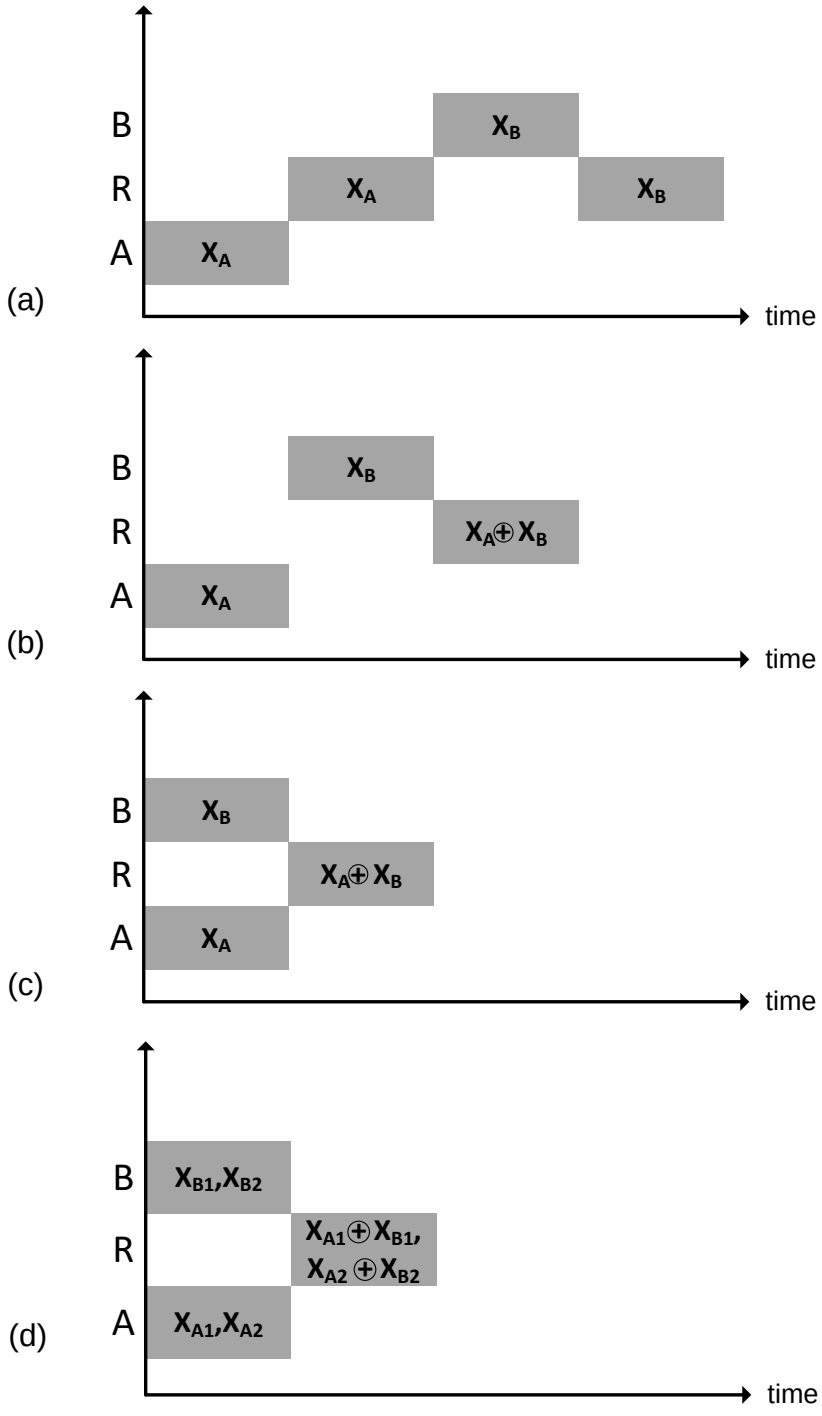

Figure 3.2: Activation schedules for the TWR channel: (a) conventional, four phase; (b) network layer NC, three-phases; (c) PNC, two-phases; (d) PNC-SSA and NC, two-phases

$$\zeta_{TWR-NC} = \frac{2\log_2 M}{3} = \frac{2}{3}\log_2 M \quad [\text{bps/Hz}] \tag{3.4}$$

where M is a modulation order. It is evident that the NC scheme can achieve higher spectral efficiency than the conventional TWR scheme.

Energy efficiency can be defined as the ratio of the total transmitted data in both directions to the total transmit power required by all nodes, including both sources and the relay. Assuming that each transmitter uses a total transmit power denoted by P, the TWR and TWR-NC schemes achieve the following energy efficiencies [18]:

$$\epsilon_{TWR} = \frac{\frac{1}{2}\log_2 M}{4P} = \frac{\log_2 M}{8P} \quad [\text{bps/Hz/W}] \tag{3.5}$$

$$\epsilon_{TWR-NC} = \frac{\frac{2}{3}\log_2 M}{3P} = \frac{2\log_2 M}{9P} \quad [\text{bps/Hz/W}] \tag{3.6}$$

It can be easily concluded that, with a fixed modulation order and transmit power, the TWR-NC scheme achieves approximately 1.78 times the efficiency of the conventional four-slot TWR scheme.

3.3 Physical-Layer network coding

The concept of Physical-Layer Network Coding (PNC) was introduced in 2006 in [19] for use in wireless networks. Since its inception, it has evolved into a significant subfield of network coding. The core idea of PNC is to utilize the natural signal mixing that occurs when electromagnetic waves overlap. Specifically, when multiple transmitters send signals simultaneously, a receiver captures a weighted sum of these signals, effectively performing a network coding operation through natural means. In addition, the received signal can be converted and mapped onto different forms of network coding. Exploiting these phenomena has profound and far-reaching implications. Typically, in wireless networks, interference is treated as a destructive phenomenon. PNC was an attempt to exploit the interference to increase the system performance [20].

Compared to the NC scheme, the PNC approach further reduces the number of required time slots to two. The idea of the PNC scheme is illustrated in Fig. 3.2c. In that case, terminals A and B transmit their messages simultaneously to the relay node (at the same time and frequency resources). The relay receives a superposition of the electromagnetic waves of the two wireless signals, but these signals are no longer separable. Since the relay cannot decode the data of terminals A and B separately, only the network code function $X_A + X_B$ is extracted from the superposed received signal $S_A + S_B$, where S_A and S_B are modulated symbols of data packets X_A and X_B, respectively. The second phase is carried out similarly to the network coding scheme in Fig. 3.2b. The relay broadcasts network coded message $X_R = X_A \oplus X_B$ to

terminals A and B, where the data packets X_A and X_B are decoded according to the side information X_A and X_B respectively (equations (3.1) and (3.2)).

In PNC, a key issue is how the relay extracts $X_A \oplus X_B$ from the overlapping electromagnetic waves. This process is commonly termed "PNC mapping" in the literature. Assuming the idealized case of QPSK modulation, symbol and carrier-phase synchronization, and power control, ensure that packets from sources A and B reach the relay with identical phase and amplitude. Neglecting noise, the bandpass signal received by the relay during one symbol period can be expressed as:

$$\begin{aligned} y_R(t) &= s_A(t) + s_B(t) \\ &= [s_A^{(I)} cos(\omega t) - s_A^{(Q)} sin(\omega t)] + [s_B^{(I)} cos(\omega t) - s_B^{(Q)} sin(\omega t)] \\ &= (s_A^{(I)} + s_B^{(I)}) cos(\omega t) - (s_A^{(Q)} + s_B^{(Q)}) sin(\omega t) \end{aligned} \tag{3.7}$$

where $s_A(t)$ and $s_B(t)$ are the QPSK symbols sent by node A and node B, respectively, $s_A^{(I)}$ and $s_B^{(I)}$ are the in-phase components and $s_A^{(Q)}$ and $s_B^{(Q)}$ are quadrature components of the respective QPSK symbol. The baseband in-phase (I) and quadrature (Q) components corresponding to equation (3.7) are

$$\begin{aligned} y_R^{(I)} &= s_A^{(I)} + s_B^{(I)} \\ y_R^{(Q)} &= s_A^{(Q)} + s_B^{(Q)} \end{aligned} \tag{3.8}$$

Equations (3.8) confirm that the relay is not able to extract individual symbols transmitted by node A and B, since in the given two equations there are four unknowns, namely $s_A^{(I)}, s_A^{(Q)}, s_B^{(I)}$ and $s_B^{(Q)}$. In PNC, however, the relay does not need the individual values of all unknown components. It only needs to derive two values $s_R^{(I)} = s_A^{(I)} + s_B^{(I)}$ and $s_R^{(Q)} = s_A^{(Q)} + s_B^{(Q)}$ to form a QPSK symbol s_R with binary representation x_R equal $x_R = x_A \oplus x_B$. The PNC mapping from $y_R^{(I)}$ to $s_R^{(I)}$ for in-phase components is presented in Table 3.1. The mapping for the quadrature components is analogous.

Table 3.1: PNC mapping of in-phase signal components

Symbol from node A: $s_A^{(I)}$	**Bit from node A:** $x_A^{(I)}$	**Symbol from node B:** $s_B^{(I)}$	**Bit from node B:** $x_B^{(I)}$	**Signal received at relay:** $y_R^{(I)}$	**XOR:** $x_R^{(I)} = x_A^{(I)} \oplus x_B^{(I)}$	**Symbol transm. by relay:** $s_R^{(I)}$
1	0	1	0	2	0	1
1	0	-1	1	0	1	-1
-1	1	1	0	0	1	-1
-1	1	-1	1	-2	0	1

After PNC mapping, relay R transmits the following signal to nodes A and B:

$$s_R(t) = s_R^{(I)} cos(\omega t) - s_R^{(Q)} sin(\omega t) \tag{3.9}$$

In PNC, the RF signal transmitted during the second time slot corresponds to the RF signal transmitted during the third time slot in the NC scheme. The key difference between these two schemes lies in their methods of obtaining the symbol packet S_R. In NC, nodes A and B transmit S_A and S_B separately, and relay R decodes the messages of these symbols explicitly to construct S_R. The relay demodulates and decodes the signals S_A and S_B into the binary representation X_A and X_B, computes $X_R = X_A \oplus X_B$, encodes it, and then modulates to obtain S_R. In contrast, PNC derives S_R from the superimposed signal $S_A + S_B$ transmitted during the first time slot. The relay demodulates and decodes $S_A + S_B$ with the channel decoder into their binary representation $X_A \oplus X_B$, subsequently encoding and modulating it again to derive the S_R symbol packet. This approach requires the deployment of a linear channel coding in the transport layer such as turbo code or LDPC codes.

It should be noted that the arithmetic sum $S_A + S_B$ also constitutes a form of network coding operation termed in the literature as Analog Network Coding (ANC), where the relay performs a linear combination of the received superimposed signals and forwards the result to the destination nodes. However, in the presence of channel fading and noise, a better error performance is achieved when the PNC scheme is used.

In order to compare the TWR-PNC scheme with the classic TWR and TWR-NC, the spectral and energy efficiency is calculated and presented below:

$$\zeta_{TWR-PNC} = \frac{2\log_2 M}{2} = \log_2 M \quad [\text{bps/Hz}] \tag{3.10}$$

$$\epsilon_{TWR-PNC} = \frac{\log_2 M}{3P} \quad [\text{bps/Hz/W}] \tag{3.11}$$

It may be seen that TWR-PNC features the highest spectral and energy efficiency compared to the TWR and TWR-NC schemes.

3.4 Signal Space Alignment

SSA is a wireless communication technique that enables PNC in MIMO wireless networks. It was introduced in [21] as a way to enhance network capacity by allowing multiple MIMO transmitters to send data simultaneously. By using calculated precoding, SSA reduces the perceived signal space at a node to match its receiving capability, enabling the demodulation of linearly combined data packets. PNC combined with SSA (PNC-SSA) can fully exploit the precoding space at the transmitters and better utilize the spatial diversity of a MIMO network, resulting in higher system Degrees Of Freedom (DOF). SSA is similar to Interference Alignment (IA) scheme since both techniques make efficient use of the dimension of the signal space. However, while IA focuses on overlapping the interference to minimize the dimension of the signal space

occupied by harmful signals, the key idea of SSA is to align the desired signals received from different users to jointly perform detection and decoding.

The idea of PNC-SSA is illustrated in Fig. 3.2d. Like in the traditional PNC, data exchange is completed in just two time slots, but a greater number of data packets can be transmitted within this period. In the provided example, four messages are exchanged, which requires the presence of at least two antennas at node A, B and relay. Increasing the number of antennas at each node increases the multiplexing gain of the two-way relay channel, allowing more message transmissions. However, for simplicity, the scenario with two antennas and four messages will be examined.

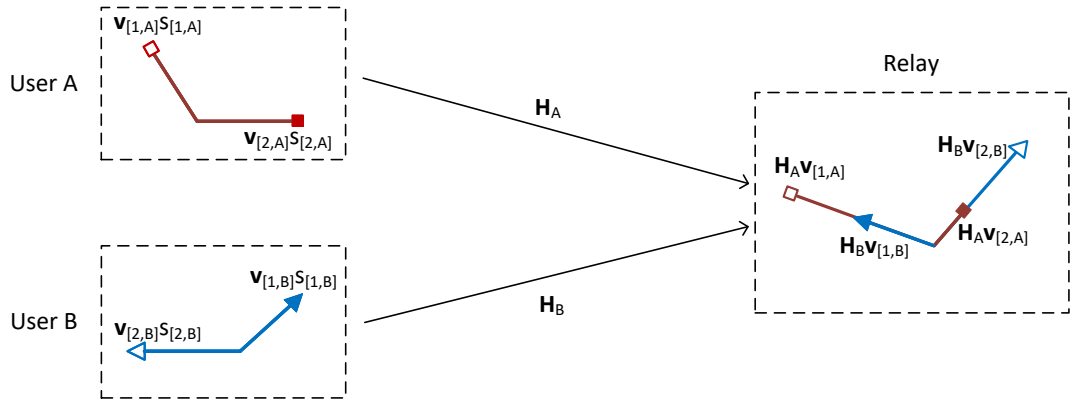

Figure 3.3: Concept of signal space alignment in MA phase

Fig. 3.3 illustrates a detailed PNC-SSA solution for a two-way relay scheme that uses two antennas at each node. During a single symbol period, user A transmits two symbols (s_{1A}, s_{2A}) to the relay (intended for user B), while simultaneously user B sends two symbols (s_{1B}, s_{2B}) to the same relay (intended for user A). In SSA, each user performs precoding, so that the signals arriving at the relay span a number of dimensions that match the relay's receive diversity. As a consequence, the relay is able to decode a linear combination of the transmitted data. Let $\boldsymbol{u}_1$ and $\boldsymbol{u}_2$ be two 2×1 vectors that denote the target directions on the relay for signal alignment and $\boldsymbol{u}_1 \neq \boldsymbol{u}_2$. The signal alignment constraint takes the following form:

$$\begin{aligned} \boldsymbol{H}_A\boldsymbol{v}_{[1A]} &= \boldsymbol{H}_B\boldsymbol{v}_{[1B]} = \boldsymbol{u}_1 \\ \boldsymbol{H}_A\boldsymbol{v}_{[2A]} &= \boldsymbol{H}_B\boldsymbol{v}_{[2B]} = \boldsymbol{u}_2 \end{aligned} \tag{3.12}$$

under the assumption that

$$\begin{aligned} ||\boldsymbol{V}_A||_F^2 &\leq P_A \\ ||\boldsymbol{V}_B||_F^2 &\leq P_B \end{aligned} \tag{3.13}$$

where $\boldsymbol{V}_A = [\boldsymbol{v}_{[1A]}\ \boldsymbol{v}_{[2A]}]$ and $\boldsymbol{V}_B = [\boldsymbol{v}_{[1B]}\ \boldsymbol{v}_{[2B]}]$ are 2×2 precoding matrices, $\boldsymbol{H}_A$, $\boldsymbol{H}_B$ channel matrices and P_A, P_B are transmitted power constraints of user A and B, respectively. Disregarding noise, the signal received by the relay takes form

$$\begin{aligned} \boldsymbol{y}_R &= \boldsymbol{H}_A \boldsymbol{v}_{[1A]} s_{[1A]} + \boldsymbol{H}_A \boldsymbol{v}_{[2A]} s_{[2A]} + \boldsymbol{H}_B \boldsymbol{v}_{[1B]} s_{[1B]} + \boldsymbol{H}_B \boldsymbol{v}_{[2B]} s_{[2B]} \\ &= \boldsymbol{u}_1 (s_{[1A]} + s_{[1B]}) + \boldsymbol{u}_2 (s_{[2A]} + s_{[2B]}) \end{aligned} \tag{3.14}$$

In the analyzed example, the relay receives two overlapped signals $s_{[1A]} + s_{[1B]}$ and $s_{[2A]} + s_{[2B]}$ that, in the next step, are decoded to binary representation of $x_{[1A]} \oplus x_{[1B]}$ and $x_{[2A]} \oplus x_{2B}$, encoded again and retransmitted in the broadcast phase.

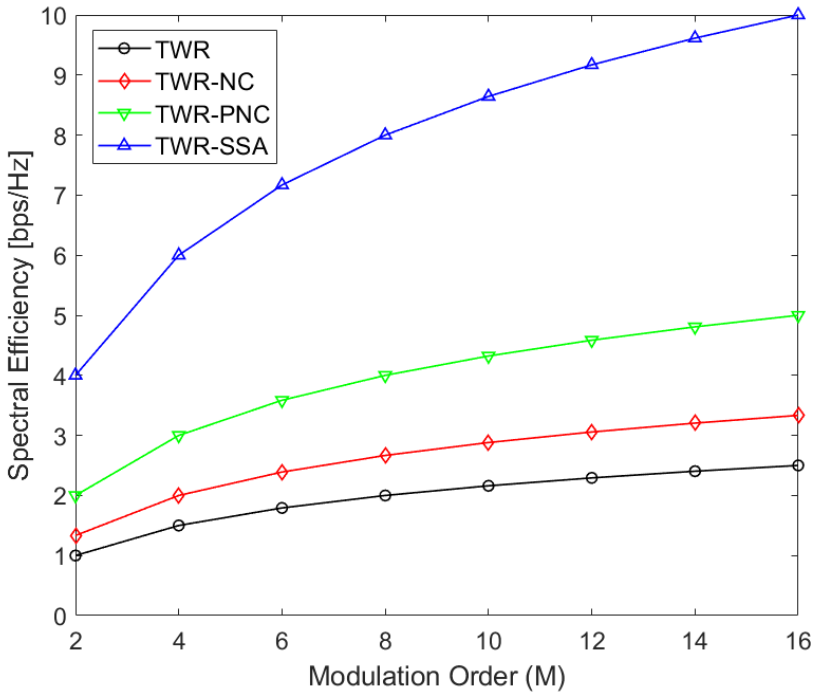

Figure 3.4: Spectral efficiency of the four considered two-way relaying schemes versus the modulation order M

For comparison with TWR-PNC, TWR-NC and classic TWR, the spectral and energy efficiency have been calculated and are presented below:

$$\zeta_{TWR-SSA} = \frac{4 \log_2 M}{2} = 2 \log_2 M \quad \text{[bps/Hz]} \tag{3.15}$$

$$\epsilon_{TWR-SSA} = \frac{2 \log_2 M}{3P} \quad \text{[bps/Hz/W]} \tag{3.16}$$

It may be seen that TWR-SSA outperforms other schemes in case of spectral and energy efficiency.

In Fig. 3.4, the achievable spectral efficiency of the four schemes: TWR, TWR-NC, TWR-PNC, and TWR-SSA is plotted based on equations (3.3), (3.4), (3.10) and (3.15) as a function of modulation order M. It is evident that for any modulation order, TWR-SSA scheme achieves the highest spectral efficiency. For example, at $M = 4$, the TWR scheme achieves 1.5 bps/Hz, the TWR-NC 2 bps/Hz, TWR-PNC 3 bps/Hz, while the TWR-SSA achieves 6 bps/Hz.

The energy efficiency versus the modulation order M for the four schemes: TWR, TWR-NC, TWR-PNC, and TWR-SSA is depicted in Fig. 3.5 based on equations (3.5), (3.6), (3.11) and (3.16). The transmit power is set to $1W$ for all schemes. Throughout the entire range of modulation orders, the TWR-SSA scheme exhibits superior energy efficiency compared to TWR, TWR-NC, and TWR-PNC. For example, at $M = 4$, the energy efficiency of TWR, TWR-NC, TWR-PNC, and TWR-SSA is 0.38, 0.67, 1 and 2 bps/Hz/W, respectively.

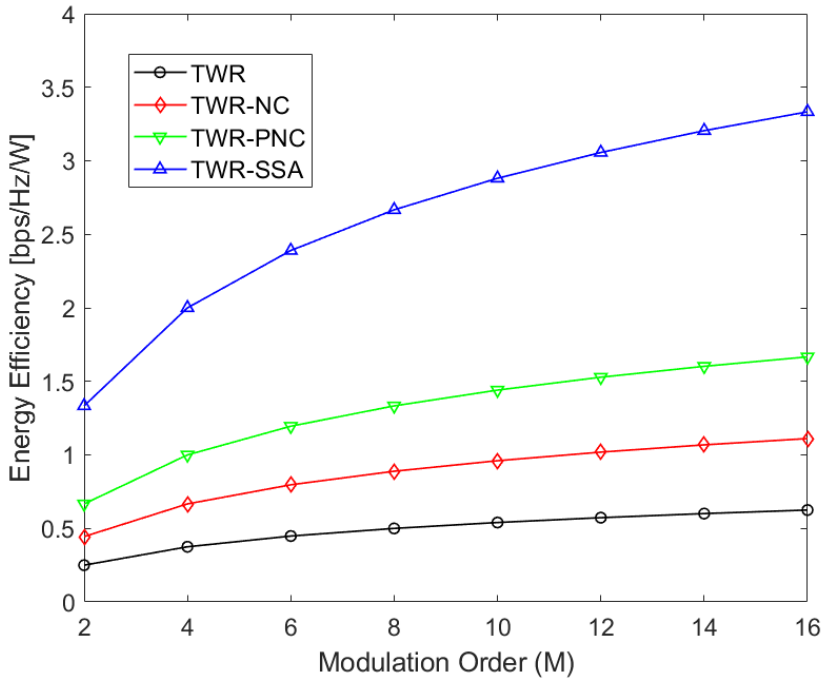

Figure 3.5: Achievable energy efficiency of the four considered two-way relaying schemes versus the modulation order M (P=1W)

3.5 Conclusions

This chapter provided a basic overview of two-way relay communication, focusing on the schemes such as network coding (NC), physical layer network coding (PNC), and signal space alignment (SSA). These techniques were detailed and evaluated with the focus on their spectral and energy efficiency. In the next two chapters, novel schemes aimed at improving two-way relaying performance will be introduced in specific scenarios. The proposed solutions will be evaluated using the 5G system simulator developed by the author. These upcoming chapters will form the primary contributions of this thesis.

Chapter 4

MRT precoding for two-way relaying

4.1 Introduction and related works

The two-way communication channel, where two nodes simultaneously transmit signal to each other, was first studied by Shannon in [16]. The two-way relay channel that incorporates network coding was introduced in the seminar paper by Alswede [17] and has emerged as a promising transmission technology. The key idea of NC is to ask the intermediate node to mix the messages it received and forward the mixture to several destinations simultaneously. The combination of network coding with the MIMO technique was considered in [22], [23], [24], [25] and [26]. Assuming a binary symmetric relay channel, it was shown that bidirectional relaying with MIMO-NC performs equivalently to 2x2 V-BLAST MIMO and a 2x1 Alamouti MISO in multiple access phase and broadcasting phase, respectively [26]. In [24] and [25] the optimal precoding design for AF network coding (AF-NC) is presented. In [23], a DF network coding scheme (DF-NC) is proposed for MIMO multiple access relaying channels. In [22], an DF-NC scheme with the virtual MIMO technique is considered in the multiple access phase and network coding in the broadcast phase. In this investigation, the scheme of [22] was extended in the case when multiple antennas are available at each station during the broadcast phase. With that assumption, simple single-antenna network coding evolved to MISO and MIMO configuration. The broadcast phase coding strategies were further investigated, and a MU-MIMO-based scheme was proposed, which together with the interference cancelation receiver can outperform multiple antenna network coding with transmit and receive diversity techniques. The performance of the MU-MIMO approach has been verified for several well-known linear precoding algorithms, such as Zero Forcing (ZF) or Block Diagonalization (BD), as well as for the Maximum Ratio Transmission (MRT) precoding algorithm proposed in this paper.

The rest of this chapter is organized as follows. In Section 4.2, we describe the system setup. Section 4.3 illustrates the multiple access phase. In Section 4.4, the broadcast phase is analyzed, the network coding scenario described, and the proposed MU-MIMO-based solution is motivated. The results of the link-level simulation are provided in Section 4.5. Section 4.6 concludes the chapter.

This chapter is based on the articles [27], [28] and [29] previously published by the author. In [27] MU-MIMO technology was explored with a focus on various precoding algorithms for MU-MIMO transmission in LTE-Advanced. The comparison of network coding and MU-MIMO techniques in a two-way relaying scenario was addressed in [28], with simulations based on specific parameters of the physical layer of the LTE. To verify these results, the article [29] presented the system performance simulated using the IMT-Advanced radio channel model in which the correlation between antennas was introduced. In this chapter, the author's earlier research has been updated to ensure compatibility with NR numerology and the recent 3GPP standards along with an additional verification for a wider range of multi-antenna scenarios.

Notations: $(.)^T$ and $(.)^H$ represent vector/matrix transpose and Hermitian transpose, respectively. $(.)^\dagger$ denotes the Moore-Penrose pseudoinverse. $|\boldsymbol{x}|$ stands for 2-norm of vextor $\boldsymbol{x}$. $span(\boldsymbol{a})$ represents the subspace spanned by a vector $\boldsymbol{a}$. $ran(\boldsymbol{H})$ denotes the range (column space) of matrix $\boldsymbol{H}$. $\langle \boldsymbol{x} \rangle$ represents normalization operation on vector $\boldsymbol{x}$, i.e. $\langle \boldsymbol{x} \rangle = \frac{\boldsymbol{x}}{|x|}$.

4.2 System model

In this chapter, the author proposes a new transmission scheme, called Maximum Ration Transmission (MRT) for the two-way relaying channel (TWR-MRT). The considered two-way relaying scenario is shown in Fig. 4.1 and comprises one Relay Station (RS), such that MS and BS can communicate through the relay. As described in chapter 3 in the traditional solution of two-way relaying, four time slots are needed in the TDD mode to exchange data blocks between two stations. In the considered scenario, the number of slots is reduced to two; however, the two slots are achieved through multi-antenna transmission (MIMO) instead of applying PNC/NC schemes. These time slots are the so-called multiple access slot (MA) and the broadcast slot (BC).

MIMO refers to a collection of signal processing techniques that have been developed to enhance the performance of wireless communication systems using multiple antennas at the transmitter, receiver or at both of them. MIMO technique was initially used for single-user data transmission (SU-MIMO), where there is only one transmitting and one receiving node, and the transmitter and receiver has multiple antennas. However, with the development of multi-user transmission technologies, several multiuser types of MIMO were derived, such as MU-MIMO and Cooperative MIMO (CO-

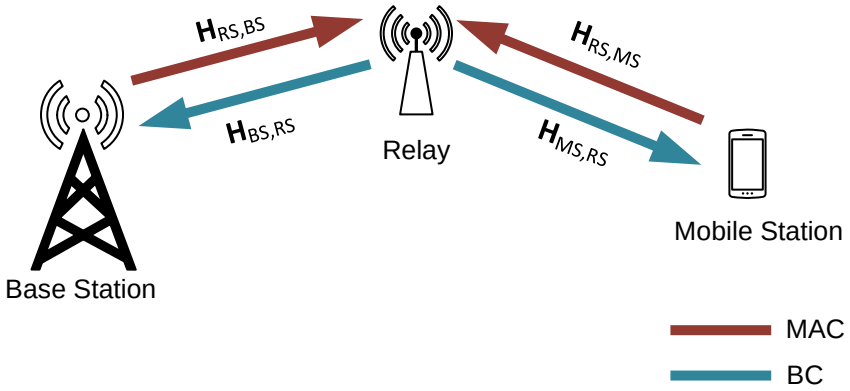

Figure 4.1: Considered two-way relaying scenario

MIMO). In the MU-MIMO there is one multi-antenna transmitting node and multiple receiving nodes. While SU-MIMO increases the throughput of one user, MU-MIMO allows increasing the overall capacity of the system. Cooperative MIMO, also known as network MIMO, distributed MIMO or virtual MIMO, combines multiple wireless devices into a virtual multi-antenna system, so that the neighboring transmitters can send data concurently to other users emulating a multi-antenna node.

In the multiple access time slot, MS and BS transmit their data to RS using the cooperative MIMO technique. Both stations use the same time and frequency resources during transmission. The RS jointly detects two data blocks, performs soft decoding of received codewords, and finds information blocks transmitted by MS and BS. In the broadcast phase, RS uses MU-MIMO to communicate with BS and MS simultaneously, using the same radio resources. Let us assume one BS, one RS and one MS user with $N_{T_{BS}}$, $N_{T_{RS}}$, $N_{T_{MS}}$ transmit antennas and $N_{R_{BS}}$, $N_{R_{RS}}$, $N_{R_{MS}}$ receive antennas, respectively. Furthermore, we assume that the MIMO channel between node A and node B is perfectly known at the receiving node and can be described by the $N_{R_B} \times N_{T_A}$ channel matrix $\boldsymbol{H}_{B,A}$.

4.3 Multiple Access Phase

To make full use of spatial multiplexing MIMO and to decrease the number of required time slots, Cooperative MIMO has been adopted in the first transmission phase. Cooperative communication is in a certain way inspired by the idea of spatial diversity that also motivated MIMO systems. In CO-MIMO the functionality of multi-antenna systems is emulated by grouping transmitting devices to operate as a virtual MIMO system.

Fig. 4.2 illustrates the system model during the MAC phase for the scenario where both source nodes are equipped with a single transmit antenna and the relay has two receive antennas. This setup represents the minimum possible configuration, since to receive two data streams at the same time and frequency resources, the system's multiplexing gain, which is $min(N_{T_{BS}} + N_{T_{MS}}, N_{R_{RS}})$, must be equal to two.

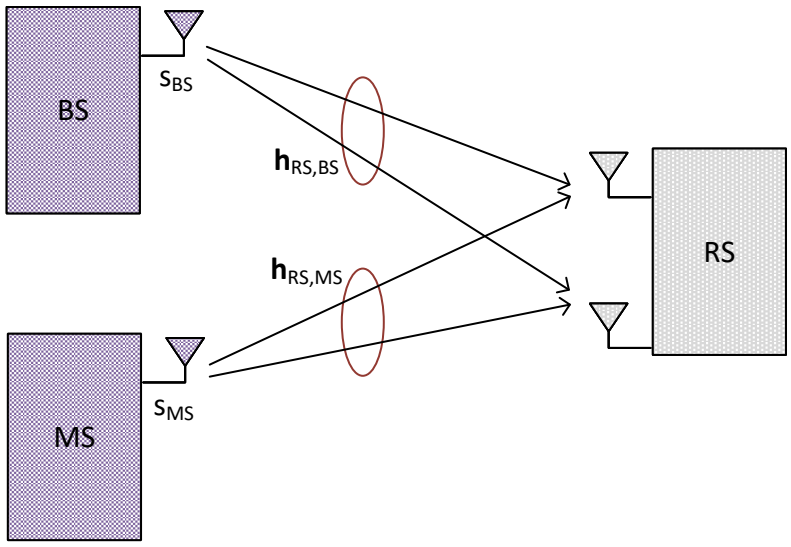

Figure 4.2: MAC channel

Suppose a flat fading channel, the channel coefficients between BS/MS and RS form a $N_{R_{RS}} \times (N_{T_{BS}} + N_{T_{MS}})$ channel matrix $\boldsymbol{H}_{RS} = [\boldsymbol{h}_{BS}\ \boldsymbol{h}_{MS}]$. Such a channel model reflects a transmission on a single subcarrier of the MIMO-OFDM system. If the message sent by the BS and MS is denoted as s_{BS} and s_{MS} respectively, and assuming frequency synchronization of both signals, the combined signal received by the relay may be expressed as:

$$\boldsymbol{y}_{RS} = \boldsymbol{H}_{RS}\boldsymbol{s} + \boldsymbol{n}_{RS} \tag{4.1}$$

or more detailed as

$$\begin{bmatrix} y_{RS_1} \\ y_{RS_2} \end{bmatrix} = \begin{bmatrix} h_{RS_1,BS} & h_{RS_1,MS} \\ h_{RS_2,BS} & h_{RS_2,MS} \end{bmatrix} \cdot \begin{bmatrix} s_{BS} \\ s_{MS} \end{bmatrix} + \begin{bmatrix} n_{RS_1} \\ n_{RS_2} \end{bmatrix} \tag{4.2}$$

where y_{RS_1} and y_{RS_2} are the received symbols for the first and second RS antenna, respectively. The channel coefficients $h_{RS_i,BS}$ and $h_{RS_i,MS}$ represent channel attenuation between BS/MS and RS, seen on the i-th receive antenna. Let us assume that all channel coefficients are zero-mean and mutually uncorrelated. n_{RS_1} and n_{RS_2} are the white Gaussian noise samples.

Typical receivers in a MIMO-OFDM system may be categorized according to their type of signal processing, e.g. they may be nonlinear or linear. The three most common

receivers for uncoded spatial multiplexing are Maximum Likelihood (ML), ZF and Minimum Mean Square Error (MMSE), where ML is a nonlinear receiver, while ZF and MMSE are linear. The efficiency of a system will strongly depend on the selected decoding algorithm.

4.3.1 Maximum Likelihood

ML decoding is the optimal decoding algorithm, however it requires an exhaustive search over all possible combinations of transmitted symbols, thus its computational complexity is often too high. Assuming equally likely, temporally uncoded trasmit symbols, the ML decoder chooses the vector $\boldsymbol{x}$ that solves

$$\tilde{\boldsymbol{s}} = \begin{bmatrix} \tilde{s}_{BS} \\ \tilde{s}_{MS} \end{bmatrix} = \underset{\boldsymbol{s}}{\operatorname{argmin}} \, ||\boldsymbol{y_{RS}} - \boldsymbol{H}_{RS}\boldsymbol{s}||_2^2 \tag{4.3}$$

where $\boldsymbol{s} = \begin{bmatrix} s_{BS} \\ s_{MS} \end{bmatrix}$ and $||.||_2$ is a Euclidean norm.

4.3.2 Zero Forcing

The complexity of the ML receiver can be reduced by using a linear filter to separate the transmitted data streams and decode them independently. The ZF detector transforms the received vector using the pseudoinverse of the channel matrix $\boldsymbol{H}_{RS}$. The ZF equalizer, denoted by $\boldsymbol{G}_{ZF}^H$ is given by

$$\boldsymbol{G}_{ZF}^H = \left(\boldsymbol{H}_{RS}^H \boldsymbol{H}_{RS}\right)^{-1} \boldsymbol{H}_{RS}^H \tag{4.4}$$

The output of the ZF receiver is equal to

$$\begin{aligned} \tilde{\boldsymbol{s}} = \begin{bmatrix} \tilde{s}_{BS} \\ \tilde{s}_{MS} \end{bmatrix} &= \boldsymbol{G}_{ZF}^H \boldsymbol{y_{RS}} \Rightarrow \\ &= \boldsymbol{G}_{ZF}^H \boldsymbol{H}_{RS}\boldsymbol{s} + \boldsymbol{G}_{ZF}^H \boldsymbol{n}_{RS} \Rightarrow \\ &= \left(\boldsymbol{H}_{RS}^H \boldsymbol{H}_{RS}\right)^{-1} \boldsymbol{H}_{RS}^H \boldsymbol{H}_{RS}\boldsymbol{s} + \boldsymbol{G}_{ZF}^H \boldsymbol{n}_{RS} \Rightarrow \\ &= \boldsymbol{s} + \boldsymbol{G}_{ZF}^H \boldsymbol{n}_{RS} \end{aligned} \tag{4.5}$$

Let us note that SNR can be different in two links, i.e. between MS and RS and between BS and RS. Under the assumption of zero-mean and mutual uncorrelated data symbols s_{BS} and s_{MS} and white Gaussian and mutually uncorrelated noise samples n_{RS_1} and n_{RS_2} we can find the values of SNR for each link in the main diagonal of the following matrix

$$\boldsymbol{\Gamma}_{ZF} = E\left[\mathbf{s}\mathbf{s}^H\right] \cdot \left(E\left[(\mathbf{G}_{ZF}^H \mathbf{n}_{RS})(\mathbf{G}_{ZF}^H \mathbf{n}_{RS})^H\right]\right)^{-1} \tag{4.6}$$

Since the equalizer coefficients do not depend on the noise samples, we can treat $\boldsymbol{G}_{ZF}^{H}$ and $\boldsymbol{n}_{RS}$ as independent. Therefore, recalling that data symbols are zero-mean, uncorrelated and have the mean power equal to P_s we can write

$$\begin{aligned}
\boldsymbol{\Gamma}_{ZF} &= P_s \boldsymbol{I} \left(\mathbf{E} \left[\boldsymbol{G}_{ZF}^{H} \boldsymbol{n}_{RS} \boldsymbol{n}_{RS}{}_{ZF}^{H} \right] \right)^{-1} \\
&= P_s \boldsymbol{I} \left(\sigma_n^2 \mathbf{E} \left[\boldsymbol{G}_{ZF}^{H} \boldsymbol{I} \boldsymbol{G}_{ZF} \right] \right)^{-1} \\
&= P_s \boldsymbol{I} \left(\sigma_n^2 \mathbf{E} \left[(\boldsymbol{H}_{RS}^{H} \boldsymbol{H}_{RS})^{-1} \boldsymbol{H}_{RS}^{H} \boldsymbol{H}_{RS} \left((\boldsymbol{H}_{RS}^{H} \boldsymbol{H}_{RS})^{-1} \right)^{H} \right] \right)^{-1} \\
&= P_s \boldsymbol{I} \left(\sigma_n^2 \mathbf{E} \left[\left((\boldsymbol{H}_{RS}^{H} \boldsymbol{H}_{RS})^{-1} \right)^{H} \right] \right)^{-1}
\end{aligned} \tag{4.7}$$

Let us note that

$$\begin{aligned}
\mathbf{E}\left[\boldsymbol{H}_{RS}^{H}\boldsymbol{H}_{RS}\right] &= \mathbf{E}\left\{ \begin{bmatrix} h_{RS_1,BS}^{*} & h_{RS_2,BS}^{*} \\ h_{RS_1,MS}^{*} & h_{RS_2,MS}^{*} \end{bmatrix} \cdot \begin{bmatrix} h_{RS_1,BS} & h_{RS_1,MS} \\ h_{RS_2,BS} & h_{RS_2,MS} \end{bmatrix} \right\} \\
&= \mathbf{E}\left\{ \begin{bmatrix} |h_{RS_1,BS}|^2 + |h_{RS_2,BS}|^2 & h_{RS_1,BS}^{*} h_{RS_1,MS} + h_{RS_2,BS}^{*} h_{RS_2,MS} \\ h_{RS_1,MS}^{*} h_{RS_1,BS} + h_{RS_2,MS}^{*} h_{RS_2,BS} & |h_{RS_1,MS}|^2 + |h_{RS_2,MS}|^2 \end{bmatrix} \right\} \\
&= \begin{bmatrix} \mathbf{E}[|h_{RS_1,BS}|^2] + \mathbf{E}[|h_{RS_2,BS}|^2] & 0 \\ 0 & \mathbf{E}[|h_{RS_1,MS}|^2] + \mathbf{E}[|h_{RS_2,MS}|^2] \end{bmatrix}
\end{aligned}$$

If we assume that $P_s = 1$ is a total transmitted power per each source and σ_n^2 is a noise variance then the expression for SNR can be formulated in the following way:

$$\boldsymbol{\Gamma}_{ZF} = \begin{bmatrix} \frac{\left|\left|h_{RS,BS}\right|\right|_2^2}{\sigma_n^2} & 0 \\ 0 & \frac{\left|\left|h_{RS,MS}\right|\right|_2^2}{\sigma_n^2} \end{bmatrix} \tag{4.8}$$

Thus, the ZF equalizer completely cancels the interference from other streams, however, it requires careful consideration of matrix inversion and noise amplification effects.

4.3.3 Minimum Mean Square Error Estimation

The MMSE receiver minimizes the expected value of the mean square error between the transmitted vector $\boldsymbol{s}$ and the estimated vector. Therefore, the MMSE criterion can be formulated as follows.

$$\min_{\boldsymbol{s}} \mathbf{E}\left[\left|\left| \boldsymbol{s} - \boldsymbol{G}_{MMSE}^{H} \boldsymbol{y}_{RS} \right|\right|_2^2 \right] \tag{4.9}$$

The solution of the above minimization problem is given by

$$\boldsymbol{G}_{MMSE}^{H} = \left(\boldsymbol{H}_{RS}^{H} \boldsymbol{H}_{RS} + \sigma_n^2 \boldsymbol{I}_{N_T} \right)^{-1} \boldsymbol{H}_{RS}^{H} \tag{4.10}$$

where $N_T = N_{T_{BS}} + N_{T_{MS}}$. The MMSE equalizer output is equal to

$$\begin{aligned}\tilde{\boldsymbol{s}} = \begin{bmatrix}\tilde{s}_{BS}\\ \tilde{s}_{MS}\end{bmatrix} &= \boldsymbol{G}^H_{MMSE}\boldsymbol{y}_{RS} \Rightarrow \\ &= \boldsymbol{G}^H_{MMSE}\boldsymbol{s} + \boldsymbol{G}^H_{MMSE}\boldsymbol{n}_{RS} \Rightarrow \\ &= \left(\boldsymbol{H}^H_{RS}\boldsymbol{H}_{RS} + \sigma_n^2\boldsymbol{I}_{N_T}\right)^{-1}\boldsymbol{H}^H_{RS}\boldsymbol{H}_{RS}\boldsymbol{s} + \boldsymbol{G}^H_{MMSE}\boldsymbol{n}_{RS}\end{aligned} \tag{4.11}$$

The MMSE detector combines the advantages of the Matched Filter (MF) and ZF receivers. At high SNRs, which correspond to small values σ_n^2, the MMSE equalizer acts similarly to a ZF receiver, whereas at low SNRs (high σ_n^2) it behaves more like MF [30]. The detailed analysis and derivation of the output SNR of the MMSE receiver can be found in [31], [32], [33] and [34].

4.4 Broadcast Phase

During the second phase of two-way relaying, the decoded information blocks received by RS from both end stations are broadcast to MS and BS using the same time and frequency resources. In the proposed solution, savings in transmission time resources during the broadcast phase are achieved by performing MU-MIMO on separated signal streams for BS and MS. The alternative solution is to perform a simple network coding in which the relay node performs XOR operation with massages dedicated to base and mobile stations. The network coding scheme will be described in Section 4.4.1. Section 4.4.2 presents the scenario with the MU-MIMO scheme with a focus on classic MU-MIMO solutions known from the literature and MU-MIMO with the MRT precoding, proposed by the author of this dissertation.

4.4.1 Network coding

In the network coding scenario, RS starts with the determination of the binary sum (XOR) of the received information bit blocks. Subsequently, the codeword is calculated in the LDPC encoder and its bits are mapped onto data symbols of the appropriate number of the OFDM symbols. The RS broadcasts the produced signal to the BS and MS, which receive the transmitted signal, decode it using the applied LDPC decoder and, as a result, obtain the modulo-2 sum of the BS and MS information blocks. Having their own information block stored in their buffers, both stations are able to determine the other station's information block by modulo-2 summing the decoded block with the own one.

Since the RS inherently uses at least two antennas in the multiple access phase, they may also be applied in the broadcast phase to perform transmit diversity. The transmit diversity scheme adopted in the considered scenario is consistent with the

3GPP standard [10] and assumes no Channel State Information at the Transmitter (CSIT). In such a case, the data signals are processed at the transmitter in a way that allows the receiver to exploit the spatial diversity of the received signals. The performance of transmit diversity can be improved by the joint design of coding, modulation, and multiple antenna transmission. Coding techniques dedicated to the multiantenna scenario are called Space-Time Block Codes (STBC). Coding redundancy is added in the spatial and temporal domains without sacrificing bandwidth. STBC codes were first introduced by Siavash Alamouti in [35], later adapted to Space-Frequency Block Codes (SFBC), and included in the 3GPP LTE standard in this form. In SFBC the encoding is performed in the frequency domain of the antenna, whereas in STBC in the time domain. Fig. 4.3 presents the network coding with two antenna transmit diversity in the broadcast phase with two receiving antennas at BS and MS.

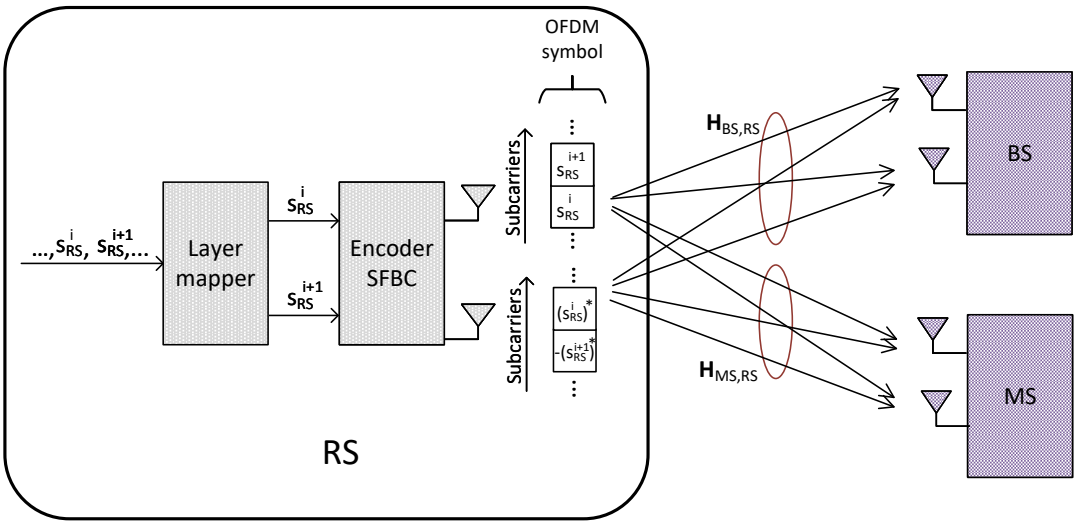

Figure 4.3: Network coding with 2 antenna SFBC

Relay station transmits symbol vector $\boldsymbol{s}_{RS} = [s^0_{RS}, ..., s^i_{RS}, ...s^{M_{symb}}_{RS}]$, where M_{symb} is the number of symbols to be transmitted. In case of two transmit antennas, symbols are divided into two layers, with all even-indexed symbols placed in the first layer and odd-indexed symbols in the second layer. The layers are then passed to the SFBC encoder, which transforms the symbols and maps them onto two consecutive subcarriers at each antenna. Symbols received by the BS and MS may be written as follows:

$$\begin{bmatrix} \boldsymbol{y}^{sc}_{BS} \\ \boldsymbol{y}^{sc+1}_{BS} \end{bmatrix} = \begin{bmatrix} \boldsymbol{H}^{sc}_{RS,BS} & \boldsymbol{0} \\ \boldsymbol{0} & \boldsymbol{H}^{sc+1}_{RS,BS} \end{bmatrix} \cdot \boldsymbol{s} + \begin{bmatrix} \boldsymbol{n}^{sc}_{BS} \\ \boldsymbol{n}^{sc+1}_{BS} \end{bmatrix} \tag{4.12}$$

$$\begin{bmatrix} \boldsymbol{y}^{sc}_{MS} \\ \boldsymbol{y}^{sc+1}_{MS} \end{bmatrix} = \begin{bmatrix} \boldsymbol{H}^{sc}_{RS,MS} & \boldsymbol{0} \\ \boldsymbol{0} & \boldsymbol{H}^{sc+1}_{RS,MS} \end{bmatrix} \cdot \boldsymbol{s} + \begin{bmatrix} \boldsymbol{n}^{sc}_{MS} \\ \boldsymbol{n}^{sc+1}_{MS} \end{bmatrix} \tag{4.13}$$

where $\boldsymbol{y}_{BS}^{sc}$, $\boldsymbol{y}_{BS}^{sc+1}$ and $\boldsymbol{y}_{MS}^{sc}$, $\boldsymbol{y}_{MS}^{sc+1}$ are the received signals on the sc-th and $sc+1$-st subcarrier at BS and MS, recpectively. $\boldsymbol{s}$ is the transmitted symbol vector after SFBC encoding of symbols $\boldsymbol{s}_{RS}^{i}$ and $\boldsymbol{s}_{RS}^{i+1}$. In case of two transmit antennas, $\boldsymbol{s}$ takes form (according to LTE stanard):

$$\boldsymbol{s} = \frac{1}{\sqrt{2}} \begin{bmatrix} s^{i} \\ -\left(s^{i+1}\right)^{*} \\ s^{i+1} \\ \left(s^{i}\right)^{*} \end{bmatrix} \tag{4.14}$$

When using the four-transmit diversity, the combination of SFBC and Frequency Switched Transmit Diveristy (FSTD) is applied [36]. The main principle of operation of the FSTD scheme is that a pair of modulated symbols is transmitted using the SFBC on two of the four antennas, while the other two antennas remain inactive. The active pair of antenna ports switches with each subcarrier. The signal received from four antenna RS by BS and MS, may be written as

$$\begin{bmatrix} \boldsymbol{y}_{BS}^{sc} \\ \boldsymbol{y}_{BS}^{sc+1} \\ \boldsymbol{y}_{BS}^{sc+2} \\ \boldsymbol{y}_{BS}^{sc+3} \end{bmatrix} = \begin{bmatrix} \boldsymbol{H}_{RS,BS}^{sc} & \mathbf{0} & \mathbf{0} & \mathbf{0} \\ \mathbf{0} & \boldsymbol{H}_{RS,BS}^{sc+1} & \mathbf{0} & \mathbf{0} \\ \mathbf{0} & \mathbf{0} & \boldsymbol{H}_{RS,BS}^{sc+2} & \mathbf{0} \\ \mathbf{0} & \mathbf{0} & \mathbf{0} & \boldsymbol{H}_{RS,BS}^{sc+3} \end{bmatrix} \cdot \boldsymbol{s} + \begin{bmatrix} \boldsymbol{n}_{BS}^{sc} \\ \boldsymbol{n}_{BS}^{sc+1} \\ \boldsymbol{n}_{BS}^{sc+2} \\ \boldsymbol{n}_{BS}^{sc+3} \end{bmatrix} \tag{4.15}$$

$$\begin{bmatrix} \boldsymbol{y}_{MS}^{sc} \\ \boldsymbol{y}_{MS}^{sc+1} \\ \boldsymbol{y}_{MS}^{sc+2} \\ \boldsymbol{y}_{MS}^{sc+3} \end{bmatrix} = \begin{bmatrix} \boldsymbol{H}_{RS,MS}^{sc} & \mathbf{0} & \mathbf{0} & \mathbf{0} \\ \mathbf{0} & \boldsymbol{H}_{RS,MS}^{sc+1} & \mathbf{0} & \mathbf{0} \\ \mathbf{0} & \mathbf{0} & \boldsymbol{H}_{RS,MS}^{sc+2} & \mathbf{0} \\ \mathbf{0} & \mathbf{0} & \mathbf{0} & \boldsymbol{H}_{RS,MS}^{sc+3} \end{bmatrix} \cdot \boldsymbol{s} + \begin{bmatrix} \boldsymbol{n}_{MS}^{sc} \\ \boldsymbol{n}_{MS}^{sc+1} \\ \boldsymbol{n}_{MS}^{sc+2} \\ \boldsymbol{n}_{MS}^{sc+3} \end{bmatrix} \tag{4.16}$$

where symbols transmitted from four antennas take the form

$$\boldsymbol{s} = \frac{1}{\sqrt{2}} \begin{bmatrix} s^{i} \\ 0 \\ -\left(s^{i+1}\right)^{*} \\ 0 \\ s^{i+1} \\ 0 \\ \left(s^{i}\right)^{*} \\ 0 \\ 0 \\ s^{i+2} \\ 0 \\ -\left(s^{i+3}\right)^{*} \\ 0 \\ s^{i+3} \\ 0 \\ \left(s^{i+2}\right)^{*} \end{bmatrix} \tag{4.17}$$

4.4.1.1 Equalizer and determination of output SNR

Depending on the abilities of the MS and BS participating in the two-way relaying process, the Multiple-Input Single-Output (MISO) and MIMO configurations have been considered and verified through simulations. The following calculations will demonstrate the design of the equalizer developed and implemented by the author to recover transmitted data symbols s_i and s_{i+1} using the 2×2 SFBC scenario as an example (an analog receiver is implemented for four transmit antennas). Furthermore, the output SNR of such a system is derived by the author and is presented below. In general, equations (4.12) and (4.13) may be generalized to

$$\begin{bmatrix} \boldsymbol{y}^{sc} \\ \boldsymbol{y}^{sc+1} \end{bmatrix} = \begin{bmatrix} \boldsymbol{H}^{sc} & \boldsymbol{0} \\ \boldsymbol{0} & \boldsymbol{H}^{sc+1} \end{bmatrix} \cdot \boldsymbol{s} + \begin{bmatrix} \boldsymbol{n}^{sc} \\ \boldsymbol{n}^{sc+1} \end{bmatrix} \tag{4.18}$$

The channel experienced between each transmit and receive antennas is varying randomly in time. However, it is assumed that the channel will remain constant over two consecutive subcarriers. Thus, we can write:

$$\boldsymbol{H} = \boldsymbol{H}^{sc} = \boldsymbol{H}^{sc+1} \tag{4.19}$$

$$\begin{bmatrix} \boldsymbol{y}^{sc} \\ \boldsymbol{y}^{sc+1} \end{bmatrix} = \begin{bmatrix} \boldsymbol{H} & 0 \\ 0 & \boldsymbol{H} \end{bmatrix} \cdot \boldsymbol{s} + \begin{bmatrix} \boldsymbol{n}^{sc} \\ \boldsymbol{n}^{sc+1} \end{bmatrix} = \begin{bmatrix} h_{11} & h_{12} & 0 & 0 \\ h_{21} & h_{22} & 0 & 0 \\ 0 & 0 & h_{11} & h_{12} \\ 0 & 0 & h_{21} & h_{22} \end{bmatrix} \cdot \boldsymbol{s} + \begin{bmatrix} \boldsymbol{n}^{sc} \\ \boldsymbol{n}^{sc+1} \end{bmatrix} \tag{4.20}$$

After changing the order of symbols in vecor $\boldsymbol{s}$:

$$\begin{bmatrix} \boldsymbol{y}^{sc} \\ \hat{\boldsymbol{y}}^{sc+1} \end{bmatrix} = \frac{1}{\sqrt{2}} \begin{bmatrix} h_{11} & h_{12} & 0 & 0 \\ h_{21} & h_{22} & 0 & 0 \\ 0 & 0 & h_{12} & h_{11} \\ 0 & 0 & h_{22} & h_{21} \end{bmatrix} \cdot \begin{bmatrix} s^i \\ -\left(s^{i+1}\right)^* \\ \left(s^i\right)^* \\ s^{i+1} \end{bmatrix} + \begin{bmatrix} \boldsymbol{n}^{sc} \\ \hat{\boldsymbol{n}}^{sc+1} \end{bmatrix} \tag{4.21}$$

After complex conjugation of $\hat{\boldsymbol{y}}^{sc+1}$:

$$\begin{bmatrix} \boldsymbol{y}^{sc} \\ \left(\hat{\boldsymbol{y}}^{sc+1}\right)^* \end{bmatrix} = \frac{1}{\sqrt{2}} \begin{bmatrix} h_{11} & h_{12} & 0 & 0 \\ h_{21} & h_{22} & 0 & 0 \\ 0 & 0 & \left(h_{12}\right)^* & \left(h_{11}\right)^* \\ 0 & 0 & \left(h_{22}\right)^* & \left(h_{21}\right)^* \end{bmatrix} \cdot \begin{bmatrix} s^i \\ -\left(s^{i+1}\right)^* \\ s^i \\ \left(s^{i+1}\right)^* \end{bmatrix} + \begin{bmatrix} \boldsymbol{n}^{sc} \\ \left(\hat{\boldsymbol{n}}^{sc+1}\right)^* \end{bmatrix} \tag{4.22}$$

After moving the "-" sign from vector $\boldsymbol{s}$ to matrix $\boldsymbol{H}$:

$$\begin{bmatrix} \boldsymbol{y}^{sc} \\ \left(\hat{\boldsymbol{y}}^{sc+1}\right)^* \end{bmatrix} = \frac{1}{\sqrt{2}} \begin{bmatrix} h_{11} & -h_{12} & 0 & 0 \\ h_{21} & -h_{22} & 0 & 0 \\ 0 & 0 & \left(h_{12}\right)^* & \left(h_{11}\right)^* \\ 0 & 0 & \left(h_{22}\right)^* & \left(h_{21}\right)^* \end{bmatrix} \cdot \begin{bmatrix} s^i \\ \left(s^{i+1}\right)^* \\ s^i \\ \left(s^{i+1}\right)^* \end{bmatrix} + \begin{bmatrix} \boldsymbol{n}^{sc} \\ \left(\hat{\boldsymbol{n}}^{sc+1}\right)^* \end{bmatrix} \tag{4.23}$$

Equation (4.23) may now be written as

$$\hat{\boldsymbol{y}} = \begin{bmatrix} \boldsymbol{y}^{sc} \\ \left(\hat{\boldsymbol{y}}^{sc+1}\right)^* \end{bmatrix} = \frac{1}{\sqrt{2}} \begin{bmatrix} h_{11} & -h_{12} \\ h_{21} & -h_{22} \\ \left(h_{12}\right)^* & \left(h_{11}\right)^* \\ \left(h_{22}\right)^* & \left(h_{21}\right)^* \end{bmatrix} \cdot \begin{bmatrix} s^i \\ \left(s^{i+1}\right)^* \end{bmatrix} + \begin{bmatrix} \boldsymbol{n}^{sc} \\ \left(\hat{\boldsymbol{n}}^{sc+1}\right)^* \end{bmatrix} \tag{4.24}$$

For the ZF linear receiver, we apply the equalizer matrix:

$$\boldsymbol{G}^H = \left(\hat{\boldsymbol{H}}^H \hat{\boldsymbol{H}}\right)^{-1} \hat{\boldsymbol{H}}^H \tag{4.25}$$

where

$$\hat{\boldsymbol{H}} = \frac{1}{\sqrt{2}} \begin{bmatrix} h_{11} & -h_{12} \\ h_{21} & -h_{22} \\ \left(h_{12}\right)^* & \left(h_{11}\right)^* \\ \left(h_{22}\right)^* & \left(h_{21}\right)^* \end{bmatrix} \tag{4.26}$$

The term $\hat{\boldsymbol{H}}^H \hat{\boldsymbol{H}}$ equals

$$\begin{aligned} \hat{\boldsymbol{H}}^H \hat{\boldsymbol{H}} &= \frac{1}{\sqrt{2}} \begin{bmatrix} \left(h_{11}\right)^* & \left(h_{21}\right)^* & h_{12} & h_{22} \\ -\left(h_{12}\right)^* & -\left(h_{22}\right)^* & h_{11} & h_{21} \end{bmatrix} \cdot \frac{1}{\sqrt{2}} \begin{bmatrix} h_{11} & -h_{12} \\ h_{21} & -h_{22} \\ \left(h_{12}\right)^* & \left(h_{11}\right)^* \\ \left(h_{22}\right)^* & \left(h_{21}\right)^* \end{bmatrix} \\ &= \frac{1}{2} \begin{bmatrix} |h_{11}|^2 + |h_{12}|^2 + |h_{21}|^2 + |h_{22}|^2 & 0 \\ 0 & |h_{11}|^2 + |h_{12}|^2 + |h_{21}|^2 + |h_{22}|^2 \end{bmatrix} \\ &= \frac{1}{2} \|\boldsymbol{H}\|_F^2 \boldsymbol{I}_{2\times 2} \end{aligned} \tag{4.27}$$

where $\|.\|_F$ is the Frobenius norm. Since this is a diagonal matrix, the inverse is just the inverse of the diagonal elements, i.e.

$$\left(\hat{\boldsymbol{H}}^H\hat{\boldsymbol{H}}\right)^{-1} = \frac{2}{\|\boldsymbol{H}\|_F^2}\boldsymbol{I}_{2\times 2} \tag{4.28}$$

The detected signal is

$$\begin{bmatrix}\tilde{s}^i\\ \tilde{s}^{i+1}\end{bmatrix} = \boldsymbol{G}^H\hat{\boldsymbol{y}} = \boldsymbol{G}^H\hat{\boldsymbol{H}}\hat{\boldsymbol{s}} + \boldsymbol{G}^H\hat{\boldsymbol{n}} = \hat{\boldsymbol{s}} + \boldsymbol{G}^H\hat{\boldsymbol{n}} \tag{4.29}$$

where

$$\hat{\boldsymbol{s}} = \begin{bmatrix}s^i\\ (s^{i+1})^*\end{bmatrix} \tag{4.30}$$

$$\hat{\boldsymbol{n}} = \begin{bmatrix}\boldsymbol{n}^{sc}\\ (\hat{\boldsymbol{n}}^{sc+1})^*\end{bmatrix} \tag{4.31}$$

As seen in equation (4.29) for the considered tranmission scheme, two consecutive received symbols are equalized jointly. The output SNR for each symbol can be found along the main diagonal of the following matrix.

$$\boldsymbol{\Gamma}_{NC} = \mathbf{E}\left[\hat{\boldsymbol{s}}\left(\hat{\boldsymbol{s}}\right)^H\right]\cdot\left(\mathbf{E}\left[\boldsymbol{G}^H\hat{\boldsymbol{n}}\left(\boldsymbol{G}^H\hat{\boldsymbol{n}}\right)^H\right]\right)^{-1} \tag{4.32}$$

Since data symbols are zero-mean, uncorrelated, and $|s^i|^2 = 1$ we can write

$$\mathbf{E}\left[\hat{\boldsymbol{s}}\left(\hat{\boldsymbol{s}}\right)^H\right] = \begin{bmatrix}\mathbf{E}\left[|s^i|^2\right] & 0\\ 0 & \mathbf{E}\left[|s^{i+1}|^2\right]\end{bmatrix} = \begin{bmatrix}1 & 0\\ 0 & 1\end{bmatrix} = \boldsymbol{I}_{2\times 2} \tag{4.33}$$

The equalizer coefficients calculated according to (4.25) do not depend on noise samples, thus we can treat $\boldsymbol{G}$ and $\hat{\boldsymbol{n}}$ as independent. Therefore,

$$\begin{aligned}\mathbf{E}\left[\boldsymbol{G}^H\hat{\boldsymbol{n}}\left(\boldsymbol{G}^H\hat{\boldsymbol{n}}\right)^H\right] &= \mathbf{E}\left[\boldsymbol{G}^H\hat{\boldsymbol{n}}\hat{\boldsymbol{n}}^H\boldsymbol{G}\right]\\ &= \sigma_n^2\cdot\mathbf{E}\left[\left(\hat{\boldsymbol{H}}^H\hat{\boldsymbol{H}}\right)^{-1}\hat{\boldsymbol{H}}^H\hat{\boldsymbol{H}}\left(\left(\hat{\boldsymbol{H}}^H\hat{\boldsymbol{H}}\right)^H\right)^{-1}\right]\\ &= \sigma_n^2\cdot\mathbf{E}\left[\frac{2}{\|\boldsymbol{H}\|_F^2}\frac{\|\boldsymbol{H}\|_F^2}{2}\frac{2}{\|\boldsymbol{H}\|_F^2}\boldsymbol{I}_{2\times 2}\right]\\ &= \frac{2\sigma_n^2}{\|\boldsymbol{H}\|_F^2}\boldsymbol{I}_{2\times 2}\end{aligned} \tag{4.34}$$

Based on equations (4.33) and (4.34), the detected SNR for two consecutive symbols, may be rewritten as

$$\boldsymbol{\Gamma}_{\boldsymbol{NC}} = \boldsymbol{I}_{2\times 2}\left(\frac{2\sigma_n^2}{\|\boldsymbol{H}\|_F^2}\boldsymbol{I}_{2\times 2}\right)^{-1} = \frac{\|\boldsymbol{H}\|_F^2}{2\sigma_n^2}\boldsymbol{I}_{2\times 2} = \frac{\sum_{i=1}^{r}\delta_i^2}{2\sigma_n^2}\boldsymbol{I}_{2\times 2} \tag{4.35}$$

where r is a rank of the channel matrix $\boldsymbol{H}$ and δ_i is its i-th singular value.

4.4.2 Multiuser MIMO

In the MU-MIMO scheme, the codewords for BS and MS are independently generated in their respective channel code encoders and then multiplied by the appropriate precoding vectors. The symbols intended for BS (s_{MS}) and MS (s_{BS}) are then combined and mapped to the antenna ports of the relay. Fig. 4.4 illustrates the broadcast phase using the MU-MIMO technique in the scenario with two transmit antennas at the relay and two receive antennas at BS and MS.

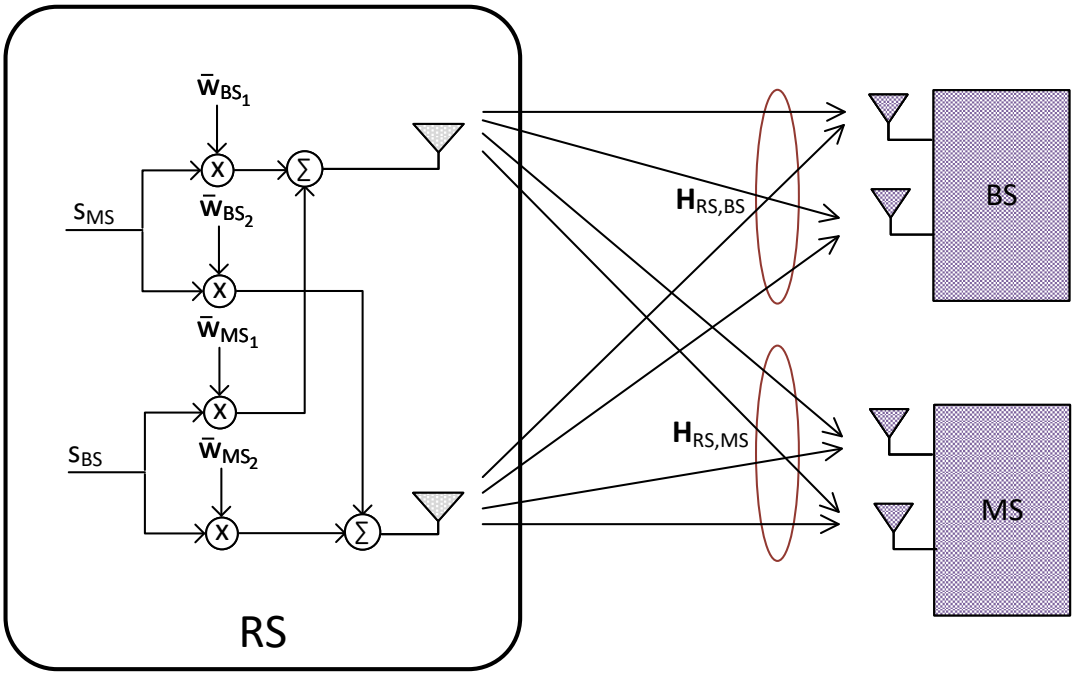

Figure 4.4: Two-way relaying system with MU-MIMO in broadcast phase

The resultant received signal vectors per subcarrier for the BS and MS are noted as follows

$$\boldsymbol{y}_{BS} = \boldsymbol{H}_{RS,BS}\bar{\boldsymbol{w}}_{BS}s_{MS} + \underbrace{\boldsymbol{H}_{RS,BS}\bar{\boldsymbol{w}}_{MS}s_{BS}}_{\text{interference}} + \boldsymbol{n}_{BS} \tag{4.36}$$

$$\boldsymbol{y}_{MS} = \boldsymbol{H}_{RS,MS}\bar{\boldsymbol{w}}_{MS}s_{BS} + \underbrace{\boldsymbol{H}_{RS,MS}\bar{\boldsymbol{w}}_{BS}s_{MS}}_{\text{interference}} + \boldsymbol{n}_{MS} \tag{4.37}$$

$$\bar{\boldsymbol{w}}_{BS} = \sqrt{p_{BS}}\boldsymbol{w}_{BS} = \sqrt{p_{BS}}\begin{bmatrix} w_{BS_1} \\ w_{BS_2} \end{bmatrix} \tag{4.38}$$

$$\bar{\boldsymbol{w}}_{MS} = \sqrt{p_{MS}}\boldsymbol{w}_{MS} = \sqrt{p_{MS}}\begin{bmatrix} w_{MS_1} \\ w_{MS_2} \end{bmatrix} \tag{4.39}$$

where $\boldsymbol{w}_{BS}$ and $\boldsymbol{w}_{MS}$ are the precoding vectors. p_{BS} and p_{MS} are the transmit signal power of the BS and MS data streams. Under the assumption of equal power distri-

bution across all users, each element $p_k = \frac{P}{K\|\boldsymbol{w}_k\|_2^2}$, $(k = 1, \cdots, K)$ where P is the total power constraint on the transmitted signal, and $\boldsymbol{w}_k$ is the k-th precoding vector. The elements of additive noise $\boldsymbol{n}_{BS}$ and $\boldsymbol{n}_{MS}$ are $CN(0, N_0)$.

The interference from multi-user transmission occurring in the received signal (according to equations (4.36) and (4.37)) in the BS and MS respectively, may be expressed as

$$\boldsymbol{I}_{BS} = \boldsymbol{H}_{RS,BS}\bar{\boldsymbol{w}}_{MS}\boldsymbol{s}_{BS} \tag{4.40}$$

$$\boldsymbol{I}_{MS} = \boldsymbol{H}_{RS,MS}\bar{\boldsymbol{w}}_{BS}\boldsymbol{s}_{MS} \tag{4.41}$$

We can see from equations (4.40) and (4.41) that interference is the product of three factors: the channel matrix, the data symbol desired to another station, and its normalized precoder. s_{BS} is the data symbol transmitted during the multiple access phase from BS to RS (for MS), while s_{MS} denotes the data block transmitted from MS to RS (for BS). In the classic MU-MIMO scheme, precoding matrices are chosen in a way to cancel interference to other users. The most common MU-MIMO algorithms are presented and described in Section 4.4.2.1. The solution proposed by the author is presented in Section 4.4.2.2.

4.4.2.1 Classic MU-MIMO

In the classic MU-MIMO scheme, for Gaussian MIMO broadcast channels, the capacity region may be achieved when Dirty Paper Coding (DPC) is applied [37]. Due to its high complexity, some suboptimal precoding techniques have emerged, such as Zero Forcing Beamforming (ZFBF) [38] [39], MMSE [38], Block Diagonalization (BD) or Multi User Block Diagonalization Beamforming (MU-BDBF) [40]. The main goal of these precoding techniques is to remove interference between signals transmitted on the same resources and intended for different end points. For comparison purposes, the ZFBF and BD precoding algorithms have been implemented and will be described in detail in this section.

The ZFBF algorithm is the most common linear precoding scheme that involves zero-forcing [41]. ZF precoder decouples the multi-user channel into multiple independent subchannels resulting in interference-free reception (that is, $\boldsymbol{H}_k\bar{\boldsymbol{w}}_j = 0$ for $k \neq j$). The ZFBF precoding matrix is expressed by the Moore-Penrose pseudoinverse of $\bar{\boldsymbol{H}} = \left[\boldsymbol{H}_{RS,BS}^T \; \boldsymbol{H}_{RS,MS}^T\right]$

$$\boldsymbol{W} = \bar{\boldsymbol{H}}^H \left(\bar{\boldsymbol{H}}\bar{\boldsymbol{H}}^H\right)^{-1} \tag{4.42}$$

where the precoding weights are the corresponding submatrices of $\boldsymbol{W} = [\boldsymbol{w}_{BS} \; \boldsymbol{w}_{MS}]$. The capacity of MU-MIMO scheme with ZF precoder does not increase with

$min(N_T, K)$ (as it is possible in the multiuser channel) due to significant SNR degradation at the receivers after inversion of ill-conditioned channels.

When the BD algorithm is applied, the precoding vectors $\boldsymbol{w}_{BS}$ and $\boldsymbol{w}_{MS}$ are chosen in such a way that $\boldsymbol{w}_{BS}$ lies in the null space of the channel matrix $\boldsymbol{H}_{RS,MS}$ and $\boldsymbol{w}_{MS}$ lays in the null space of channel matrix $\boldsymbol{H}_{RS,BS}$ as follows:

$$\boldsymbol{H}_{RS,BS} = \boldsymbol{U}_{BS} \left[\boldsymbol{\Lambda}_{BS}\ \boldsymbol{0}\right] \left[\boldsymbol{V}_{BS}\ \boldsymbol{W}_{MS}\right]^H \tag{4.43}$$

$$\boldsymbol{H}_{RS,MS} = \boldsymbol{U}_{MS} \left[\boldsymbol{\Lambda}_{BS}\ \boldsymbol{0}\right] \left[\boldsymbol{V}_{MS}\ \boldsymbol{W}_{BS}\right]^H \tag{4.44}$$

where $\boldsymbol{V}_{BS}$ and $\boldsymbol{V}_{MS}$ represent the right singular matrices associated with the non-zero singular values $\boldsymbol{\Lambda}_{BS}$ and $\boldsymbol{\Lambda}_{MS}$ respectively, and $\boldsymbol{W}_{MS}$ and $\boldsymbol{W}_{BS}$ correspond to the zero singular values. The vectors $\boldsymbol{w}_{BS}$ and $\boldsymbol{w}_{MS}$ are the first columns of the matrices $\boldsymbol{W}_{MS}$ and $\boldsymbol{W}_{BS}$, or additional columns when transmitting more than one data stream. Assuming that $\boldsymbol{H}_{RS,BS}$ and $\boldsymbol{H}_{RS,MS}$ are full rank, the transmitter must have at least as many antennas as the total number of receive antennas at the BS and MS combined in order to meet the dimensionality requirements needed to cancel interference for each user.

Similarly to the BD algorithm, MU-BDBF eliminates intra-cell interference using block diagonalization, but compared to BD it uses two beamforming matrices to precode one data stream [42]. The MU-BDBF precoding matrices take the following form.

$$\boldsymbol{W}_{BS} = \boldsymbol{B}_{BS}\boldsymbol{D}_{BS} \tag{4.45}$$

$$\boldsymbol{W}_{MS} = \boldsymbol{B}_{MS}\boldsymbol{D}_{MS} \tag{4.46}$$

where $\boldsymbol{B}_{BS}$ and $\boldsymbol{B}_{MS}$ are used for interference cancellation and are obtained as in BD algorithm:

$$\boldsymbol{H}_{RS,BS} = \boldsymbol{U}_{BS} \left[\boldsymbol{\Lambda}_{BS}\ \boldsymbol{0}\right] \left[\boldsymbol{V}_{BS}\ \boldsymbol{B}_{MS}\right]^H \tag{4.47}$$

$$\boldsymbol{H}_{RS,MS} = \boldsymbol{U}_{MS} \left[\boldsymbol{\Lambda}_{BS}\ \boldsymbol{0}\right] \left[\boldsymbol{V}_{MS}\ \boldsymbol{B}_{BS}\right]^H \tag{4.48}$$

and $\boldsymbol{D}_{BS}$ and $\boldsymbol{D}_{BS}$ are applied for power allocation and are calculated as

$$\boldsymbol{H}_{RS,BS}\boldsymbol{B}_{BS} = \boldsymbol{U}_{BS}\boldsymbol{\Sigma}_{BS}\boldsymbol{D}_{BS}^H \tag{4.49}$$

$$\boldsymbol{H}_{RS,MS}\boldsymbol{B}_{MS} = \boldsymbol{U}_{MS}\boldsymbol{\Sigma}_{MS}\boldsymbol{D}_{MS}^H \tag{4.50}$$

The vectors $\boldsymbol{w}_{BS}$ and $\boldsymbol{w}_{MS}$ correspond to the first columns of the matrices $\boldsymbol{W}_{BS}$ and $\boldsymbol{W}_{MS}$, respectively, or to the subsequent columns when multiple data streams are transmitted.

Equalizer and determination of the output SNR

Applying a linear MU-MIMO precoder to the transmitted data stream transforms equations (4.36) and (4.37) into

$$\boldsymbol{y}_{BS} = \boldsymbol{H}_{RS,BS}\bar{\boldsymbol{w}}_{BS}s_{MS} + \boldsymbol{n}_{BS} \tag{4.51}$$

$$\boldsymbol{y}_{MS} = \boldsymbol{H}_{RS,MS}\bar{\boldsymbol{w}}_{MS}s_{BS} + \boldsymbol{n}_{MS} \tag{4.52}$$

In general, the vector received by the k-th station may be written as

$$\boldsymbol{y}_k = \boldsymbol{H}_k\bar{\boldsymbol{w}}_k s_{kj} + \boldsymbol{n}_k \tag{4.53}$$

After receiving the vector $\boldsymbol{y}_k$, the signals from all the receiving antennas are weighted by a complex weight vector $\boldsymbol{g}_k = [g_{1k}, ..., g_{N_Rk}]^T$. The linear receiver $\boldsymbol{g}_k$ can be designed by ZF or MMSE criteria. The MMSE would obtain better performance, but in order to simplify the analysis, the ZF receiver will be assumed:

$$\boldsymbol{g}_k^H = \left[\left(\boldsymbol{H}_k\bar{\boldsymbol{w}}_k\right)^H \boldsymbol{H}_k\bar{\boldsymbol{w}}_k\right]^{-1}\left(\boldsymbol{H}_k\bar{\boldsymbol{w}}_k\right)^H. \tag{4.54}$$

The detected signal of the k-th user is

$$\tilde{s}_{kj} = \boldsymbol{g}_k^H\boldsymbol{y}_k = \boldsymbol{g}_k^H\boldsymbol{H}_k\bar{\boldsymbol{w}}_k s_{kj} + \boldsymbol{g}_k^H\boldsymbol{n}_k = s_{kj} + \boldsymbol{g}_k^H\boldsymbol{n}_k. \tag{4.55}$$

The received signal power P_S can be expressed as follows:

$$P_S = \mathbf{E}\left[s_{kj}s_{kj}^*\right] = |s_{kj}|^2 = 1 \tag{4.56}$$

The noise power P_N may be written as

$$P_N \;=\; \mathbf{E}\left[\boldsymbol{g}_k^H\boldsymbol{n}_k\left(\boldsymbol{g}_k^H\boldsymbol{n}_k\right)^H\right] = \mathbf{E}\left[\boldsymbol{g}_k^H\boldsymbol{n}_k\boldsymbol{n}_k^H\boldsymbol{g}_k\right] \tag{4.57}$$

Since equalizer coefficients calculated according to (4.54) do not depend on noise samples, we can treat $\boldsymbol{g}_k$ and $\boldsymbol{n}_k$ as independent. Since

$$\mathbf{E}\left[\boldsymbol{n}_k\boldsymbol{n}_k^H\right] = \sigma_n^2\boldsymbol{I} \tag{4.58}$$

where σ_n^2 is a noise variance, therefore P_N takes form

$$\begin{aligned}
P_N &= \sigma_n^2\cdot\mathbf{E}\left[\left[\left(\boldsymbol{H}_k\bar{\boldsymbol{w}}_k\right)^H\boldsymbol{H}_k\bar{\boldsymbol{w}}_k\right]^{-1}\left(\boldsymbol{H}_k\bar{\boldsymbol{w}}_k\right)^H\left(\boldsymbol{H}_k\bar{\boldsymbol{w}}_k\right)\left[\left[\left(\boldsymbol{H}_k\bar{\boldsymbol{w}}_k\right)^H\boldsymbol{H}_k\bar{\boldsymbol{w}}_k\right]^H\right]^{-1}\right] \\
&= \sigma_n^2\cdot\left\|\boldsymbol{H}_k\bar{\boldsymbol{w}}_k\right\|_2^2\cdot\mathbf{E}\left[\left(\left\|\boldsymbol{H}_k\bar{\boldsymbol{w}}_k\right\|_2^2\right)^{-1}\left[\left(\left\|\boldsymbol{H}_k\bar{\boldsymbol{w}}_k\right\|_2^2\right)^H\right]^{-1}\right] \\
&= \sigma_n^2\cdot\left\|\boldsymbol{H}_k\bar{\boldsymbol{w}}_k\right\|_2^2\cdot\left\|\boldsymbol{H}_k\bar{\boldsymbol{w}}_k\right\|_2^{-4} = \frac{\sigma_n^2}{\left\|\boldsymbol{H}_k\bar{\boldsymbol{w}}_k\right\|_2^2} = \frac{\sigma_n^2}{p_k\left\|\boldsymbol{H}_k\boldsymbol{w}_k\right\|_2^2} = \frac{K\sigma_n^2\left\|\boldsymbol{w}_k\right\|_2^2}{P\left\|\boldsymbol{H}_k\boldsymbol{w}_k\right\|_2^2}
\end{aligned} \tag{4.59}$$

Then the detected SNR for the user k is

$$\gamma_{MU-MIMO} = \frac{P_S}{P_N} = \frac{P\left\|\boldsymbol{H}_k\boldsymbol{w}_k\right\|_2^2}{K\sigma_n^2\left\|\boldsymbol{w}_k\right\|_2^2} \tag{4.60}$$

4.4.2.2 MRT precoding

In the classic MU-MIMO scheme used during the broadcast phase of a two-way relaying scenario (described in Subsection 4.4.2.1), precoding vectors are designed to eliminate multiuser interference in the signals received by the BS and MS. As seen from equations (4.40) and (4.41), if the messages s_{BS} and s_{MS} are buffered by the BS and MS during the MAC phase, they will be fully available to these nodes in the subsequent phase. Since in 5G systems both reference signals (DMRS) and data pass through the same precoder and radio channel, the channel estimator can determine the total effective channels $\boldsymbol{H}_{RS,BS}\bar{\boldsymbol{w}}_{BS}$ and $\boldsymbol{H}_{RS,BS}\bar{\boldsymbol{w}}_{MS}$ in the BS, as well as $\boldsymbol{H}_{RS,MS}\bar{\boldsymbol{w}}_{MS}$ and $\boldsymbol{H}_{RS,MS}\bar{\boldsymbol{w}}_{BS}$ in the MS. These effective channels are then used first to cancel multi-user interference, followed by equalization and decoding of the desired signal. In such a case, the design of the precoding vectors can be aimed at maximizing the received SNR. The following section presents the derivation of these precoders.

Assuming that both BS and MS are aware of their own precoding vectors as well as the precoders and normalization factors of the interfering node, and under the condition of perfect channel estimation, the received signal simplifies to

$$\boldsymbol{r}_{BS} = \boldsymbol{y}_{BS} - \boldsymbol{H}_{RS,BS}\bar{\boldsymbol{w}}_{MS}s_{BS} = \boldsymbol{H}_{RS,BS}\bar{\boldsymbol{w}}_{BS}s_{MS} + \boldsymbol{n}_{BS} \tag{4.61}$$

$$\boldsymbol{r}_{MS} = \boldsymbol{y}_{MS} - \boldsymbol{H}_{RS,MS}\bar{\boldsymbol{w}}_{BS}s_{MS} = \boldsymbol{H}_{RS,MS}\bar{\boldsymbol{w}}_{MS}s_{BS} + \boldsymbol{n}_{MS} \tag{4.62}$$

In general, the received signal by the k-th station may be written as

$$\boldsymbol{r}_k = \boldsymbol{H}_k\bar{\boldsymbol{w}}_k s_{kj} + \boldsymbol{n}_k \tag{4.63}$$

where s_{kj} is the data symbol intended for the k-th receiving station, from the j-th transmitting node satisfying $|s_{kj}|^2 = 1$, $\bar{\boldsymbol{w}}_k = \sqrt{p_k}\boldsymbol{w}_k$ is the $N_T \times 1$ transmit weight vector normalized by power coefficient $p_k = \dfrac{P}{K\|\boldsymbol{w}_k\|_2^2}$, $\boldsymbol{H}_k = [h_{ij}]_k$ is the $N_R \times N_T$ channel matrix, and $\boldsymbol{n}_k$ is complex $N_R \times 1$ white Gaussian noise vector with zero mean and covariance $\sigma_n^2\boldsymbol{I}$.

At the receiver, the signals from all receive antennas are weighted by a complex weight vecor $\boldsymbol{g}_k = [g_{1k}, ..., g_{N_R k}]^T$. The linear receiver $\boldsymbol{g}_k$ can be designed by ZF or MMSE criteria. The MMSE would obtain better performance in small SNR region, but in order to simplify the analysis, the ZF receiver will be assumed:

$$\boldsymbol{g}_k^H = \left[\left(\boldsymbol{H}_k\bar{\boldsymbol{w}}_k\right)^H \boldsymbol{H}_k\bar{\boldsymbol{w}}_k\right]^{-1}\left(\boldsymbol{H}_k\bar{\boldsymbol{w}}_k\right)^H. \tag{4.64}$$

The detected signal of the k-th user is

$$\tilde{s}_{kj} = \boldsymbol{g}_k^H\boldsymbol{r}_k = \boldsymbol{g}_k^H\boldsymbol{H}_k\bar{\boldsymbol{w}}_k s_{kj} + \boldsymbol{g}_k^H\boldsymbol{n}_k = s_{kj} + \boldsymbol{g}_k^H\boldsymbol{n}_k. \tag{4.65}$$

Then following the derivations from (4.56) to (4.60) the detected SNR for the user k is

$$\gamma_k = \frac{P_S}{P_N} = \frac{p_k\|\boldsymbol{H}_k\boldsymbol{w}_k\|_2^2}{\sigma_n^2} \tag{4.66}$$

The channel matrix of user k can be decomposed by the Singular Value Decomposition (SVD) and written as

$$\boldsymbol{H}_k = \boldsymbol{U}_k \boldsymbol{\Sigma}_k \boldsymbol{V}_k^H \tag{4.67}$$

where $\boldsymbol{U}_k$ is $N_R \times N_R$ complex unitary matrix, $\boldsymbol{\Sigma}_k$ is $N_R \times N_T$ rectangular diagonal matrix with non-negative real numbers on the diagonal and $\boldsymbol{V}_k$ is an $N_T \times N_T$ complex unitary matrix. The diagonal entries of $\boldsymbol{\Sigma}_k$ are known as the singular values of $\boldsymbol{H}_k$. The columns of $\boldsymbol{U}_k$ and $\boldsymbol{V}_k$ are called the left singular vectors and the right singular vectors of $\boldsymbol{H}_k$, respectively.

To minimize the block error rate, γ_k must be maximized with respect to $\boldsymbol{w}_k$. The optimization problem is the following.

$$\gamma_k^{max} = \max_{\boldsymbol{w}_k} \quad \frac{p_k \left\| \boldsymbol{H}_k \boldsymbol{w}_k \right\|_2^2}{\sigma_n^2} \tag{4.68}$$

The key term in the objective function (4.68) is $\left\| \boldsymbol{H}_k \boldsymbol{w}_k \right\|_2^2$ which is the squared norm of the projection of the precoder $\boldsymbol{w}_k$ onto the channel matrix $\boldsymbol{H}_k$. After performing several derivations of equation (4.66) we obtain

$$\gamma_k = \frac{p_k (\boldsymbol{H}_k \boldsymbol{w}_k)^H (\boldsymbol{H}_k \boldsymbol{w}_k)}{\sigma_n^2} = \frac{p_k \boldsymbol{w}_k^H \boldsymbol{H}_k^H \boldsymbol{H}_k \boldsymbol{w}_k}{\sigma_n^2} = \frac{p_k \boldsymbol{w}_k^H \boldsymbol{A} \boldsymbol{w}_k}{\sigma_n^2} \tag{4.69}$$

where matrix $\boldsymbol{A} = \boldsymbol{H}_k^H \boldsymbol{H}_k$. From (4.69) it can be observed that the optimization problem can be reformulated as an eigenvalue problem. The term $\boldsymbol{w}_k^H \boldsymbol{A} \boldsymbol{w}_k$ is maximized when $\boldsymbol{w}_k$ is aligned with the eigenvector associated with the largest eigenvalue of matrix $\boldsymbol{A}$. This eigenvector corresponds to the first column of the right singular matrix $\boldsymbol{V}_k$ ($[\boldsymbol{V}_k]_1$). If $\boldsymbol{w}_k = [\boldsymbol{V}_k]_1$ then

$$\begin{aligned} \gamma_k &= \frac{p_k \left[\boldsymbol{V}_k\right]_1^H \boldsymbol{A} \left[\boldsymbol{V}_k\right]_1}{\sigma_n^2} = \frac{p_k \left[\boldsymbol{V}_k\right]_1^H \lambda_k^{max} \left[\boldsymbol{V}_k\right]_1}{\sigma_n^2} = \frac{p_k \lambda_k^{max} \left\| \left[\boldsymbol{V}_k\right]_1 \right\|_2^2}{\sigma_n^2} \\ &= \frac{p_k \lambda_k^{max}}{\sigma_n^2} = \frac{\lambda_k^{max}}{2\sigma_n^2} = \frac{(\delta_k^{max})^2}{2\sigma_n^2} \end{aligned} \tag{4.70}$$

where λ_k^{max} is a maximal eigenvalue of $\boldsymbol{H}_k^H \boldsymbol{H}_k$, δ_k^{max} is a maximal singular value of $\boldsymbol{H}_k$, the total transmitted power $P = 1$, number of receiving nodes $K = 2$ and $\left\| \left[\boldsymbol{V}_k\right]_1 \right\|_2^2 = 1$ since right singular vectors have a unit norm.

When transmission utilizes CSI-RS, where only user data passes through the precoder and the reference signal is applied after the precoding stage, a simplified codebook-based approach, named Codebook-based Maximum Ratio Transmission (CB-MRT), can be employed. In CB-MRT, the relay station selects the precoding vectors from a finite codebook standardized by 3GPP for the LTE and NR systems [8], which is known throughout all stations. As a result, only the indices of the selected precoders (PMI) are transmitted from the relay station to the BS and MS, which need to know the precoder applied to the other station to cancel interference. The CB-MRT

precoding vectors are chosen according to the Mean Squared Error (MSE) criterion presented in [43]. The $\boldsymbol{w}_{BS}$ and $\boldsymbol{w}_{MS}$ take the following form.

$$\boldsymbol{w}_{BS} = [\boldsymbol{F}_{PMI_{BS}}]_1 \tag{4.71}$$

$$\boldsymbol{w}_{MS} = [\boldsymbol{F}_{PMI_{MS}}]_1 \tag{4.72}$$

where PMI_{BS} and PMI_{MS} ($PMI_{BS} = 1, ..., C$, $PMI_{MS} = 1, ..., C$) are the precoding matrix indices selected by the RS for the BS and MS data, respectively. Given that $\mathcal{F} = \boldsymbol{F}_1, ..., \boldsymbol{F}_C$ is the finite codebook of precoding matrices, the PMI index specifies the row, while the subscript in $[.]_1$ and $[.]_1$ denotes the column in the codebook where the chosen precoder is located (the column number corresponds to the number of layers used in transmission).

4.5 Simulation results

Simulation results presented in this section were obtained using the link level LTE/NR simulator developed by the author. The developed link-level simulation package consists of several parts. The core part of the simulator that models the LTE and NR physical layers has been written in the C++ programming language in an object-oriented manner. This main part utilizes IT++ library, which is a C++ library of mathematical, signal processing procedures like Fast Fourier Transform (FFT) calculation or SVD of matrices. The parameters of the simulation tool are set in the configuration files, command-line arguments or both. Scripts written in Matlab have been used for post-processing and visualizing the simulation results.

The software implementation of a single communication link is performed by modeling the whole transport layer and the physical layer processing chain from the transmitter to the receiver, as presented in Fig. 2.7. It should be mentioned that only the transmitter part is standardized in 3GPP documents. The receiver processing chain was developed by the author. DL-SCH transport channel processing is a combination of error detection, error correction, rate matching, interleaving, and transport channel mapping onto the PDSCH physical channel. Forward error correction (FEC) is provided by LDPC codes, and error detection is based on cyclic redundancy check (CRC) codes. The rate matching performs interleaving, as well as repetition or puncturing, to match the size of a block generated at the output of the transport channel to the number of bits allocated for the transmission of the physical channel. The number of bits carried by the PDSCH physical channel is determined by the modulation scheme, the number of resource blocks allocated for transmission, and the transmission mode. PDSCH processing consists of scrambling, modulation, layer mapping, precoding, mapping onto the resource grid, and conversion to complex-valued OFDM

baseband signals for each antenna port. Both layer mapping and precoding are associated with multi-antenna transmission and reception. The split between these two steps allows all antenna processing schemes to be taken into account in a single framework. On the receiver side, complementary operations are performed after channel estimation and data equalization.

4.5.1 Simulation procedure and parameters

The performance of the multi-antenna two-way relaying scheme has been evaluated through the aforementioned C++ link-level simulations with key simulation parameters outlined in Table 5.1. The channel between the end nodes and the relay node was simulated using a Extended Pedestrian A model (EPA) A fading channel model [44] designed to represent environments with low delay spread. The main parameters of this model are specified in Table 4.2. The EPA channel consists of seven independent paths, each of them with a Rayleigh-Jakes-Doppler spectrum. The maximum Doppler frequency was set to 5 Hz. The channel coefficients between each antenna are assumed to be uncorrelated. The multipath effects are neutralized at the receivers by the CP present in OFDM transmission.

Table 4.1: Simulation parameters.

Parameter	**Value**
Radio Channel	EPA 5Hz
Channel Estimation	Ideal
Channel Coding	LDPC NR, rate 1/3
Modulation	QPSK
Multiplexing	OFDM
Subcarrier Spacing	60 kHz
Slot length	0.25 ms
OFDM symbol length	16.67 us
CP length	1.2 us
Subframes in a frame	10
Slots in a subframe	4
OFDM symbols in a slot	14
Subcarriers in a PRB	12
PRB width	0.72 MHz
Number of PRBs	10

As shown in Table 4.1, the OFDM parameters chosen for the simulations are consistent with 5G NR. The primary outcome of the simulations is the achievable block error rate (BLER) achieved for the MAC and BR phases, for the links between end nodes and the RS. Each subframe, configured according to the transmission parameters, was treated as a data block. It is assumed that, as in many systems, the final performance is achieved after the application of HARQ or ARQ techniques within the

Table 4.2: EPA delay profile.

Excess tap delay [ns]	Relative power [dB]
0	0.0
30	-1.0
70	-2.0
90	-3.0
110	-8.0
190	-17.2
410	-20.8

radio link control sublayer. Therefore, a BLER in the range of 10^{-2} to 10^{-3} prior to ARQ usage is sufficient for satisfactory system performance.

To ensure precise BLER measurements as a function of SNR, each SNR point was simulated on at least 500 different channel realizations. For each channel realization, data from 20 transmitted slots were collected. If the minimum threshold of 100 erroneous blocks was not reached after simulating 10,000 slots, the simulation continued until either 100 errors were recorded or the maximum limit of 1,000,000 slots was simulated.

4.5.2 Results

In this section, the performance of the multiple antenna NC scheme together with the proposed MU-MIMO transmission protocol will be evaluated. All the presented plots will refer to the link between the base station and the relay station. Since the results for the link between the mobile station and the relay station are analogous and lead to the same conclusions, they have been moved to Section 4.7 to improve the clarity of the chapter.

4.5.2.1 Multiple Access Phase

For the multiple access phase, five antenna configurations were considered, that is, 1×2, 1×4, 2×2, 2×4, and 4×4, where the first number indicates the number of transmit antennas in both BS and MS, while the second number indicates the number of receive antennas in RS. The BLER performance as a function of transmit SNR for the $BS \rightarrow RS$ link is shown in Fig. 4.5, respectively. The corresponding achievable throughput is presented in Fig. 4.6.

The best results were observed for 4×4 configuration, followed by 2×4, 1×4, 2×2 and 1×2, in this order. It is evident that increasing the number of receive antennas has a greater impact on improving the output SNR than increasing the number of transmit antennas. For example, the 1×4 set-up outperforms the 2×2 configuration, despite both schemes achieving the same diversity. This comes from the fact that

the energy radiated from each transmit antenna in the 2×2 scenario is half of that radiated from the single antenna, resulting in a lower received SNR compared to the 1×4 set-up.

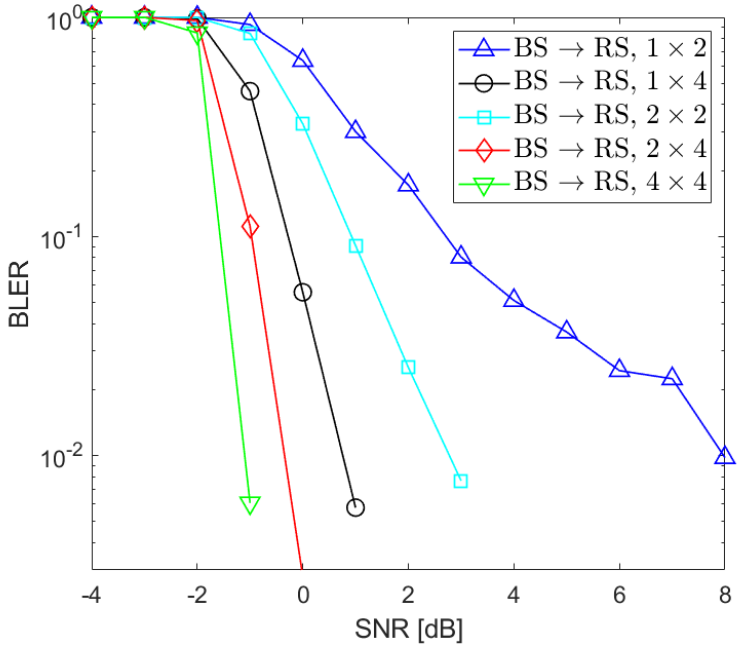

Figure 4.5: BLER performance of the link between BS and RS during the MAC phase

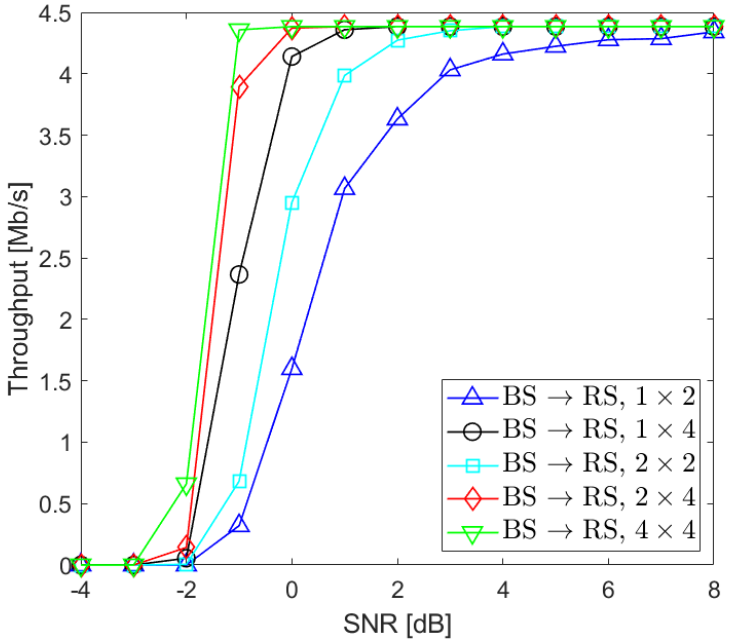

Figure 4.6: Throughput performance of the link between BS and RS during the MAC phase

The maximum achievable throughput, assuming a $BLER = 0$, is just under 4.5 Mb/s. This occurs in the 4×4 scenario with an SNR of -1 dB, in the 2×4 setup at 0 dB, for 1×4 at 1 dB, for 2×2 at 3 dB and for 1×2 at 8 dB.

4.5.2.2 Broadcast Phase

The performance analysis of the broadcast phase is presented in Figs. 4.7-4.22. Fig. 4.7 and Fig. 4.8 show the BLER and throughput performance of network coding applied in the broadcast phase in various antenna setups. The same as in MAC phase five antenna configurations were simulated: 2×1, 4×1, 2×2, 4×2, and 4×4, where the first number indicates the number of transmit antennas in RS, while the second number indicates the number of receive antennas in BS and MS. As expected, increasing the number of transmit and receive antennas reduces the block error probability, with the 4×4 configuration achieving the best performance. The BLER performance of the other configurations follows this order: 4×2, 2×2, 4×1 and 2×1, where the latter performs the worst. It is worth noting that in the BR phase, 2×2 outperforms 4×1 since in 2×2 the number of received antennas is higher than in 4×1.

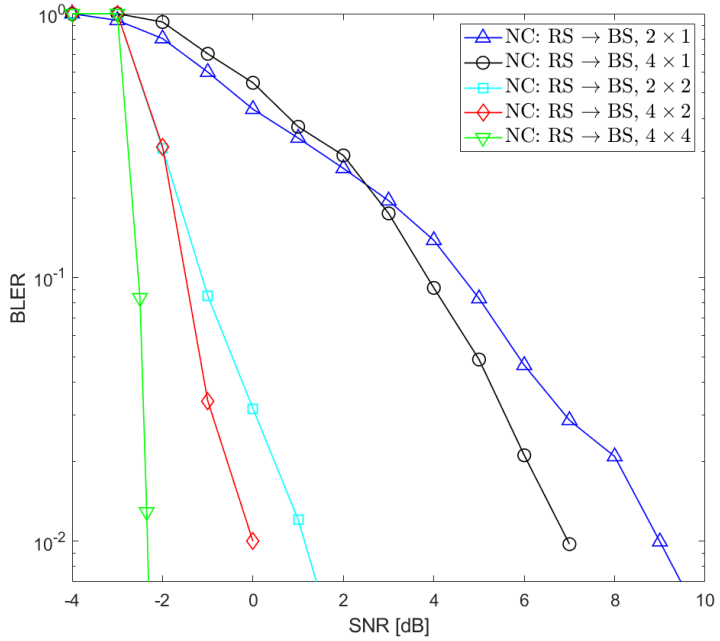

Figure 4.7: Network coding in BR phase, BLER performance of the link between RS and BS

The maximum achievable throughput was achieved in the 4×4 configuration for an SNR of -1 dB, in the 4×2 setup at 0 dB, in the 2×2 scenario at 2 dB, for 4×1 at 8 dB and for 1×2 at 10 dB.

Figs. 4.9-4.18 show the BLER and throughput performance of the classic MU-MIMO alongside the proposed MRT and CB-MRT precoding for MU-MIMO during

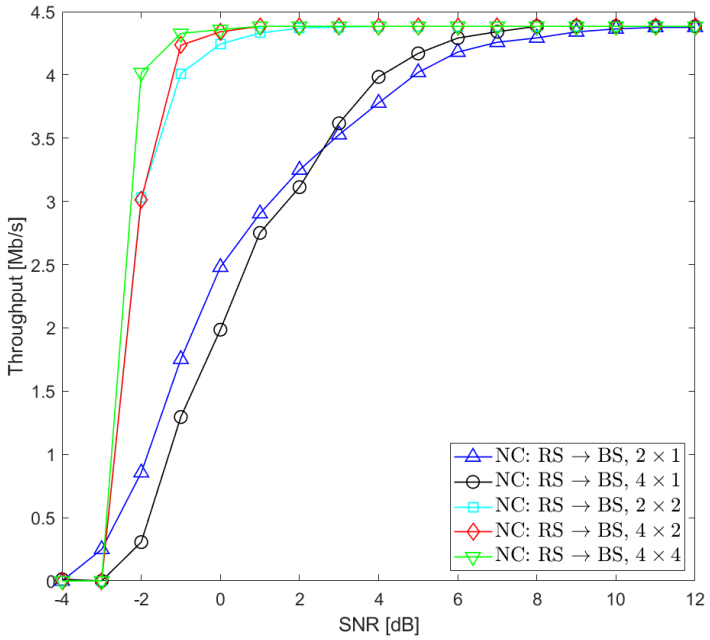

Figure 4.8: Network coding in BR phase, throughput performance of the link between RS and BS

the broadcast phase. Each pair of BLER and througput plots for the $RS \rightarrow BS$ link present results obtained for different antenna setups. Specifically, Fig. 4.9 and Fig. 4.10 correspond to the 2×1 antenna setup, Fig. 4.11 and Fig. 4.12 depict the 4×1 scenario, Fig. 4.13 and Fig. 4.14 show the 2×2 antenna configuration, Fig. 4.15 and Fig. 4.16 correspond to the 4×2 setup, and Fig. 4.17 and Fig. 4.18 illustrate the 4×4 scenario. Each plot compares the performance of five precoding algorithms: MRT, CB-MRT, ZFBF, BDBF, and MU-BDBF. Detailed descriptions of these precoders can be found in Section 4.4.2. In the 2×1 scenario, where the RS has two transmit antennas and both BS and MS each have a single receive antenna, the MRT performs the best and the performance gap between the proposed MRT and CB-MRT precoders and the traditional MU-MIMO precoders such as ZFBF, BDBF and MU-BDBF is substantial, reaching up to 6 dB. In that scenario, the ZFBF, BDBF and MU-BDBF algorithms exhibit similar performance. For the 4×1 scenario, CB-MRT, ZFBF and MU-BDBF provide comparable BLER results, while BDBF performs significantly worse, requiring approximately 12 dB more SNR to achieve a BLER of 10^{-2}. MRT outperforms the other precoders by about 1 dB in this case. In the 2×2 and 4×4 scenarios, only MRT, CB-MRT, and ZFBF are considered, as BDBF and MU-BDBF are not applicable due to the inappropriate dimensions of the channel matrix. For the 2×2 setup, MRT and CB-MRT show similar performance, while ZFBF lags by approximately 6 dB at a BLER of 10^{-2}. In the 4×4 scenario, MRT demonstrates superior performance compared to CB-MRT and ZFBF, which provide comparable results. In the 4×2 scenario, the order of BLER performance for the tested precoders is as follows: MRT,

CB-MRT/ZFBF, MU-BDBF and BDBF, with BDBF performing the worst. In general, the analysis reveals that MRT consistently outperforms all other precoders in various antenna configurations, while BDBF is the least effective.

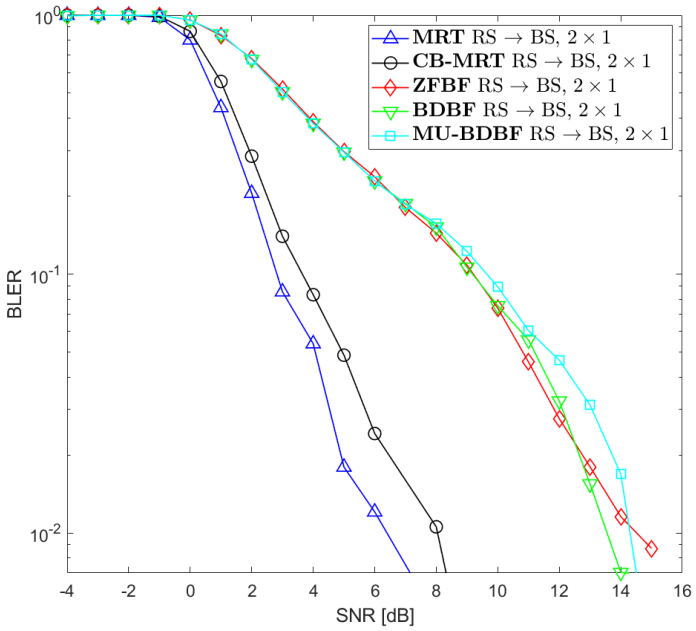

Figure 4.9: MU-MIMO 2×1 in BR phase, BLER performance of the link between RS and BS

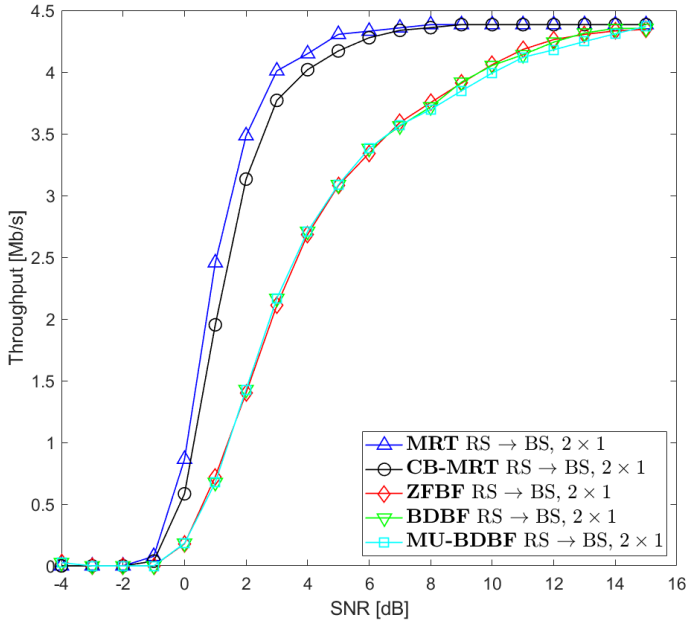

Figure 4.10: MU-MIMO 2×1 in BR phase, throughput performance of the link between RS and BS

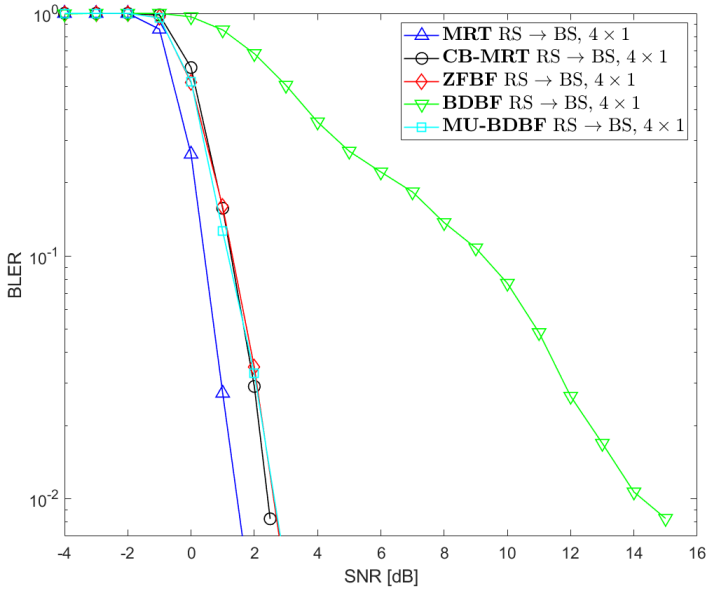

Figure 4.11: MU-MIMO 4×1 in BR phase, BLER performance of the link between RS and BS

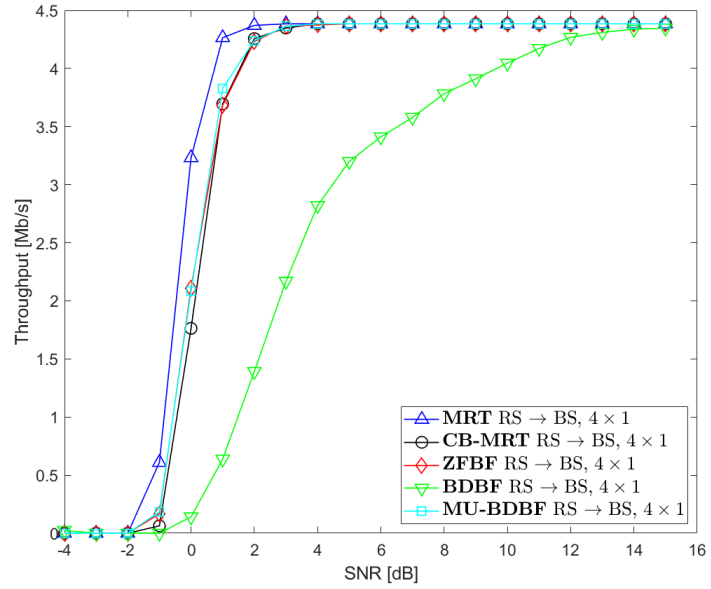

Figure 4.12: MU-MIMO 4×1 in BR phase, throughput performance of the link between RS and BS

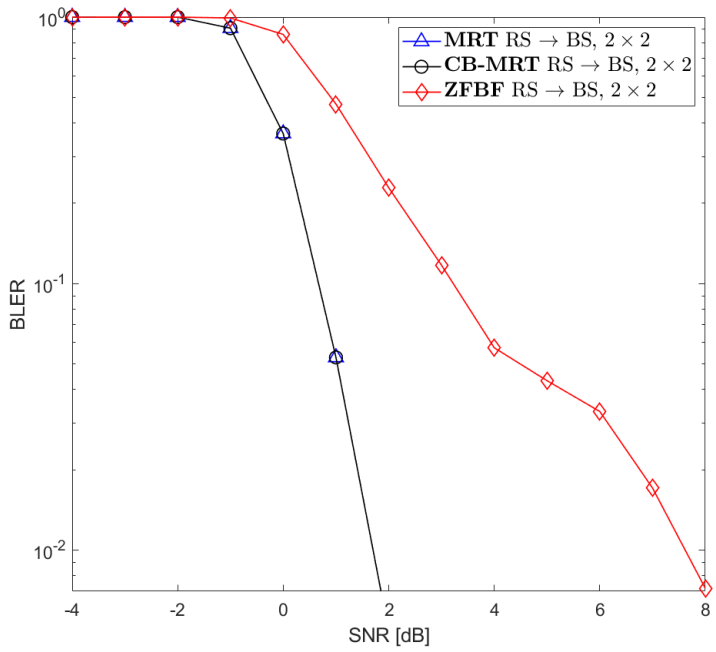

Figure 4.13: MU-MIMO 2×2 in BR phase, BLER performance of the link between RS and BS

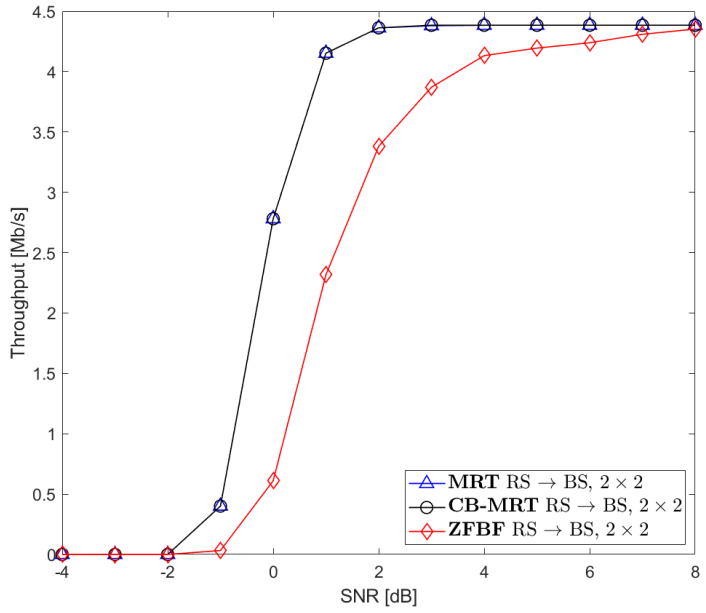

Figure 4.14: MU-MIMO 2×2 in BR phase, throughput performance of the link between RS and BS

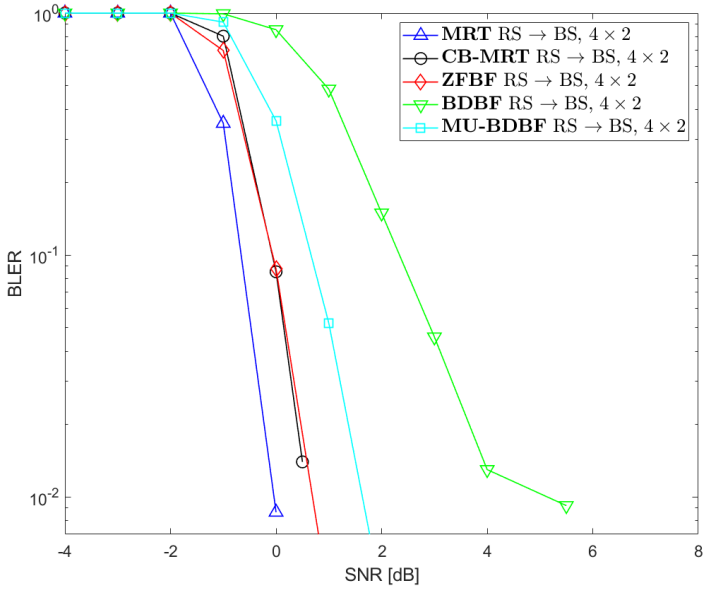

Figure 4.15: MU-MIMO 4×2 in BR phase, BLER performance of the link between RS and BS

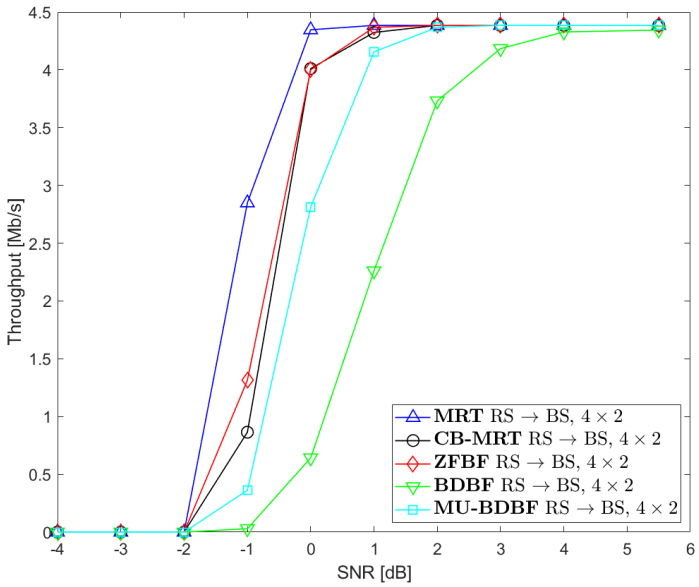

Figure 4.16: MU-MIMO 4×2 in BR phase, throughput performance of the link between RS and BS

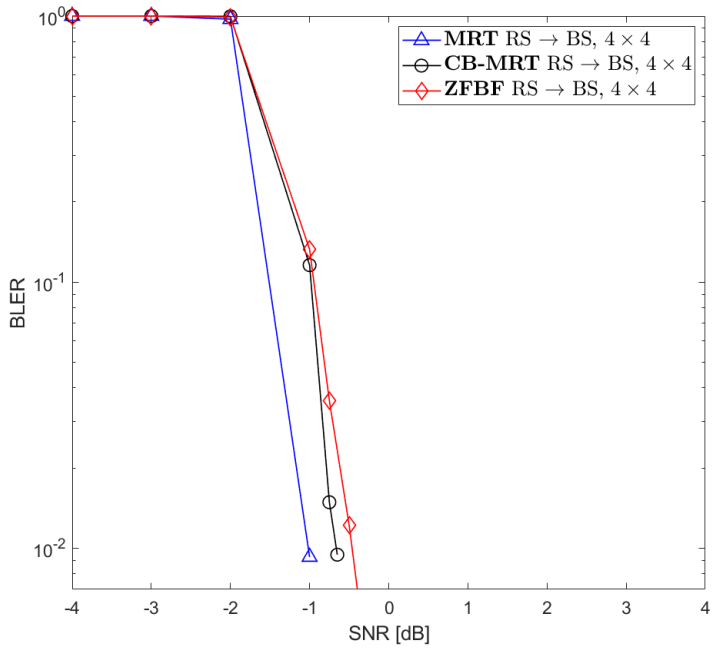

Figure 4.17: MU-MIMO 4×4 in BR phase, BLER performance of the link between RS and BS

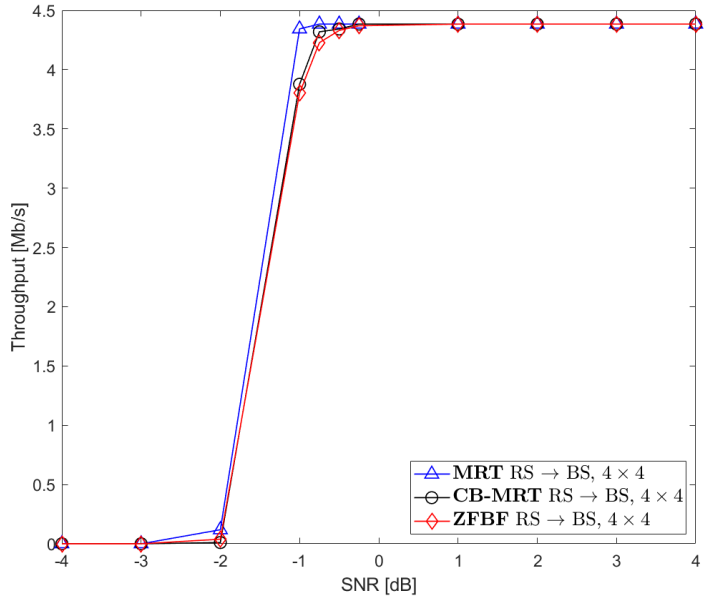

Figure 4.18: MU-MIMO 4×4 in BR phase, throughput performance of the link between RS and BS

Fig. 4.19 and Fig. 4.20 illustrate the performance comparison of the MRT precoder in different antenna configurations. The highest performance is observed in the 4×4 setup, where a BLER of 10^{-2} is achieved at an SNR of approximately -1 dB. The 4×2 configuration follows, with performance lower by about 1 dB, then the 4×1 configuration, and next the 2×2 configuration. The lowest performance is observed in the 2×1 scenario. Maximum throughput is achieved at -1 dB for 4×4, 0 dB for 4×2, 2 dB for both 2×2 and 4×1, and 8 dB for 2×1.

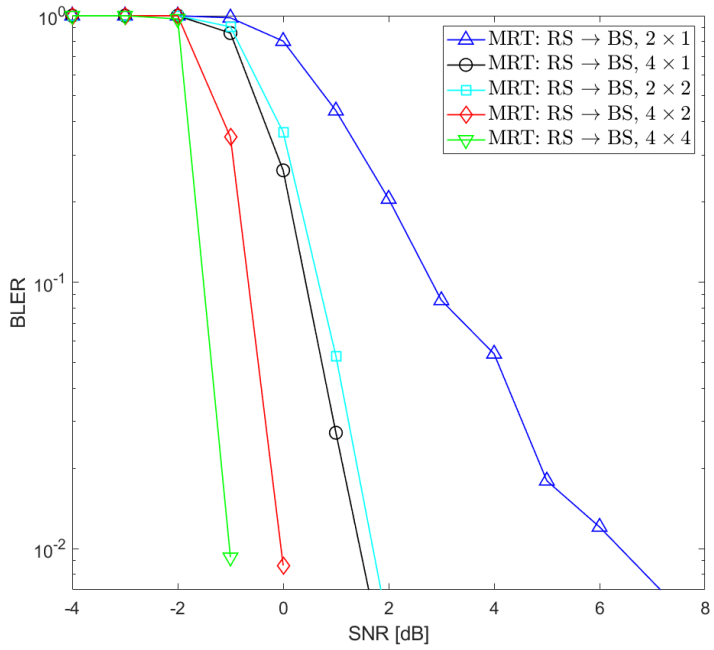

Figure 4.19: MRT in BR phase, BLER performance of the link between RS and BS

The comparison between the network coding and MRT precoding algorithms is illustrated in Fig. 4.21 and Fig. 4.22. In the 4×4 antenna scenario, the network coding outperforms MU-MIMO with MRT precoding by approximately 1 dB. Similarly, for the 4×2 configuration, the BLER curve for network coding is better than MRT by about 1 dB, although both achieve a BLER level of 10^{-2} at the same SNR of 0 dB. A similar trend is observed in the 2×2 scenario, where the network coding initially shows better performance, but both curves converge around a BLER of 10^{-2} at an SNR of approximately 2 dB. However, for configurations with one receiving antenna, such as 4×1 and 2×1, MRT significantly outperforms network coding. In the 4×1 case, the gap between the MRT and network coding BLER curves is around 5 dB, and for the 2×1 configuration, network coding lags by about 2 dB. The maximum throughput is achieved at an SNR of -1 dB for both NC and MRT in the 4×4 scenario, at 1 dB in the 4×2 configuration for both, at 2 dB in the 2×2 setup for both algorithms, at 2 dB in the 4×1 configuration for MRT (compared to 8 dB for network coding), and at 8 dB in the 2×1 scenario for MRT (compared to 10 dB for network coding).

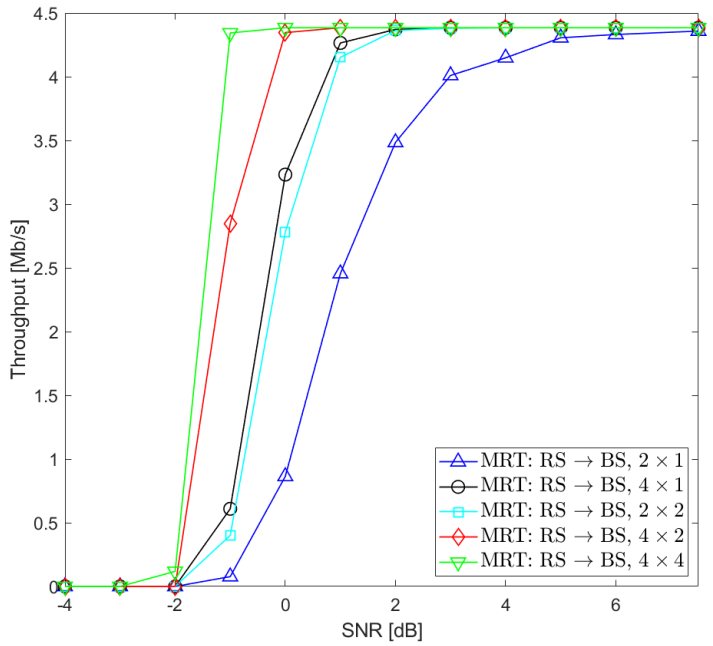

Figure 4.20: MRT in BR phase, throughput performance of the link between RS and BS

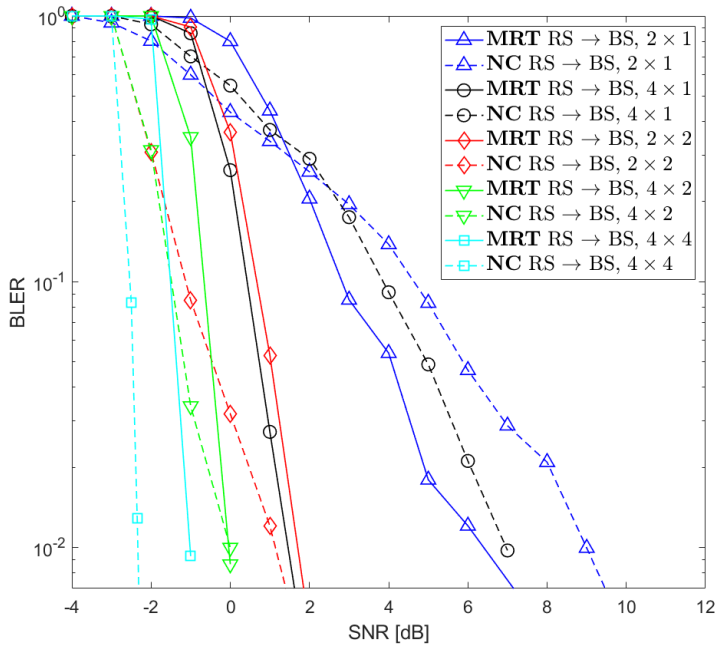

Figure 4.21: Comparison of network coding and MRT precoding in BR phase, BLER performance of the link between RS and BS

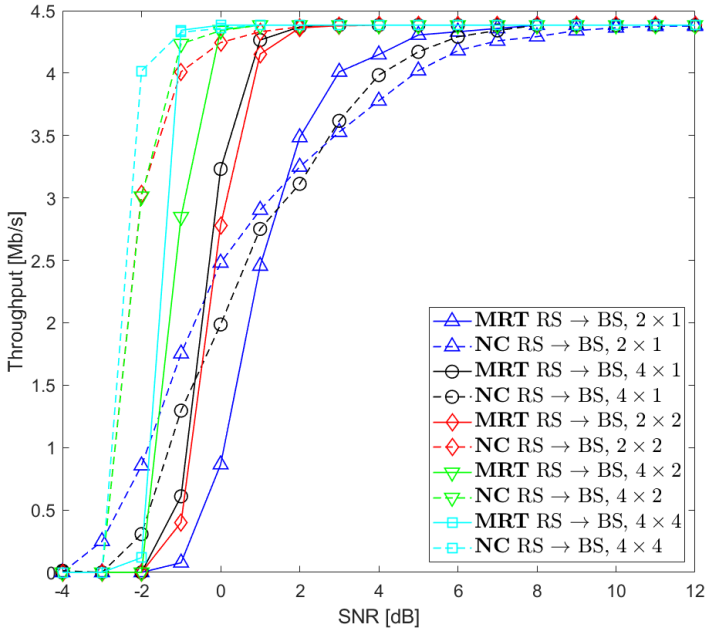

Figure 4.22: Comparison of network coding and MRT precoding in BR phase, throughput performance of the link between RS and BS

4.6 Conclusions

This chapter explored how multiple antennas can be utilized in the broadcast phase of a two-way relaying scenario. Novel MU-MIMO precoding techniques (MRT and CB-MRT) were introduced that maximize the received SNR at the receiving station compared to well known MU-MIMO precoders such as ZFBF, BDBF or MU-BDBF. The analysis of the output SNR (equation (4.60) versus (4.70)) has proved the superiority of the proposed MRT scheme, which includes the design of both the precoder and interference cancellation receiver. Simulation results further confirm the MRT precoder's advantage over traditional approaches.

In single-user transmission schemes, beamforming significantly improves communication performance by directing signal power more efficiently towards the receiver, resulting in a notable increase in SNR. Compared to transmit diversity, beamforming offers better received SNR, as transmit diversity focuses on enhancing reliability rather than data rates. The analysis of the theoretical received SNR of both beamforming and transmit diversity, which is $\gamma_{SU-MIMO} = \frac{(\delta_k^{max})^2}{\sigma_n^2}$ and $\gamma_{TX-DIV} = \frac{\sum_{i=1}^{r} \delta_i^2}{N_T \sigma_n^2}$, respectively, proves this statemant, since $\gamma_{SU-MIMO} > \gamma_{TX-DIV}$ is satisfied. The proposed MRT MU-MIMO is similar to the SVD-based precoding used in SU-MIMO systems. However, in MU-MIMO, the received SNR is reduced by a factor of K (the number of receiving nodes), because the transmitted power per user is less than in SU-MIMO,

where the entire power is allocated to a single data stream. Consequently, the performance comparison between MU-MIMO with MRT precoding (equation (4.70)) and network coding with transmit diversity (equation (4.35)), based on theoretical received SNR, is ambiguous and is influenced by factors such as the rank of the channel matrix, which varies with the number of transmit and receive antennas.

Simulations showed that across all verified antenna configurations, MU-MIMO with the MRT precoder delivers equal or better BLER performance at levels of 10^{-2} compared to the network coding approach. MU-MIMO demonstrated the greatest advantage over network coding in single receive antenna configurations, where the channel rank is the lowest, thus degrading the network coding received SNR. In other scenarios, network coding exhibited greater robustness at lower SNR values.

A major advantage of network coding over MU-MIMO is its lower complexity and lack of channel state information requirements at the receiver. However, in practical systems with imperfect channel estimation, MU-MIMO performance may decline, although further investigation is needed to fully evaluate the influence of imperfect channel state information. On the other hand, a significant limitation of network coding is that, since data blocks are mixed at the bit level, both messages must be of the same length, restricting the flexibility of modulation and coding schemes, as well as the ability to send different packet sizes when stations transmit varying amounts of data. MU-MIMO, in contrast, can be seen as network coding applied at the signal sample level rather than binary blocks. This provides flexibility in selecting different block sizes and modulation and coding schemes for BS and MS during the multiple access phase, better accommodating varying channel conditions and transmission requirements.

4.7 Appendix. Additional simulation results

The following section comprises the simulation results for the link between the mobile station and the relay. The results for the multiple access phase for the $MS \rightarrow RS$ link are presented in Fig. 4.23 where the BLER performance is verified and in Fig. 4.24 with the throughput results. Similarly to $BS \rightarrow RS$, the 4×4 scenario achieved the best results.

The performance analysis of the network coding in the broadcast phase is presented in Fig. 4.25 and Fig. 4.26 with respect to its BLER and throughput. Among five simulated antenna configurations such as 2×1, 4×1, 2×2, 4×2, and 4×4, it can be seen once again that increasing the number of transmit and receive antennas improves the system performance in terms of BLER and achievable throughput.

The comparison of the classic MU-MIMO scheme for the broadcast phase with precoding algorithms such as ZFBF, BDBF and MU-BDBF versus the two proposed precoding algorithms - MRT and CB-MRT is presented in Figs. 4.27-4.36. Each pair of

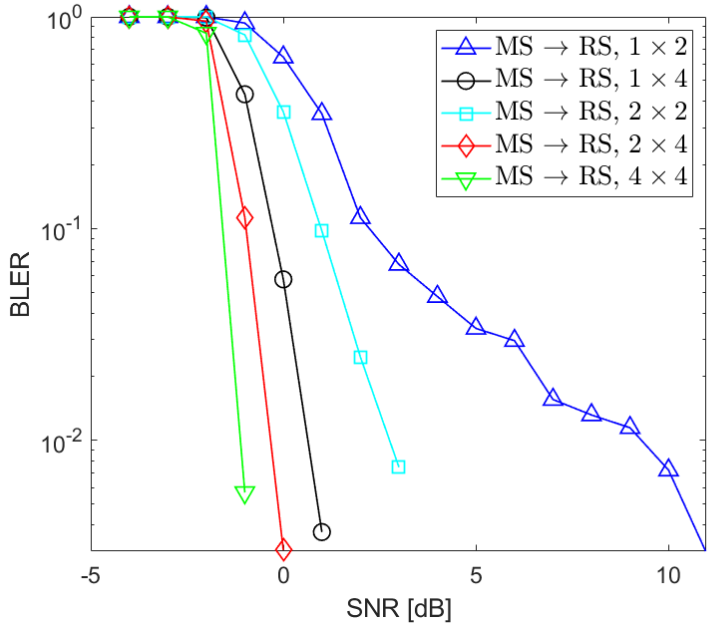

Figure 4.23: BLER performance of the link between MS and RS during the MAC phase

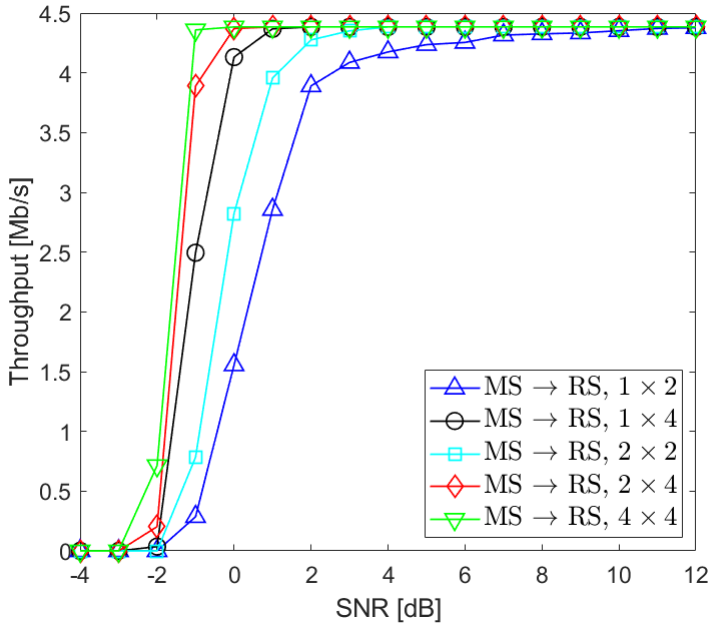

Figure 4.24: Throughput performance of the link between MS and RS during the MAC phase

BLER and througput plots for the $RS \rightarrow MS$ link shows results for different antenna configurations. Fig. 4.27 and Fig. 4.28 correspond to the 2×1 antenna setup, Fig. 4.29 and Fig. 4.30 depict the 4×1 scenario, Fig. 4.31 and Fig. 4.32 show the 2×2 antenna configuration, Fig. 4.33 and Fig. 4.34 correspond to the 4×2 setup, and Fig. 4.35 and Fig. 4.36 illustrate the 4×4 scenario. The conclusions drawn from the graphs presented for the $RS \rightarrow MS$ link are analogous to those presented in the previous section for

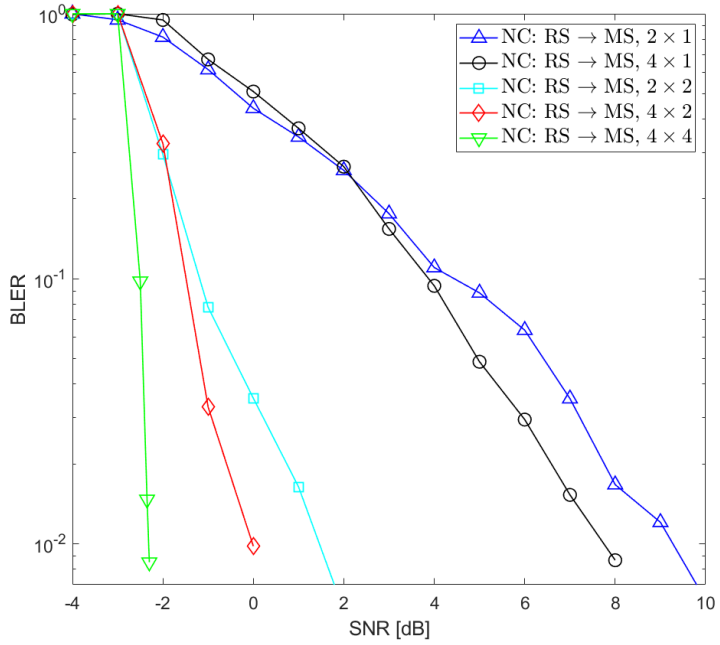

Figure 4.25: Network coding in BR phase, BLER performance of the link between RS and MS

the $RS \rightarrow BS$ link. The best results, regardless of the antenna configuration, were obtained for the proposed algorithm called MRT.

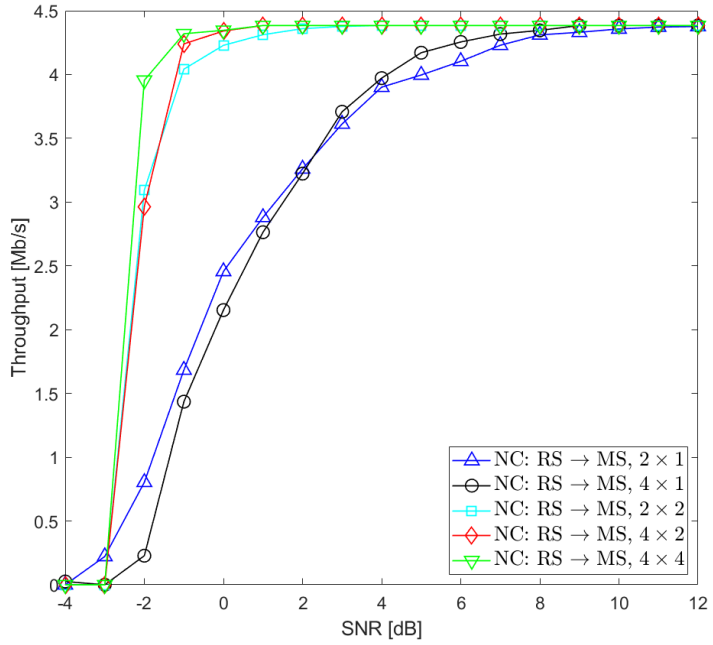

Figure 4.26: Network coding in BR phase, throughput performance of the link between RS and MS

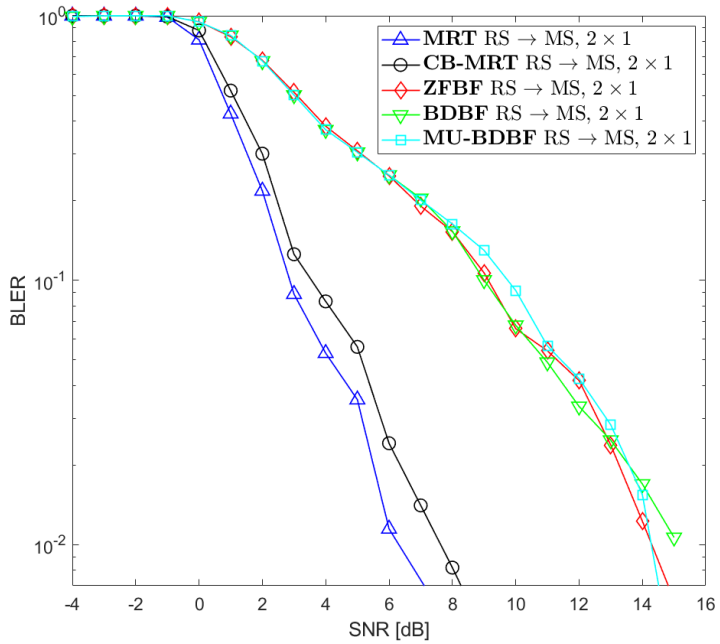

Figure 4.27: MU-MIMO 2×1 in BR phase, BLER performance of the link between RS and MS

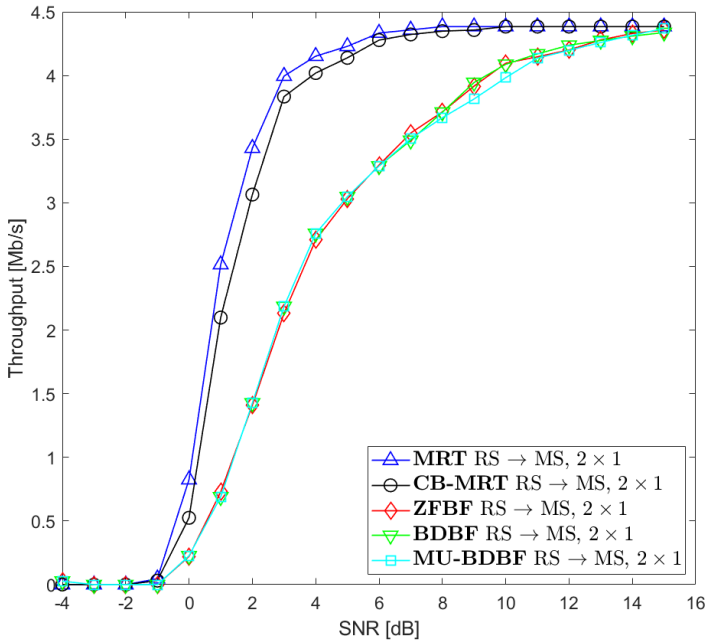

Figure 4.28: MU-MIMO 2×1 in BR phase, throughput performance of the link between RS and MS

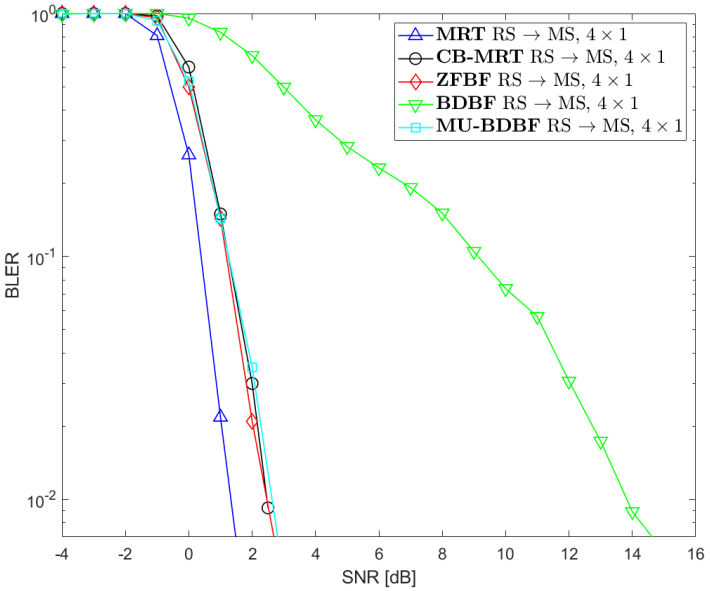

Figure 4.29: MU-MIMO 4 × 1 in BR phase, BLER performance of the link between RS and MS

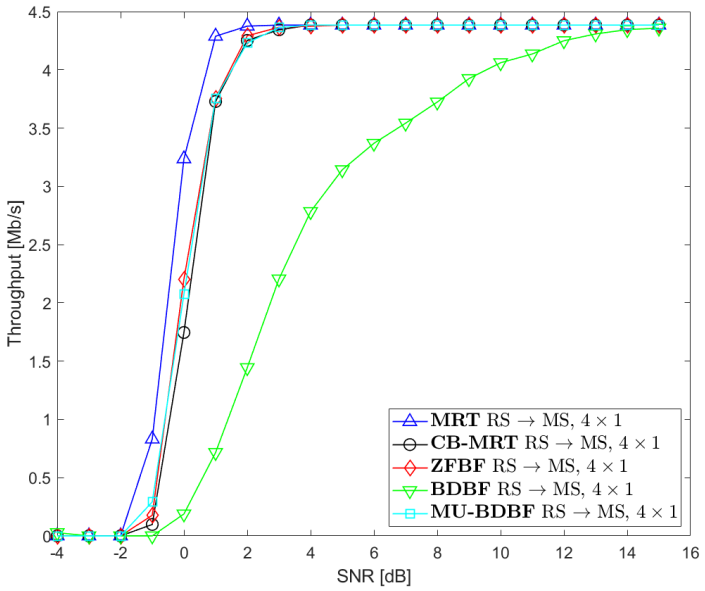

Figure 4.30: MU-MIMO 4×1 in BR phase, throughput performance of the link between RS and MS

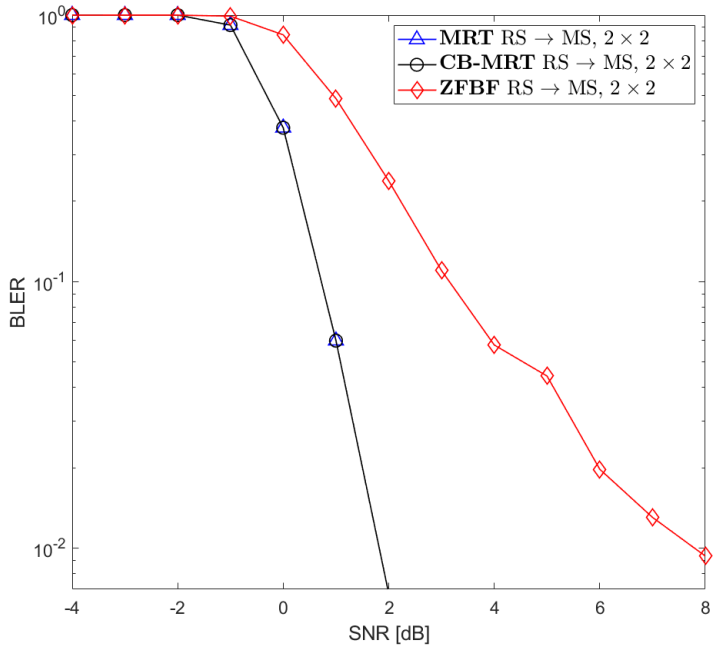

Figure 4.31: MU-MIMO 2×2 in BR phase, BLER performance of the link between RS and MS

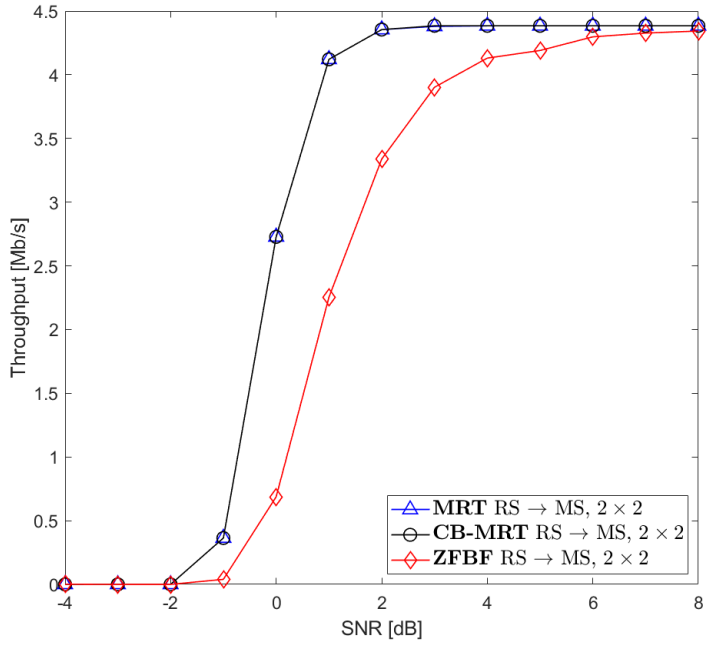

Figure 4.32: MU-MIMO 2×2 in BR phase, throughput performance of the link between RS and MS

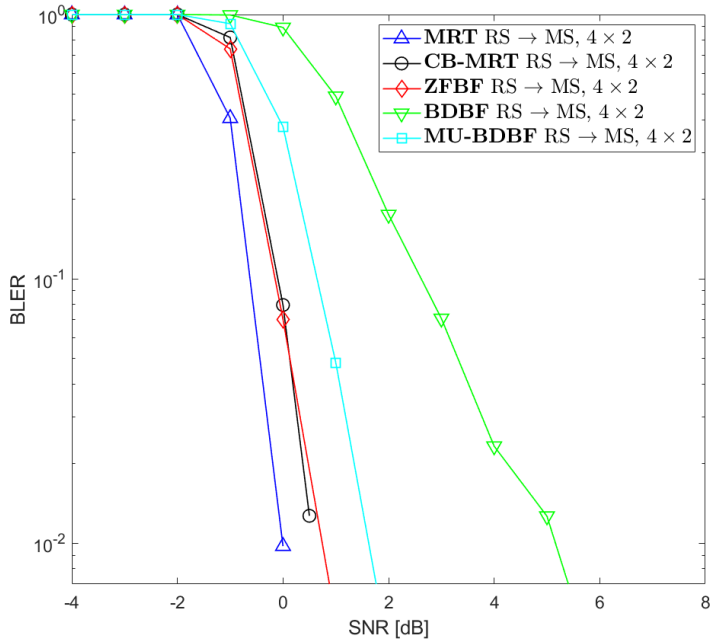

Figure 4.33: MU-MIMO 4 × 2 in BR phase, BLER performance of the link between RS and MS

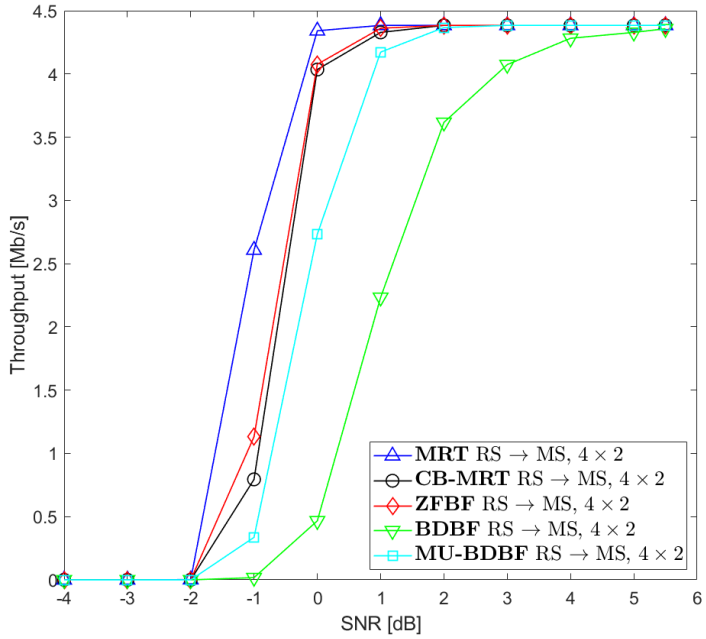

Figure 4.34: MU-MIMO 4×2 in BR phase, throughput performance of the link between RS and MS

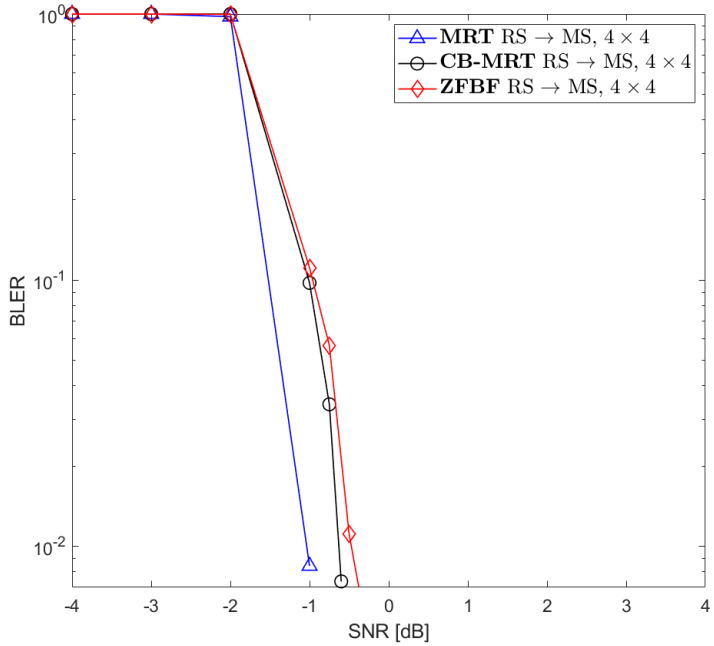

Figure 4.35: MU-MIMO 4 × 4 in BR phase, BLER performance of the link between RS and MS

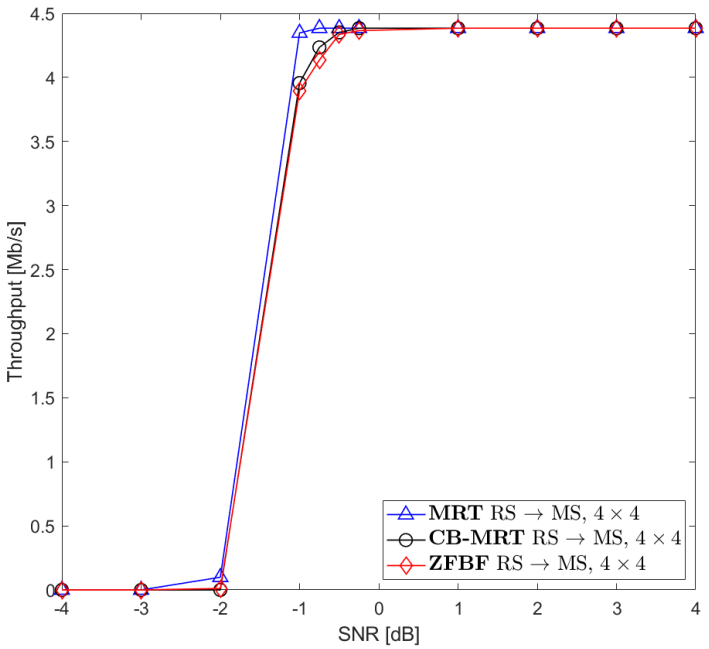

Figure 4.36: MU-MIMO 4×4 in BR phase, throughput performance of the link between RS and MS

A detailed comparison of the results achieved by the MRT precoding algorithm for different antenna configurations is presented in Fig. 4.37 and Fig. 4.38. As expected, the best results were obtained for the configuration with the highest number of antennas tested, 4×4, and the worst for the 2×1 configuration.

The last Fig. 4.39 and Fig. 4.40 present a comparison of the results obtained for the network coding scheme and MU-MIMO with the MRT algorithm. The MU-MIMO technique with the MRT precoder achieves significantly better results when the MS is equipped with only one receiving antenna. In other cases, the results are similar, with a slight advantage for the NC algorithm (around 1 dB).

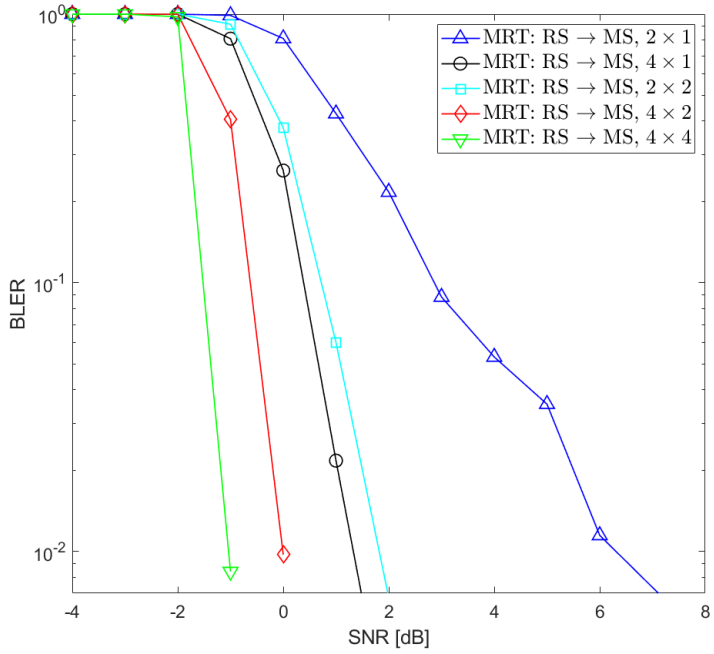

Figure 4.37: MRT in BR phase, BLER performance of the link between RS and MS

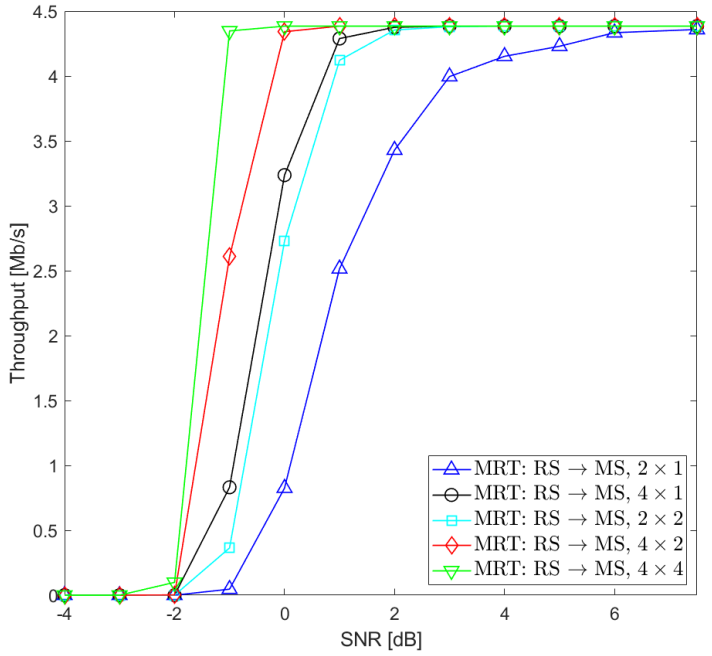

Figure 4.38: MRT in BR phase, throughput performance of the link between RS and MS

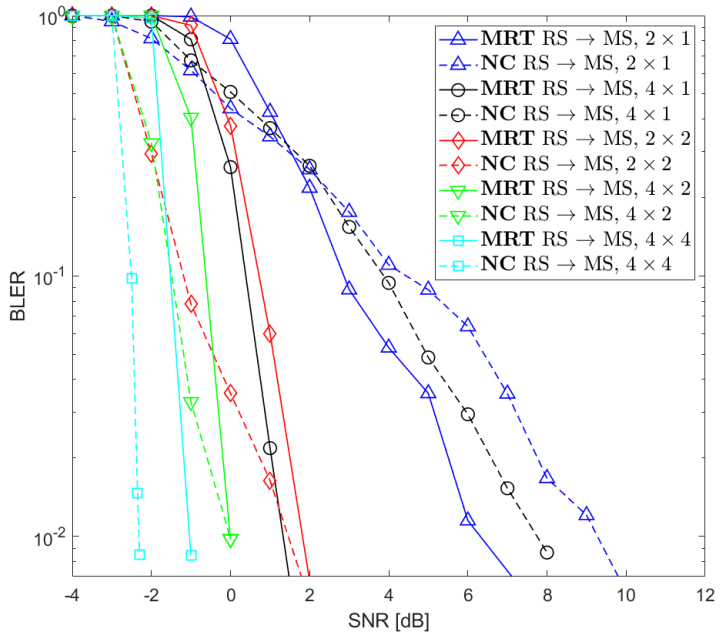

Figure 4.39: Comparison of network coding and MRT precoding in BR phase, BLER performance of the link between RS and MS

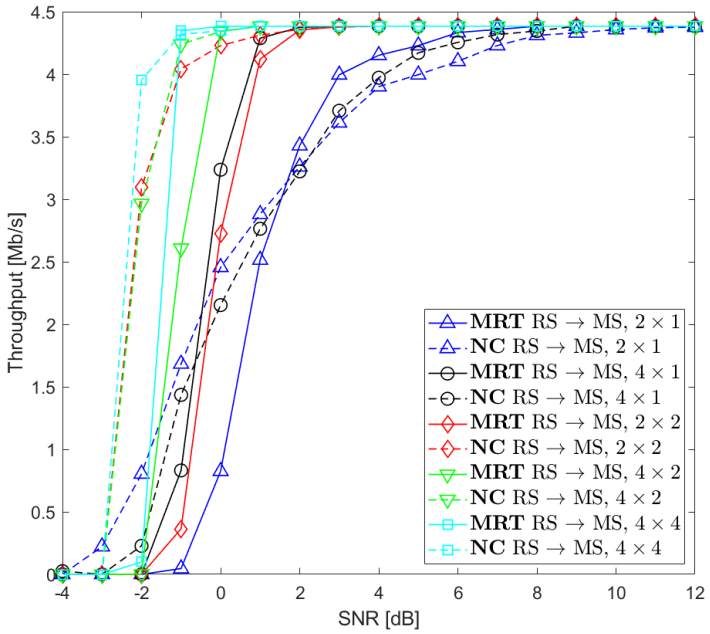

Figure 4.40: Comparison of network coding and MRT precoding in BR phase, throughput performance of the link between RS and MS

Chapter 5

Antijamming schemes for generalized MIMO Y channel

5.1 Introduction and related work

In wireless communication, numerous transceiver designs have been investigated to address the challenge of limited radio resources, such as time and frequency. Due to the broadcast nature of the wireless medium, simultaneous transmissions from multiple transmitters to their respective receivers within the same frequency band inevitably result in interference among them. In such communication scenarios, interference is a crucial factor that determines the performance limits of wireless networks. Consequently, effectively managing this interference at the receiver, where signals from multiple transmitters converge simultaneously, emerges as one of the primary challenges in wireless communication. Among all signaling schemes explored by numerous researchers that address the issue of interference and increase transmission rates, two gained a particular interest: network coding (described in more detail in Section 3.2) and interference alignment.

The interference alignment (IA) was introduced by Jafar in [45] and is based on overlapping interference signals at each receiver, thus reducing the dimensionality of the signal space occupied by the interference signals, while distinctly remaining the desired signal. As each receiver perceives a different picture, all interference signal vectors can be confined to approximately one-half of the signal space at each receiver. This leaves half of the other half free from interference and can be reserved for the desired signal.

In recent years, the use of relaying techniques has become increasingly recognized as an effective method to improve the reliability and throughput of wireless networks. To accommodate more than two users in the two-way relay channel, researchers in

[46] introduced a multi-user two-way relaying system. However, this system model faces a limitation on traffic pattern, since message exchange occurs separately for each user pair, thus point-to-multipoint transmission cannot be supported. To overcome this issue, the concept of a three-user relay channel was introduced in [47] and is a generalized version of the case of a two-way relay channel for more than two users. In this setup, each of the three users aims to transmit separate messages to the other users through a shared relay node. Communication involves a total of six messages exchanged in two time slots: Multiple Access (MA) and Broadcast (BC). The authors describe this channel model as MIMO Y channel and propose a new signaling method for the first time slot which was called a signal space alignment (SSA) for PNC. SSA is similar to the IA scheme, since both techniques make efficient use of the dimension of the signal space. However, while IA focuses on overlapping the interference signal vectors to minimize the dimension of the signal space occupied by the interference signals, the key idea of SSA is that the beamforming vectors are chosen in a way to align the desired signal vectors received from different users to jointly perform detection and encoding for network coding at the receiver of the relay.

The MIMO Y channel was further studied in [21] where the authors analyzed the achievable DOF and in [48], where the extended model was proposed to accommodate any number of K users. In [49] for the first time, the beamforming design of the MIMO Y channels was addressed and an iterative random beamforming algorithm was proposed. In [50] an optimization problem was formulated to maximize the system throughput of MIMO Y channels by taking advantage of adaptive modulation under the Bit Error Rate (BER) requirement. In [51] a combined scheme of IA and signal detection was addressed to optimize the performance of the MIMO Y channel. First, an iterative interference alignment algorithm was introduced to optimize both the beamforming and combining vectors, and then a signal detection scheme was applied in the relay to further deal with system interference. The simulation results showed that the proposed combined scheme for MIMO Y channels produced a significant improvement over the existing schemes. In [52] and [53] the authors studied the achievable DOF under the assumption of imperfect CSI.

Research on the SSA technique was continued in [54], where the authors studied the optimal precoding and power allocation problem of PNC-SA to maximize SNR at the receiver. In [55] based on SSA, an iterative algorithm was designed to choose beamforming vectors to maximize the minimum effective SINR among all data streams in the MIMO two-way X relay channel. The results showed that the proposed beamforming scheme can achieve significantly better error performance than random beamforming from [49]. The Generalized Signal Alignment (GSA) transmission scheme for the two-way MIMO X relay channel was introduced in [56] which, compared to existing SSA schemes, instead of directly aligning the signal subspaces using beamforming vectors applied at the transmitters, the alignment of the data signals is achieved after

a certain processing at the relay. The work was then extended by the authors in [57] for different antenna conditions and in [58] where the achievable DOF for the general multiuser MIMO two-way relay channels was analyzed. Some additional work related to SSA can be found in [59], [60], [61], and [62].

Although the authors in [47], [21], and [48] were the first to consider the application of SSA in the MIMO Y channel, they did not address the optimal design of the beamforming vectors. The beamforming design of MIMO Y channels appeared for the first time in [49], where a random beamforming algorithm was proposed. However, due to its random nature, for any given channel realization, the beamforming design could be far from optimal. In [63] and [64] the authors examined a generalized MIMO Y channel for K users and introduced a deterministic beamforming design to maximize the effective SNR for any specific channel realization. Following the design of the beamforming, an optimal power allocation scheme was proposed to maximize the sum rate. The proposed scheme significantly outperformed the random beamforming from [49].

The SSA is a prospective technique for interference management in wireless networks. However, despite the excellent work done on SSA, none of the papers has considered its robustness against jamming attacks. As our dependence on wireless services increases, security risks related to privacy, reliability, and accessibility of wireless communications have become an underlying concern. Among various security threats, such as eavesdropping and data fabrication, wireless networks are especially vulnerable to radio jamming attacks. The aim of an adversarial jammer is to generate jamming signals to intentionally disrupt legitimate wireless transmission and degrade the receiving performance [65]. There exist several types of jammers, and their common countermeasures are analyzed in [66]. Over the past decades, significant attention has been paid to studying antijamming strategies to mitigate the impacts of jamming and ensure the continuity of legitimate transmission. Among these strategies, the spread spectrum has been a conventional method used to combat jamming [67], [68]. However, spread-spectrum techniques lose effectiveness when faced with jammers that are broadband or possess high transmit power, surpassing the spreading gain. Consequently, several alternative and effective antijamming techniques have emerged in the realm of wireless networks in recent times [69], [70], and [71]. Wang *et al.* [69] explored security protocols in situations where secondary users are subjected to disruption by jamming attacks. The authors proposed a stochastic game aimed at defending against jamming within cognitive radio networks. In another study [70], the mobility of network nodes was innovatively used as a defense strategy against jamming. This involved designing node motion patterns that could dynamically adapt to the actions of the jammer. The authors in [71] introduced an antijamming scheme that allows reliable communication even in the presence of a high-power and broadband reactive jammer. Existing anti-

jamming attacks and antijamming strategies in wireless networks were collected and analyzed in the comprehensive survey [72].

In the context of IA scheme, antijamming issues were first examined in [73] and [74] for the MIMO X channel. The authors proposed a novel iterative antijamming IA scheme to remove interference and jamming signals. To effectively implement this antijamming IA scheme, the addition of more antennas or a reduction in the number of streams transmitted within the network is necessary. Consequently, feasibility conditions were established for the proposed antijamming IA scheme, considering scenarios with a single stream or multiple streams for each user. The simulation results demonstrated the effectiveness of the proposed antijamming IA scheme in mitigating both jamming and interferences between users. The research on IA MIMO X channel in the presence of a jammer was continued in [75], where the authors proposed a beneficial jamming scheme. The precoding vector of the jammer was designed to restrict the jamming signal into the same subspace as that of the interference between users at each receiver. Furthermore, the feasibility condition for this scheme was determined and the eavesdropping performance was thoroughly analyzed. Simulation results were provided to validate the efficacy of the proposed antijamming scheme. In [76] the authors developed a Minimizing Interference Leakage (MinIL) algorithm for IA-based networks in jamming scenarios that jointly optimize power splitting and transmit power of users in the network. The simulation results presented showed that the use of the MinIL algorithm leads to a decrease in the total transmission power of the entire network for low jamming power levels.

In the research presented in this chapter, attention was directed towards addressing the issue of antijamming in the SSA-based MIMO Y channel, which, to the best of available knowledge, is the first work concerning this topic. The main contributions of this section can be summarized as follows.

- Two antijamming schemes are proposed for the SSA-based MIMO Y channel with a single antenna jammer. In the first scheme, the jamming signal and interference are projected onto the null space of each pair of signals. In the second scheme, the interference originating from the jammer is removed in the relay by subtracting the disturbance estimate from the incoming signal.

- Monte Carlo simulation results are provided and compared with those received for the SSA-based MIMO Y channel for the iterative beamforming optimization algorithm presented in [64] for two scenarios when the jammer is present or not. These results can be treated as an upper bound for the proposed jammer scenarios.

This chapter expands upon the findings presented in the previous article of the author [77]. It includes additional results obtained from simulations involving an 8×8

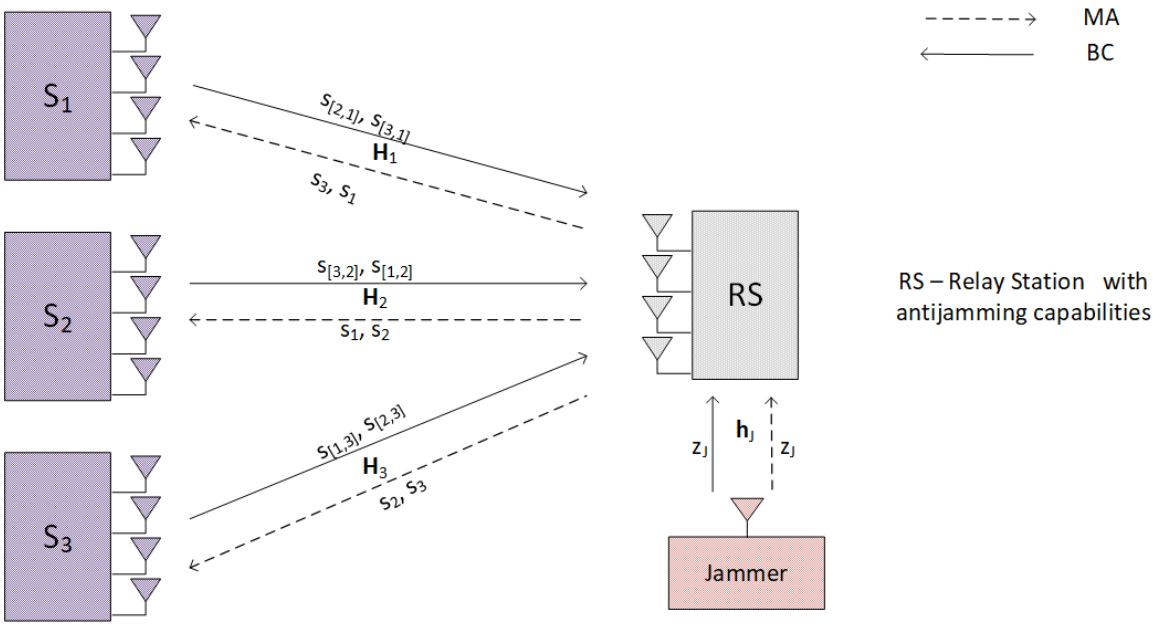

Figure 5.1: System model for K=3 (do poprawy rysunek (MA i BC źle podpisane)

antenna configuration across various jammer power levels, along with the introduction of new jammer power values.

Notations: For the reader's convenience let us recall the notations used in this thesis and introduce some new ones. $(.)^T$ and $(.)^H$ represent vector/matrix transpose and Hermitian transpose, respectively. $(.)^\dagger$ denotes the Moore-Penrose pseudoinverse. $|\boldsymbol{x}|$ stands for 2-norm of vector $\boldsymbol{x}$. $span(\boldsymbol{a})$ represents the subspace spanned by a vector $\boldsymbol{a}$. $ran(\boldsymbol{H})$ denotes the range (column space) of matrix $\boldsymbol{H}$. $\langle \boldsymbol{x} \rangle$ represents normalization operation on vector $\boldsymbol{x}$, i.e. $\langle \boldsymbol{x} \rangle = \frac{\boldsymbol{x}}{|x|}$.

5.2 System Model

Generalized MIMO Y channel model was examined, where K source nodes/users, denoted as $U_1, U_2, ..., U_K, (K \geq 3)$, each equipped with N_S antennas, communicate through a RS with N_R antennas. Users exchange $K-1$ independent messages and anticipate receiving the same number of messages from others. Communication between the relay and source nodes is distorted by an adversarial jammer. Suppose a flat fading channel, the channel coefficients between the user i and the relay form a $N_R \times N_S$ matrix $\boldsymbol{H}_i$ with full CSI assumed at all nodes. Such a channel model well reflects a realistic transmission on a single subcarrier of MIMO-OFDM system. The system model with $K = 3$ and a single antenna jammer is presented in Fig. 5.1. Transmission is divided into two phases: the MA phase and the Broadcast Channel (BC) phase. In the MA interval, all users send messages to the RS, which jointly detects and broadcasts them in the BC phase.

If the message sent by the user i to the user j is denoted as $s_{[j,i]}$, the signal sent by the user i to all $K-1$ users can be written as

$$\boldsymbol{x}_i = \sum_{j=1, j\neq i}^{K} \sqrt{\kappa_{[j,i]}}\boldsymbol{v}_{[j,i]} s_{[j,i]} \tag{5.1}$$

where $\kappa_{[j,i]}$ is the power scaling factor and $\boldsymbol{v}_{[j,i]}$ is the unit norm beamforming vector. The signal received by the relay in the MA phase is

$$\boldsymbol{r} = \sum_{i=1}^{K} \boldsymbol{H}_i \boldsymbol{x}_i + \boldsymbol{h}_J z_J + \boldsymbol{n}_R \tag{5.2}$$

where $\boldsymbol{h}_J$ is the vector of channel coefficients between the jammer and the relay, z_J is the jamming signal generated by the jammer and $\boldsymbol{n}_R$ is the Additive White Gaussian Noise (AWGN) vector with variance σ_n^2. The dimension of the received signal and noise vectors is $[N_R \times 1]$. Substituting (5.1) into (5.2) we get

$$\boldsymbol{r} = \sum_{i=1}^{K} \sum_{j=1, j\neq i}^{K} \boldsymbol{H}_i \sqrt{\kappa_{[j,i]}}\boldsymbol{v}_{[j,i]} s_{[j,i]} + \boldsymbol{h}_J z_J + \boldsymbol{n}_R \tag{5.3}$$

The basic idea of SSA is to pair the reciprocal messages $s_{[j,i]}$ and $s_{[i,j]}$ $(\forall i < j)$ so that (5.3) consists of $n_K \triangleq \binom{K}{2}$ message pairs. Then, equation (5.3) may be rewritten as

$$\boldsymbol{r} = \sum_{k=1}^{n_K} \left(\boldsymbol{H}_i \sqrt{\kappa_{[j,i]}}\boldsymbol{v}_{[j,i]} s_{[j,i]} + \boldsymbol{H}_j \sqrt{\kappa_{[i,j]}}\boldsymbol{v}_{[i,j]} s_{[i,j]} \right) + \boldsymbol{h}_J z_J + \boldsymbol{n}_R \tag{5.4}$$

The beamforming vectors must be designed in a way to align signal components within a pair, i.e. $span(\boldsymbol{H}_i \boldsymbol{v}_{[j,i]}) = span(\boldsymbol{H}_j \boldsymbol{v}_{[i,j]})$, $\forall i < j$. With a proper power allocation, we can write

$$\boldsymbol{u}_k = \sqrt{\kappa_{[j,i]}}\boldsymbol{H}_i \boldsymbol{v}_{[j,i]} = \sqrt{\kappa_{[i,j]}}\boldsymbol{H}_j \boldsymbol{v}_{[i,j]}, \forall k = \pi(i,j) \tag{5.5}$$

where $k = \pi(i,j)$ is a one-to-one index mapping function. Inserting (5.5) into (5.4) we get the following equation:

$$\boldsymbol{r} = \sum_{k=1}^{n_K} \boldsymbol{u}_k \left(s_{[j,i]} + s_{[i,j]} \right) + \boldsymbol{h}_j z_j + \boldsymbol{n}_R = \sum_{k=1}^{n_K} \boldsymbol{u}_k s_k + \boldsymbol{h}_j z_j + \boldsymbol{n}_R = \boldsymbol{U}\boldsymbol{s} + \boldsymbol{h}_J z_J + \boldsymbol{n}_R \tag{5.6}$$

where $s_k = s_{[j,i]} + s_{[i,j]}$ is k-th physical layer network coded symbol, $\boldsymbol{U} = [\boldsymbol{u}_1, \boldsymbol{u}_2, ..., \boldsymbol{u}_{n_K}]$ and $\boldsymbol{s} = [s_1, s_2, ..., s_{n_K}]^T$.

To decode the physical layer network coded symbols s_k, the relay station combines a received signal $\boldsymbol{r}$ with a unit norm combining vector $\boldsymbol{w}_k$ as

$$\boldsymbol{w}_k^H \boldsymbol{r} = \boldsymbol{w}_k^H \boldsymbol{u}_k s_k + \sum_{l=1, l\neq k}^{n_K} \boldsymbol{w}_k^H \boldsymbol{u}_l s_l + \boldsymbol{w}_k^H \boldsymbol{h}_J z_J + \boldsymbol{w}_k^H \boldsymbol{n}_R \tag{5.7}$$

5.2.1 Antijamming schemes in the MA phase

5.2.1.1 Antijamming signal space alignment (AJ-SSA)

In the proposed antijamming scheme based on SSA, the beamforming design presented in [64] is generalized to the scenario that contains an adversarial jammer. The combining vector $\boldsymbol{w}_k$ is chosen so that $\lambda_k = |\boldsymbol{w}_k^H \boldsymbol{u}_k|^2$ is maximized, while $\boldsymbol{w}_k^H \boldsymbol{u}_l = 0$ and $\boldsymbol{w}_k^H \boldsymbol{h}_J = 0$. To design a combining vector $\boldsymbol{w}_k$, define the following vector $\boldsymbol{G}_k = [\langle \boldsymbol{u}_1 \rangle, ..., \langle \boldsymbol{u}_{k-1} \rangle, \langle \boldsymbol{u}_{k+1} \rangle, ..., \langle \boldsymbol{u}_{n_k} \rangle, \langle \boldsymbol{h}_J \rangle]$. $\boldsymbol{w}_K$ should be placed in a null space of $\boldsymbol{G}_k^H$ and the effective gain λ_k should be maximized. Similarly to [78], given $\boldsymbol{u}_k$, a standard Lagranganian method will result in the following optimization solution.

$$\boldsymbol{w}_k = \langle \boldsymbol{M}_k \boldsymbol{u}_k \rangle \tag{5.8}$$

where

$$\boldsymbol{M}_k = \boldsymbol{I} - \boldsymbol{G}_k (\boldsymbol{G}_k^H \boldsymbol{G}_k)^{-1} \boldsymbol{G}_k^H \tag{5.9}$$

and the maximum effective channel gain is

$$\lambda_k = \boldsymbol{u}_k^H \boldsymbol{M}_k \boldsymbol{u}_k. \tag{5.10}$$

Thus, equation (5.7) takes the form

$$\boldsymbol{w}_k^H \boldsymbol{r} = \sqrt{\lambda_k} s_k + \boldsymbol{w}_k^H \boldsymbol{n}_R \tag{5.11}$$

and the effective SNR for the message pair k is equal to

$$\gamma_k = \frac{2\lambda_k}{\sigma_n^2} \tag{5.12}$$

for $k = 1, 2, ..., n_K$.

The optimization problem of beamforming design and power allocation can be formulated as [64]

$$\begin{aligned} &\underset{\boldsymbol{v}_{[j,i]}, \kappa_{[j,i]}}{\text{maximize}} \quad \min(\lambda_1, ..., \lambda_k) \\ &\text{subject to} \\ &\sqrt{\kappa_{[j,i]}} \boldsymbol{H}_i \boldsymbol{v}_{[j,i]} = \sqrt{\kappa_{[i,j]}} \boldsymbol{H}_j \boldsymbol{v}_{[i,j]}, \forall i \neq j \\ &|\boldsymbol{v}_{[j,i]}| = 1, \forall i \neq j \\ &E\left[|\boldsymbol{x}_i|^2\right] \leq P_i, i = 1, ..., K, \end{aligned} \tag{5.13}$$

where P_i is the transmit power constraint on source i.

5.2.1.2 Beamforming Optimization

The optimization problem in (5.13) was solved in [64]. First, the authors decoupled optimization over beamforming from power allocation. The beamforming vectors are

optimized for each message pair at a time while treating other beamforming vectors as fixed. This resulted in the following subproblem for each message pair $k = \pi(i, j)$:

$$\begin{aligned} &\underset{\boldsymbol{v}_{[j,i]}, \boldsymbol{v}_{[i,j]}}{\text{maximize}} \quad \left(\lambda_{[j,i]}^{-1} + \lambda_{[i,j]}^{-1}\right)^{-1} \\ &\text{subject to} \\ &\langle \boldsymbol{u}_k \rangle = \langle \boldsymbol{H}_i \boldsymbol{v}_{[i,j]} \rangle = \langle \boldsymbol{H}_j \boldsymbol{v}_{[j,i]} \rangle \\ &|\boldsymbol{v}_{[j,i]}| = |\boldsymbol{v}_{[i,j]}| = 1 \end{aligned} \tag{5.14}$$

where $\lambda_{[j,i]}$ and $\lambda_{[i,j]}$ are the effective channel gains without power scaling.

$$\lambda_{[j,i]} = \boldsymbol{v}_{[j,i]}^H \boldsymbol{H}_i^H \boldsymbol{M}_k \boldsymbol{H}_i \boldsymbol{v}_{[j,i]} \tag{5.15}$$

$$\lambda_{[i,j]} = \boldsymbol{v}_{[i,j]}^H \boldsymbol{H}_j^H \boldsymbol{M}_k \boldsymbol{H}_j \boldsymbol{v}_{[i,j]} \tag{5.16}$$

The optimization problem (5.14) was solved for two cases: $N_S \geq N_R$ and $N_S < N_R$. When $N_S \geq N_R$ the optimization problem reduces to the generalized Rayleigh quotient

$$\begin{aligned} &\underset{\boldsymbol{v}_{[j,i]}}{\text{maximize}} \quad \frac{\boldsymbol{v}_{[j,i]}^H \boldsymbol{H}_i^H \boldsymbol{M}_k \boldsymbol{H}_i \boldsymbol{v}_{[j,i]}}{\boldsymbol{v}_{[j,i]}^H \left(\boldsymbol{I} + \left(\boldsymbol{H}_j^\dagger \boldsymbol{H}_i\right)^H \left(\boldsymbol{H}_j^\dagger \boldsymbol{H}_i\right)\right) \boldsymbol{v}_{[j,i]}} \\ &\text{subject to} \quad |\boldsymbol{v}_{[j,i]}| = 1 \end{aligned} \tag{5.17}$$

where the maximum is obtained when $\boldsymbol{v}_{[j,i]}$ is the generalized eigenvector corresponding to the largest generalized eigenvalue of $\boldsymbol{H}_i^H \boldsymbol{M}_k \boldsymbol{H}_i$ and $\left(\boldsymbol{I} + \left(\boldsymbol{H}_j^\dagger \boldsymbol{H}_i\right)^H \left(\boldsymbol{H}_j^\dagger \boldsymbol{H}_i\right)\right)$.

To solve the Generalized Rayleigh Quotient it must be reduced to the Rayleigh Quotient. First, rewrite (5.17) as

$$\underset{\boldsymbol{x}}{\text{maximize}} \quad \frac{\boldsymbol{x}^H \boldsymbol{A} \boldsymbol{x}}{\boldsymbol{x}^H \boldsymbol{B} \boldsymbol{x}} \tag{5.18}$$

where $\boldsymbol{x} = \boldsymbol{v}_{[j,i]}$, $\boldsymbol{A} = \boldsymbol{H}_i^H \boldsymbol{M}_k \boldsymbol{H}_i$ and $\boldsymbol{B} = \boldsymbol{I} + \left(\boldsymbol{H}_j^\dagger \boldsymbol{H}_i\right)^H \left(\boldsymbol{H}_j^\dagger \boldsymbol{H}_i\right)$. Define $\boldsymbol{B} = \boldsymbol{D}^H \boldsymbol{D}$, $\boldsymbol{C} = \boldsymbol{D}^{-H} \boldsymbol{A} \boldsymbol{D}^{-1}$ and $\boldsymbol{y} = \boldsymbol{D}\boldsymbol{x}$:

$$\frac{\boldsymbol{x}^H \boldsymbol{A} \boldsymbol{x}}{\boldsymbol{x}^H \boldsymbol{B} \boldsymbol{x}} = \frac{\boldsymbol{x}^H \boldsymbol{D}^H \boldsymbol{D}^{-H} \boldsymbol{A} \boldsymbol{D}^{-1} \boldsymbol{D} \boldsymbol{x}}{\boldsymbol{x}^H \boldsymbol{D}^H \boldsymbol{D} \boldsymbol{x}} = \frac{\boldsymbol{x}^H \boldsymbol{D}^H \boldsymbol{C} \boldsymbol{D} \boldsymbol{x}}{\boldsymbol{y}^H \boldsymbol{y}} = \frac{\boldsymbol{y}^H \boldsymbol{C} \boldsymbol{y}}{\boldsymbol{y}^H \boldsymbol{y}} \tag{5.19}$$

After several transformations, we receive the Rayleigh Quotient with the symmetric matrix $\boldsymbol{C}$ and the unit vector $\boldsymbol{y}$. The solution is the first eigenvector of $\boldsymbol{C}$. Once $\boldsymbol{v}_{[j,i]}$ is obtained, $\langle \boldsymbol{u}_k \rangle$ and $\boldsymbol{v}_{[i,j]}$ can be calculated.

When $N_S < N_R$ the optimization problem (5.13) reduces to

$$\begin{aligned} &\underset{\boldsymbol{c}_k}{\text{maximize}} \quad \frac{\boldsymbol{c}_k \boldsymbol{B}_k^H \boldsymbol{M}_k \boldsymbol{B}_k \boldsymbol{c}_k}{\boldsymbol{c}_k^H \boldsymbol{B}_k^H \left(\boldsymbol{H}_i^{\dagger H} \boldsymbol{H}_i^\dagger + \boldsymbol{H}_j^{\dagger H} \boldsymbol{H}_j^\dagger\right) \boldsymbol{B}_k \boldsymbol{c}_k} \\ &\text{subject to} \quad |\boldsymbol{c}_k| = 1 \end{aligned} \tag{5.20}$$

where $\boldsymbol{B}_k$ is an orthonormal basis of the intersection subspace $ran(\boldsymbol{H}_i) \cap ran(\boldsymbol{H}_j)$, $\boldsymbol{c}_k$ is a length $n_I = 2N_S - N_R$ vector with unit norm, and the relation between $\boldsymbol{B}_k$, $\boldsymbol{c}_k$ and the beamforming vectors $\boldsymbol{v}_{[i,j]}$, $\boldsymbol{v}_{[j,i]}$ takes the following form:

$$\boldsymbol{v}_{[j,i]} = \langle \boldsymbol{H}_i^{\dagger} \boldsymbol{B}_k \boldsymbol{c}_k \rangle, \boldsymbol{v}_{[i,j]} = \langle \boldsymbol{H}_j^{\dagger} \boldsymbol{B}_k \boldsymbol{c}_k \rangle \tag{5.21}$$

The optimization problem (5.20), similar to (5.17), takes the form of a generalized Rayleigh quotient, where the solution is the largest generalized eigenvector corresponding to the largest generalized eigenvalue of $\boldsymbol{B}_k^H \boldsymbol{M}_k \boldsymbol{B}_k$ and $\boldsymbol{B}_k^H \left(\boldsymbol{H}_i^{\dagger H} \boldsymbol{H}_i^{\dagger} + \boldsymbol{H}_j^{\dagger H} \boldsymbol{H}_j^{\dagger} \right) \boldsymbol{B}_k$. Once $\boldsymbol{c}_k$ is obtained, the beamforming vectors $\boldsymbol{v}_{[j,i]}$, $\boldsymbol{v}_{[i,j]}$ may be calculated.

5.2.1.3 Power allocation

Whereas the beamforming optimization determines the "shape" of the beamforming vectors, power allocation determines the "length" of these vectors. Then the power optimization problem receives the form [64]:

$$\begin{aligned} \underset{\kappa_{[j,i]} i<j}{\text{minimize}} \quad & \sum_{k=1}^{n_k} \left(\kappa_{[j,i]} \lambda_{[j,i]} \right)^{-1} \\ \text{subject to} \quad & \sum_{j=1}^{i-1} \frac{\lambda_{[i,j]}}{\lambda_{[j,i]}} \kappa_{[i,j]} + \sum_{j=i+1}^{K} \kappa_{[j,i]} \leq P_i, \; i = 1, \ldots, K. \end{aligned} \tag{5.22}$$

It can be easily seen that the above problem is a convex optimization problem that can be solved by the interior point method.

5.2.1.4 Jammer's Interference Cancellation (J-IC)

In this method, the combining vector $\boldsymbol{w}_k$ is chosen so that $\lambda_k = |\boldsymbol{w}_k^H \boldsymbol{u}_k|^2$ is maximized while $\boldsymbol{w}_k^H \boldsymbol{u}_l = 0$. The beamforming vectors are chosen according to (5.17) and (5.20). The interference from the jammer is canceled in the relay according to the formula.

$$\tilde{\mathbf{r}} = \mathbf{r} - \mathbf{h}_J \hat{d} \quad \text{where} \quad \hat{d} = \arg\min_{\{d_i\}} \|\mathbf{r} - \mathbf{h}_J d_i\|^2 \tag{5.23}$$

As in the previously considered antijamming method, it is assumed that the channel coefficients $\mathbf{h}_J$ between the jammer and the receive antenna of the relay are known. Assuming the additive white Gaussian noise contained in the received signal $\mathbf{r}$ (see (5.3) the most probable jamming data symbol $\hat{d}$ drawn from the data symbol set $\{d_1, d_2, ..., d_M\}$ (where M is the modulation size) is the one that minimizes the norm in (5.23). The brute-force search over all data symbols contained in a given modulation format is the simplest method to find the most likely jamming data symbol.

5.2.2 Computational Complexity of the proposed algorithms

To compare the computational complexity of the two proposed algorithms, the differences in terms of the calculation of the precoding vectors and the equalizer operations at the relay's receiver will be examined. With the AJ-SSA algorithm, the matrix $\boldsymbol{G_k}$ in (5.9) has N_J more columns compared to the matrix $\boldsymbol{G_k}$ used in the J-IC algorithm, leading to higher computational complexity for the calculation of precoding vectors in the AJ-SSA algorithm. The operations on matrix $\boldsymbol{G_k}$ of size $N_R \times P$ in (5.9), where $P = n_K - 1 + N_J$ for the AJ-SSA and $P = n_K - 1$ for the J-IC, begin with the calculation of the matrix M_k, which involves the following steps:

- $\boldsymbol{G}_k^H$ – transposing a $N_R \times P$ matrix has time complexity $O(N_R \cdot P)$,
- $\boldsymbol{G}_k^H \boldsymbol{G}$ – matrix multiplication resulting in a $P \times P$ matrix with complexity $O(P^2 \cdot N_R)$,
- $(\boldsymbol{G}_k^H \boldsymbol{G}_k)^{-1}$ – inverting an $P \times P$ matrix has complexity $O(P^3)$,
- $\boldsymbol{G}_k(...)^{-1}$ – multiplying $N_R \times P$ with $P \times P$ has complexity $O(P^2 \cdot N_R)$,
- multiplying the $N_R \times P$ result with $\boldsymbol{G}_k^H$ $P \times N_R$ and complexity of $O(N_R^2 \cdot P)$
- subtraction with $\boldsymbol{I}$ of size $N_R \times N_R$ is straightforward and has complexity $O(N_R^2)$

with total computational complexity equal to $O((1+P)N_R^2+(2P^2+P)N_R+P^3)$. Since the size of the matrix M_k is equal to $N_R \times N_R$ and does not depend on the size P, the complexity of the remaining calculations stays the same for both algorithms. Since the channel is assumed flat for each Virtual Resource Block (VRB) these operations are performed only once for each VRB resulting in the complexity of $O(N_{VRB}((1 + P)N_R^2 + (2P^2 + P)N_R + P^3))$, where N_{VRB} is the number of VRBs per transmission slot.

In the relay equalizer, the received data is multiplied by the vector $\boldsymbol{w}_k^H$. As shown in (5.9), to calculate the vector $\boldsymbol{w}_k^H$, the matrix M_k must first be calculated. As derived in the previous paragraph, the computational complexity of the calculation of the matrix M_k equals $O(N_{VRB}((1+P)N_R^2+(2P^2+P)N_R+P^3))$. In addition, for the J-IC algorithm, cancelation of jammer interference is performed according to (5.23). The computational complexity of this operation equals $O(N_D((1+M)N_R))$, where N_D is the number of data symbols and M is the modulation size (for QPSK $M = 4$).

Taking the derived computational complexities for both algorithms, we can notice that the calculation of the precoding vectors takes more operations for the AJ-SSA algorithm; however, the equalization process is more time consuming for J-IC solution. Since N_D is much larger than N_{VRB}, the J-IC algorithm requires many more operations than AJ-SSA. For the simulated scenario with $N_{VRB} = 6$, $M = 4$ and $N_D = 648$ J-IC

algorithm required 6.34 and 5.4 times more operations than AJ-SSA for $N_R = 4$ and $N_R = 8$ respectively.

5.2.3 Antijamming signal space alignment in the BC phase

Similarly to [49] the symmetry of the MA and BC phases is assumed, so the same transmit and receive combining vectors from the MA phase can be used as the receive combining and transmit beamforming vectors in the BC phase, respectively.

5.3 Simulation Results

5.3.1 Simulation procedure and parameters

The performance of the proposed antijamming schemes has been evaluated through link-level simulations. The most important simulation parameters are presented in Table 5.1. The channel between each source node and the relay node is a multipath fading channel model with the delay profile according to EPA and a maximum Doppler frequency of 5 Hz. OFDM transmission is applied; thus, multipath propagation is neutralized by the cyclic prefix CP, and the channel seen on each subcarrier is flat fading. As MIMO technology is applied, the channels for each subcarrier between the terminals and the relay station are fully characterized by the matrices whose size results from the number of transmit and receive antennas in the MIMO system. The channel coefficients between each antenna are assumed to be uncorrelated.

Table 5.1: Simulation parameters.

Parameter	**Value**
Radio Channel	EPA 5Hz
Channel Estimation	Ideal
Channel Coding	LDPC NR, rate 1/3
Modulation	QPSK
Multiplexing	OFDM
Subcarrier Spacing	60 kHz
Slot length	0.25 ms
OFDM symbol length	16.67 us
CP length	1.2 us
Subframes in a frame	10
Slots in a subframe	4
OFDM symbols in a slot	14
Subcarriers in a PRB	12
PRB width	0.72 MHz
Number of PRBs	6

As presented in Table 5.1, the parameters of the applied transmission system are specific to the numerology selected for the 5G NR. The main aim of conducting simulations was to estimate the achievable block error rate (BLER). It was assumed that, as in many other systems, the final performance is achieved after application of the hybrid ARQ technique or the ARQ technique implemented in the radio link control sublayer. Thus, obtaining a BLER on the order of 10^{-2} — 10^{-3} before using ARQ is sufficient to achieve satisfactory transmission system performance.

To obtain accurate results in the form of BLER values as a function of SNR, each SNR point was simulated for a minimum of 500 different channel realizations. In each channel realization, results from the transmission of 20 slots were collected If the minimum number of erroneous blocks (100) was not reached after simulating a minimum of 10,000 slots, the simulation was continued until either 100 errors had been accumulated or the maximum number of simulated slots (1000000) had been reached.

When applying the proposed antijamming schemes during the MA phase, it is assumed that the relay has complete knowledge of all channel coefficients and that the source nodes receive notification along with their corresponding precoding vectors computed by the relay. The ideal CSI is a common assumption in numerous other publications that focus on signal space alignment or interference alignment techniques. In this context, the results represent the upper limit of the performance achievable with both methods. However, it would be valuable to validate the proposed algorithms under conditions of real channel estimation, which would be the focus of future work. In that case, the channel between the source nodes and the relay could be estimated using 5G NR DMRS, with a pattern best suited to the given use case scenario. The channel coefficients vector between the jammer and the relay should be estimated based on blind channel estimation, which can obtain CSI without training sequence or pilots as proposed in the following publications [79], [80], [81], [82], [83], [84], [85].

5.3.2 Simulation Results

Figs. 5.2-5.17 present the BLER curves of the proposed schemes (called AJ-SSA, and J-IC) for the MA phase, for various antenna configurations and jammer power. Furthermore, for comparison purposes, the results of the iterative beamforming optimization algorithm presented in [64] (marked SSA) were incorporated for two scenarios: one without a jammer (serving as the upper bound results) and another with the presence of the jammer.

In Figs. 5.2, 5.3 and 5.4, the results are presented for four transmit antennas and four receive antennas. The curves between the source nodes and the relay are denoted as S1→R, S2→R, and S3→R where S1, S2, and S3 represent each of the three source nodes.

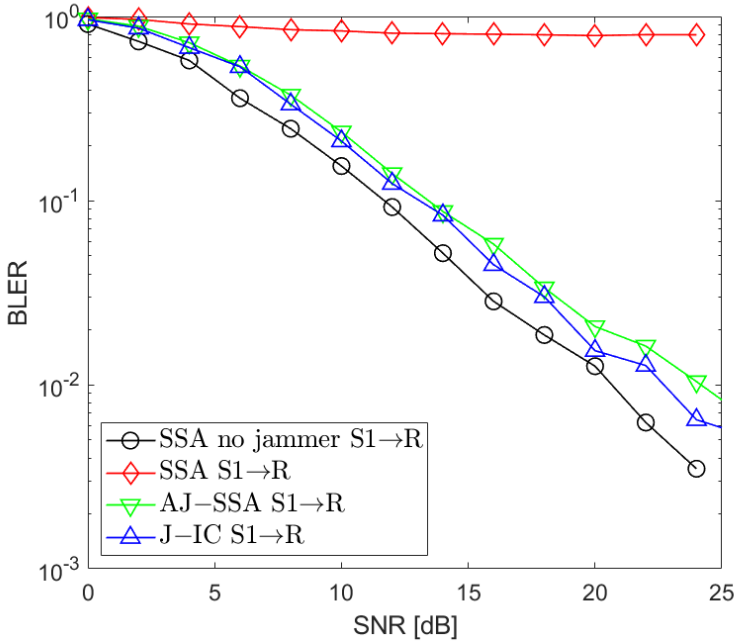

Figure 5.2: BLER performance: $N_R = 4$, $N_S = 4$ (SSA - Signal Space Alignment, AJ-SSA - Antijamming SSA, J-IC - Jammer's Interference Cancellation), $P_J = 0$ dB, link between Source 1 and Relay

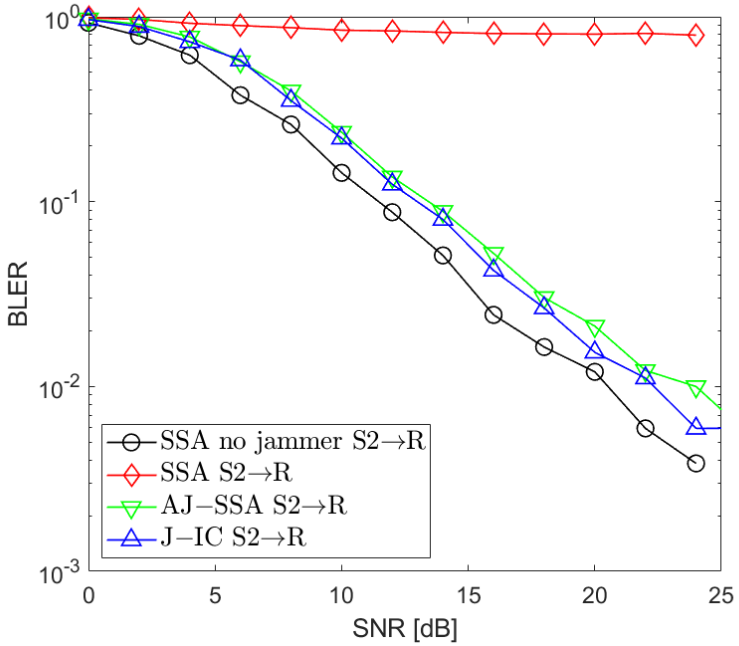

Figure 5.3: BLER performance: $N_R = 4$, $N_S = 4$ (SSA - Signal Space Alignment, AJ-SSA - Antijamming SSA, J-IC - Jammer's Interference Cancellation), $P_J = 0$ dB, link between Source 2 and Relay

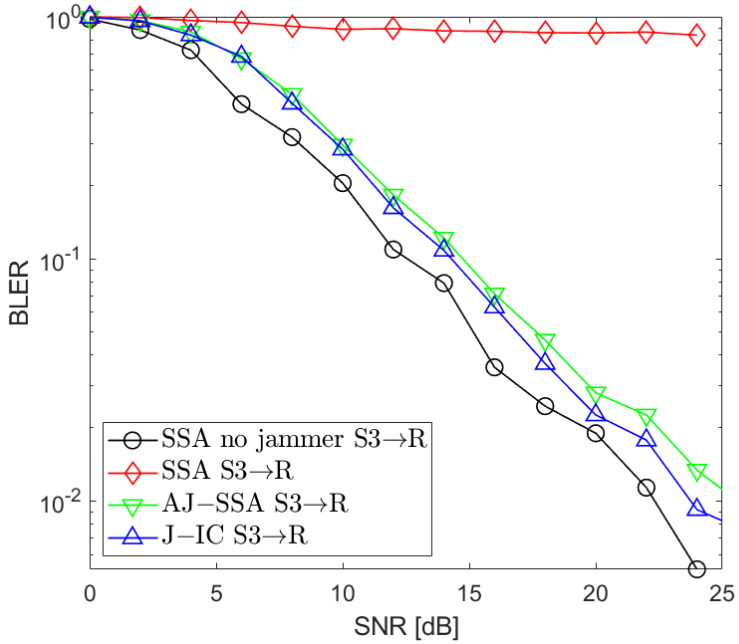

Figure 5.4: BLER performance: $N_R = 4$, $N_S = 4$ (SSA - Signal Space Alignment, AJ-SSA - Antijamming SSA, J-IC - Jammer's Interference Cancellation), $P_J = 0$ dB, link between Source 3 and Relay

It can be seen that the best results were achieved for iterative beamforming in the scenario where a jammer is not present (denoted as "SSA no jammer"). The performance of this algorithm decreases significantly when the jammer generates interference. In the figures mentioned above, the jammer power was equal to 0 dB ($P_J = 0$ dB). In that case, transmission is not possible since, despite the increase in the SNR level, BLER does not drop below 75%. Compared to the SSA scheme, it can be seen that both proposed antijamming schemes significantly mitigate the negative impact of the jammer. The results obtained for antijamming SSA and jammer interference cancelation schemes achieve performance similar to the SSA scheme with no jammer. There is around 1.5 dB loss between the upper bound solution without jammer and the proposed J-IC scheme, and another 1 dB to the proposed AJ-SSA scheme. For the 4x4 antenna configuration, J-IC slightly outperforms the AJ-SSA scheme.

The 8x8 antenna configuration is illustrated in Fig. 5.5, Fig. 5.6 and Fig. 5.7. Each figure shows the results for different source and relay pairs. The jammer power is set to $P_J = 0$ dB. Similarly, when the jammer generates interference, the transmission is interrupted when the regular SSA scheme is applied. Both the proposed antijamming schemes AJ-SSA and J-IC effectively reduce the adverse effects caused by the jammer. The loss to the SSA scheme without the jammer is less compared to the 4x4 antenna configuration, achieving around 0.5 dB in the average. The J-IC scheme offers a slight improvement over AJ-SSA, but the difference is minimal.

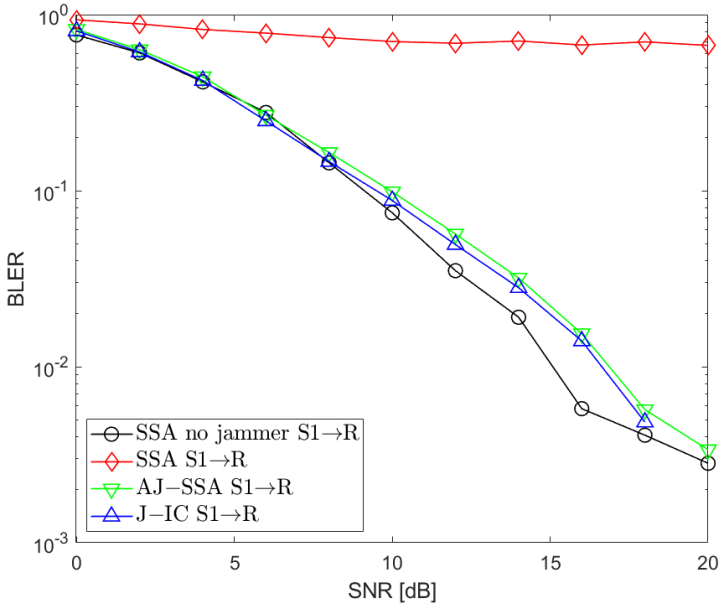

Figure 5.5: BLER performance: $N_R = 8$, $N_S = 8$ (SSA - Signal Space Alignment, AJ-SSA - Antijamming SSA, J-IC - Jammer's Interference Cancellation), $P_J = 0$ dB, link between Source 1 and Relay

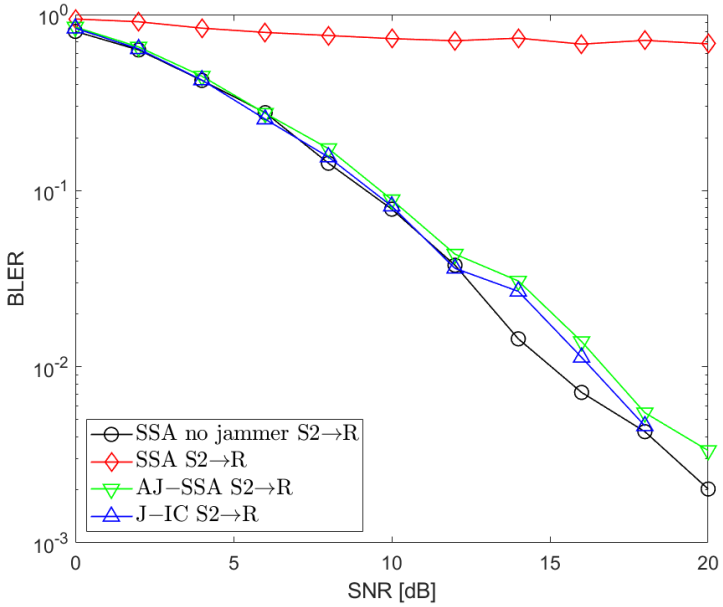

Figure 5.6: BLER performance: $N_R = 8$, $N_S = 8$ (SSA - Signal Space Alignment, AJ-SSA - Antijamming SSA, J-IC - Jammer's Interference Cancellation), $P_J = 0$ dB, link between Source 2 and Relay

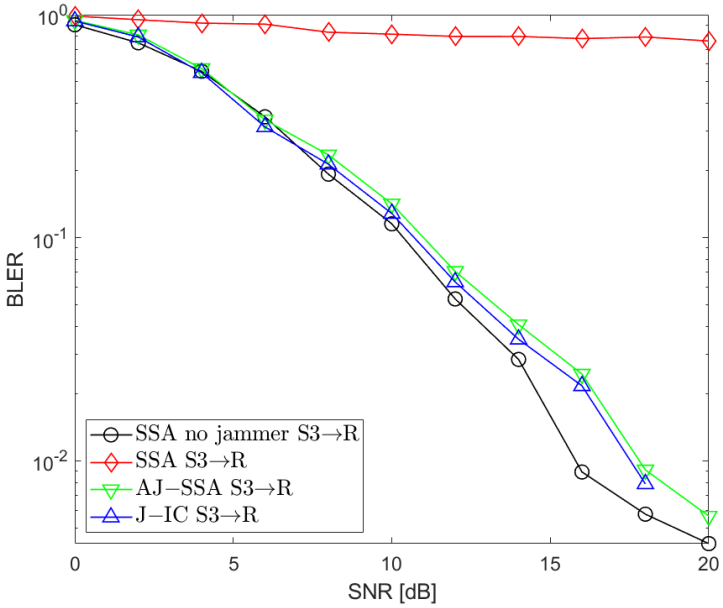

Figure 5.7: BLER performance: $N_R = 8$, $N_S = 8$ (SSA - Signal Space Alignment, AJ-SSA - Antijamming SSA, J-IC - Jammer's Interference Cancellation), $P_J = 0$ dB, link between Source 3 and Relay

Additional investigations were carried out to determine which of the two algorithms performs best under varying jammer power levels. Simulations were carried out for jammer powers of $P_J = -3$, 0, 3, 6, 9 and 12 dB with respect to the useful signals generated by the data sources. The results for the 4×4 antenna configuration are shown in Fig. 5.8, Fig. 5.9, Fig. 5.10, Fig. 5.11 and Fig. 5.12. For the 8×8 antenna configuration, see Fig. 5.13, Fig. 5.14, Fig. 5.15, Fig. 5.16 and Fig. 5.17. The simulation results indicate that in the scenario with 4×4 antennas, the proposed antijamming signal space alignment algorithm outperforms the jammer interference canceller when the jammer power is relatively low. Conversely, when the jammer power exceeds the power of the useful signals, the jammer cancellation-based algorithm maintains superior performance, surpassing the signal space alignment approach across all signal sources, including the jamming signal. In such scenarios, the interference canceller effectively identifies the QPSK jamming symbol, leading to reliable jammer compensation. In the 8×8 antenna scenario, when the jammer power is equal to -3 dB, the Aj-SSA algorithm again achieves better results. However, for jammer powers of $3, 6, 9$ and 12 dB, the performance of the Aj-SSA and J-IC algorithms is comparable.

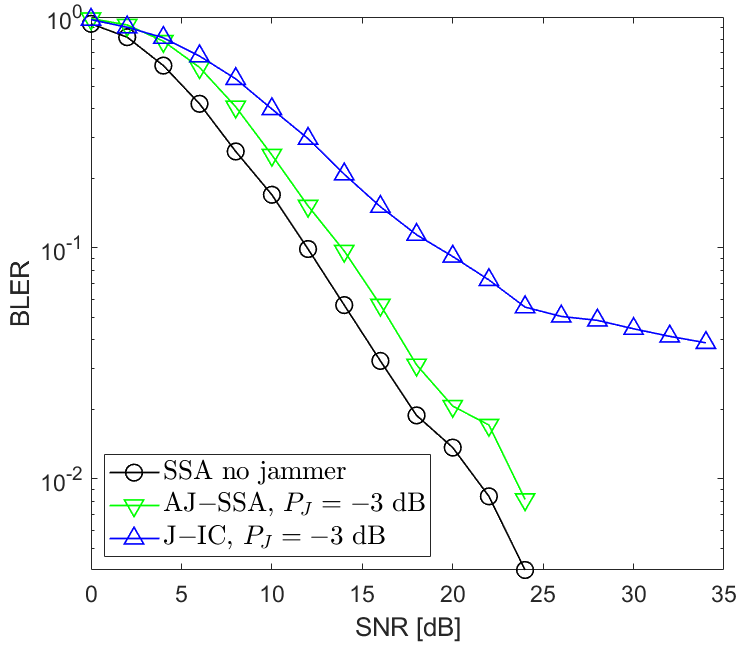

Figure 5.8: BLER performance: $N_R = 4$, $N_S = 4$ (SSA - Signal Space Alignment, AJ-SSA - Antijamming SSA, J-IC - Jammer's Interference Cancellation), $P_J = -3$ dB, the average of all sources

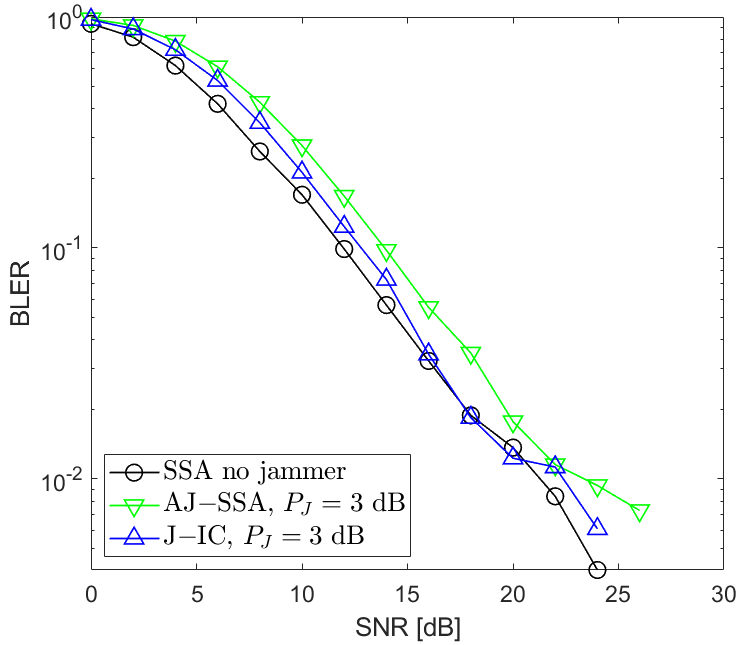

Figure 5.9: BLER performance: $N_R = 4$, $N_S = 4$ (SSA - Signal Space Alignment, AJ-SSA - Antijamming SSA, J-IC - Jammer's Interference Cancellation), $P_J = 3$ dB, the average of all sources

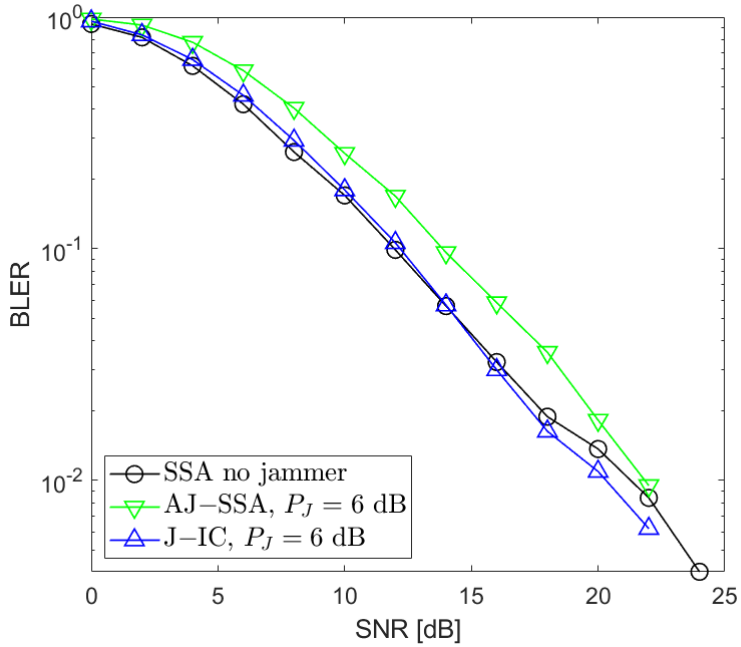

Figure 5.10: BLER performance: $N_R = 4$, $N_S = 4$ (SSA - Signal Space Alignment, AJ-SSA - Antijamming SSA, J-IC - Jammer's Interference Cancellation), $P_J = 6$ dB, the average of all sources

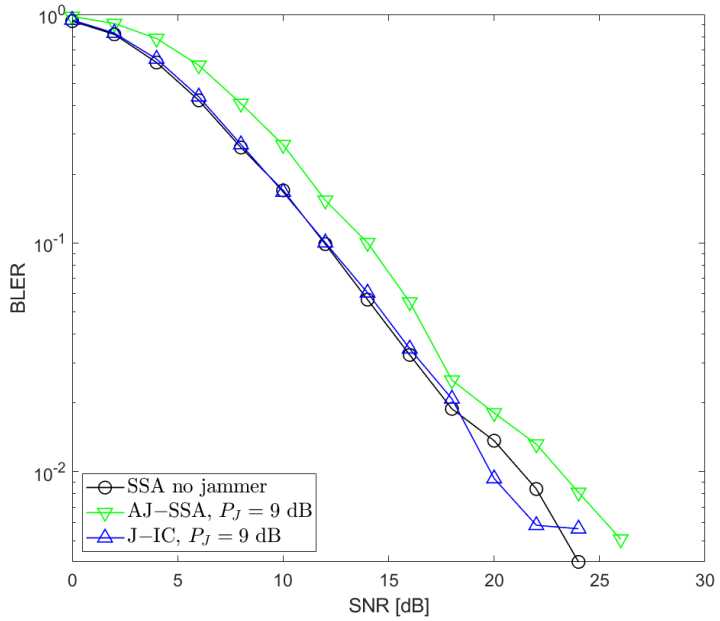

Figure 5.11: BLER performance: $N_R = 4$, $N_S = 4$ (SSA - Signal Space Alignment, AJ-SSA - Antijamming SSA, J-IC - Jammer's Interference Cancellation), $P_J = 9$ dB, the average of all sources

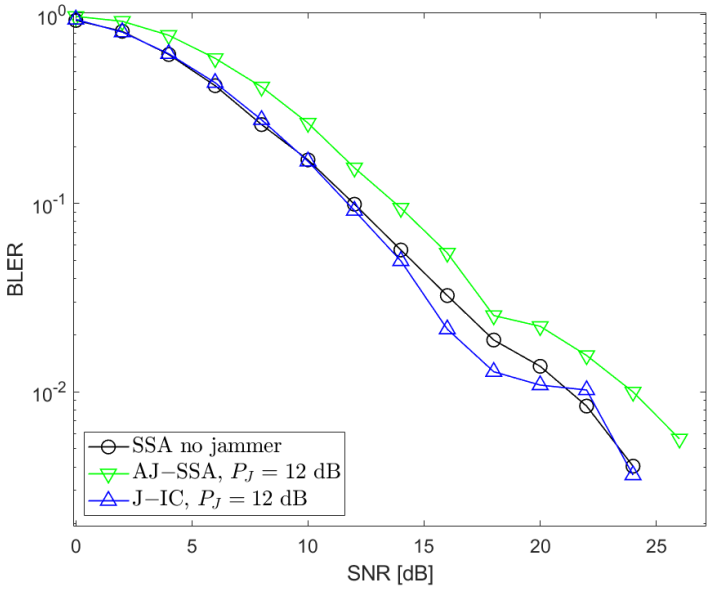

Figure 5.12: BLER performance: $N_R = 4$, $N_S = 4$ (SSA - Signal Space Alignment, AJ-SSA - Antijamming SSA, J-IC - Jammer's Interference Cancellation), $P_J = 12$ dB, the average of all sources

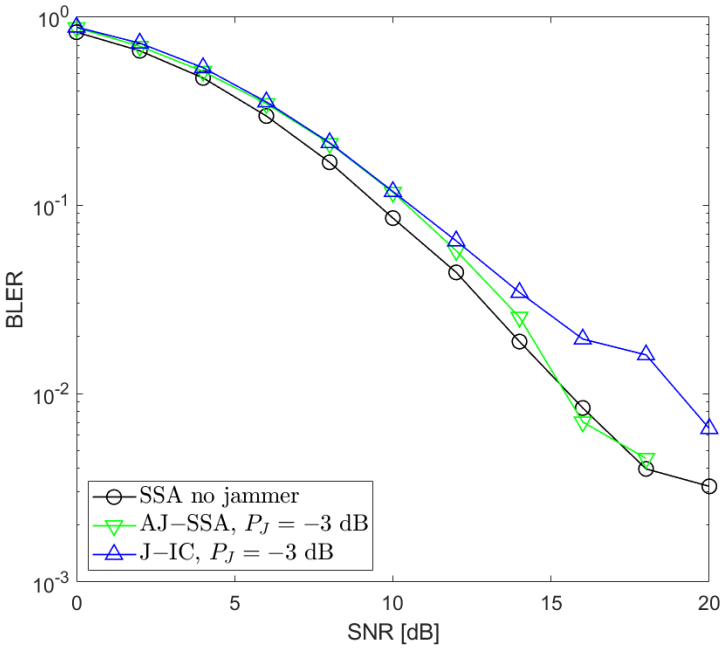

Figure 5.13: BLER performance: $N_R = 8$, $N_S = 8$ (SSA - Signal Space Alignment, AJ-SSA - Antijamming SSA, J-IC - Jammer's Interference Cancellation), $P_J = -3$ dB, the average of all sources

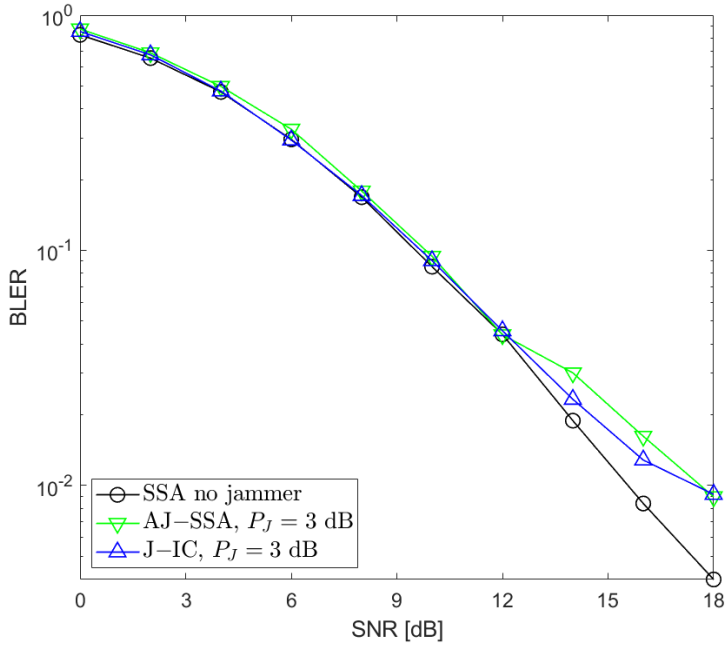

Figure 5.14: BLER performance: $N_R = 8$, $N_S = 8$ (SSA - Signal Space Alignment, AJ-SSA - Antijamming SSA, J-IC - Jammer's Interference Cancellation), $P_J = 3$ dB, the average of all sources

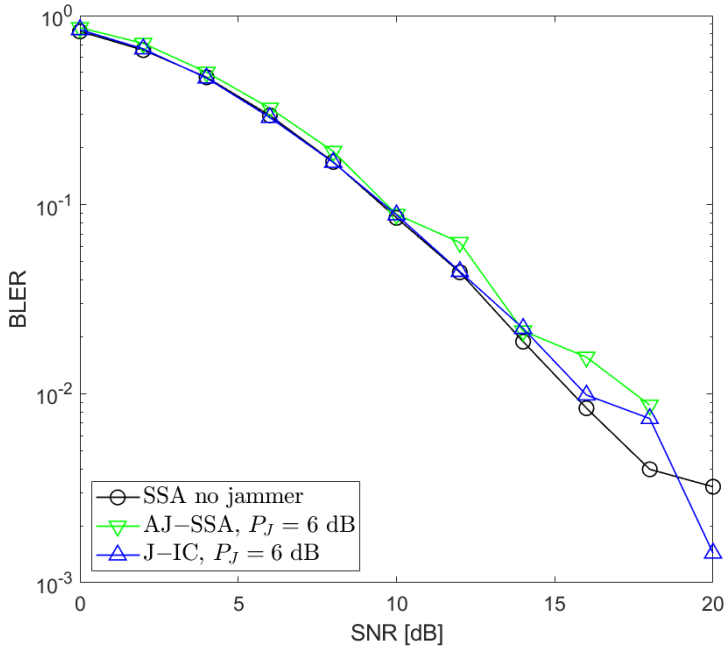

Figure 5.15: BLER performance: $N_R = 8$, $N_S = 8$ (SSA - Signal Space Alignment, AJ-SSA - Antijamming SSA, J-IC - Jammer's Interference Cancellation), $P_J = 6$ dB, the average of all sources

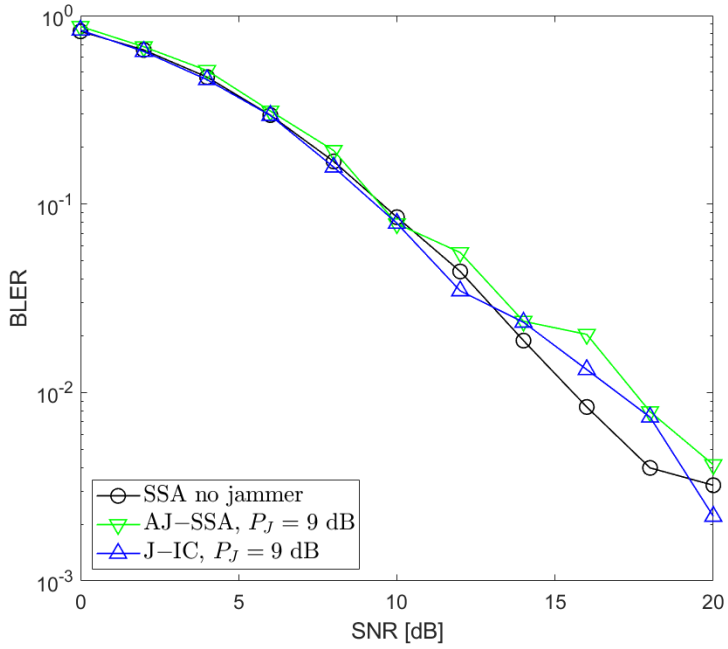

Figure 5.16: BLER performance: $N_R = 8$, $N_S = 8$ (SSA - Signal Space Alignment, AJ-SSA - Antijamming SSA, J-IC - Jammer's Interference Cancellation), $P_J = 9$ dB, the average of all sources

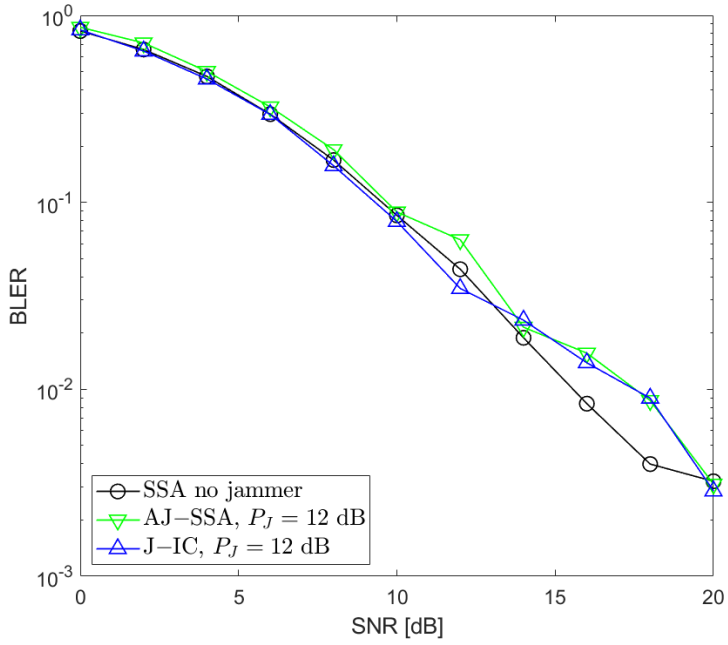

Figure 5.17: BLER performance: $N_R = 8$, $N_S = 8$ (SSA - Signal Space Alignment, AJ-SSA - Antijamming SSA, J-IC - Jammer's Interference Cancellation), $P_J = 12$ dB, the average of all sources

5.4 Conclusions and Future Work

This study developed two approaches for jamming suppression in a wireless MIMO Y-channel data exchange system. The first takes into account the presence of a jamming terminal as an additional source of information in the overall optimization of precoding vectors based on the signal-space alignment method. The second method relies on the simple elimination of the jamming signal by searching for data symbols that minimize the received signal power after cancelation. In both methods, CSI for all composite channels is assumed, which is a frequent assumption in many other publications dealing with signal space alignment or interference alignment techniques. From that point of view, the results can be viewed as the upper bound of the performance of both methods. Simulations have shown that both jamming suppression methods result in similar performance and are worth implementing, in particular, if an effective estimation of all composite channels is worked out.

Chapter 6

Conclusions

In this dissertation, new two-way relaying transmission schemes have been investigated for 5G wireless communication systems. In particular, the dissertation focuses on two important aspects of bidirectional transmission through the multi-antenna relay such as flexible design and resilience against jammer attacks. New transceiver designs have been proposed to address these problems.

To address the first issue, Chapter 4 introduces the Maximum Ratio Transmission (MRT) precoder and its codebook-based version (CB-MRT) for the broadcast phase of two-way relaying assuming that the relay is equipped with at least two antennas. The scenario involved two stations, a base station and a mobile station, exchanging messages through the relay. The dissertation explores how the availability of multiple antennas in the relay can be utilized in the broadcast phase to ensure performance comparable to or better than network coding, while eliminating the constraint of equal transport block sizes for the two messages. Simulation results demonstrated that the proposed MRT consistently outperforms three well-known MU-MIMO precoders such as ZFBF, BDBF and MU-BDBF across all antenna configurations and SNR ranges. Compared to the network coding solution, the target BLER in the range of 10^{-2} to 10^{-3} - sufficient for satisfactory system performance - was achieved at lower or similar SNR values for all configurations except the 4×4 setup, where MRT was worse by 1 dB. However, since the proposed precoding scheme combines messages at the physical layer rather than at the transport layer (as network coding does), the transport channel processing for the two data blocks remains separate and independent, allowing for flexible selection of the modulation and coding scheme for each link.

Antijamming strategies are explored in Chapter 5 where two schemes are verified for the SSA-based MIMO Y channel with a single antenna jammer. The MIMO Y channel involved three users, each sending two messages to the others. In the presence of the jammer, transmission was completely interrupted as the high BLER level persisted throughout the entire range of simulated SNR values. Introduction of the

novel AJ-SSA precoding allowed for successful transmission by effectively eliminating the jammer's interference. Compared to the regular SSA scheme with the interference cancelation receiver (J-IC), the AJ-SSA scheme provided similar performance but at significantly lower computational complexity.

In summary, in the opinion of the author, **the novel concepts, schemes, detailed solutions, and simulation results presented in this dissertation effectively address the challenges outlined in Section 1.1 and validate the theses of this dissertation stated in Section 1.2**.

Appendix A

List of publications

Please note that in earlier publications, the author used her maiden name, which was Ratajczak.

A.1 Conference Articles

1. K. Lenarska, K. Wesołowski, M. Sybis, "Application of Virtual Leaders in Long Vehicle Platoons Operating with Cooperative Adaptive Cruise Control Using IEEE 802.11p Transmission", IEEE 21st International Symposium on "A World of Wireless, Mobile and Multimedia Networks" (WoWMoM) 2020, IEEE, 2020 - s. 176-178, DOI 10.1109/WoWMoM49955.2020.00040

2. K. Lenarska, M. Sybis, P. Sroka, M. Rodziewicz, A. Langowski, K. Wesołowski, „Wprowadzenie wirtualnych liderów w celu wydłużenia długości konwoju pojazdów w systemie 802.11p", Przegląd Telekomunikacyjny i Wiadomości Telekomunikacyjne, nr 6/2017, DOI 10.15199/59.2017.6.46

3. M. Rodziewicz, A. Langowski, P. Sroka, M. Sybis, K. Lenarska, K. Wesołowski, "Modelowanie przyspieszenia pojazdów dla symulacji poruszania się konwoju samochodów wykorzystujących kooperacyjny adaptacyjny tempomat oparty na standardzie IEEE 802.11p", Przegląd Telekomunikacyjny i Wiadomości Telekomunikacyjne, nr 6/2017, DOI 10.15199/59.2017.6.47

4. P. Sroka, M. Rodziewicz, M. Sybis, A. Langowski, K. Lenarska, K. Wesołowski, "Szeregowanie transmisji wiadomości BSM w celu poprawy działania kooperacyjnego adaptacyjnego tempomatu", Przegląd Telekomunikacyjny i Wiadomości Telekomunikacyjne, nr 6/2017, DOI 10.15199/59.2017.6.45

5. M. Sybis, M. Rodziewicz, P. Sroka, A. Langowski, K. Lenarska, K. Wesołowski, "Wpływ dokładności pomiarowej czujników pokładowych na zachowanie sterowanego adaptacyjnie konwoju pojazdów", Przegląd Telekomunikacyjny i Wiadomości Telekomunikacyjne, nr 6/2017, DOI 10.15199/59.2017.6.48

6. K. Lenarska, A. Langowski, M. Sybis, K. Wesołowski, „Metody alokacji zasobów w sieciach 5G o wysokiej niezawodności w komunikacji między pojazdami", Przegląd Telekomunikacyjny i Wiadomości Telekomunikacyjne, nr 6/2016, str. 491-494, ISSN 1230-3496

7. P. Sroka, K. Lenarska, A. Langowski, M. Sybis, K. Wesołowski, „Wykorzystanie informacji o stanie kanału transmisyjnego do optymalizacji wykorzystania zasobów radiowych w systemie komunikacji między pojazdami", Przegląd Telekomunikacyjny i Wiadomości Telekomunikacyjne, nr 6/2016, str. 499-502, ISSN 1230-3496

8. M. Sybis, A. Langowski, K. Wesołowski, K. Lenarska, „Porównanie wybranych sposobów kodowania na potrzeby transmisji URC", Przegląd Telekomunikacyjny i Wiadomości Telekomunikacyjne, nr 6/2016, str. 605-608, ISSN 1230-3496

9. K. Ratajczak, "Podwójna transmisja dwukierunkowa przez stację przekaźnikową", Przegląd Telekomunikacyjny i Wiadomości Telekomunikacyjne, nr 8-9/2014, str. 1182-1188, ISSN 1230-3496 (prezentacja referatu podczas Krajowego Sympozjum Telekomunikacji i Teleinformatyki, 3-5 września 2014 w Poznaniu)

10. K. Bąkowski, M. Rodziewicz, K. Ratajczak, "Overview of the MACHINE - a set of software simulation tools for mobile networks evaluation", XVIII Poznańskie Warsztaty Telekomunikacyjne PWT'2014, Poznań, 12 grudnia 2014

11. K. Ratajczak, K. Bąkowski, K. Wesołowski, "Two-way Relaying for 5G Systems - Comparison of Network Coding and MIMO Techniques", IEEE Wireless Communications and Networking Conference, p. 376-381, ISSN 1525-3511

12. K. Bąkowski, K. Ratajczak, "Porównanie kodowania sieciowego z techniką MU-MIMO w transmisji dwukierunkowej przez przekaźnik dla modelu kanału radiowego IMT-Advanced", Przegląd Telekomunikacyjny i Wiadomości Telekomunikacyjne, nr 6/2014, str. 197-200, ISSN 1230-3496

13. K. Bąkowski, K. Ratajczak, "Overview of the LTE link level simulator developed at Poznań University of Technology", XVII Poznańskie Warsztaty Telekomunikacyjne PWT'2013, Poznań, 13 grudnia 2013

14. K. Ratajczak, K. Bąkowski, "Analiza wydajności techniki MU-MIMO w systemie LTE-Advanced dla modelu kanału radiowego IMT-Advanced", Przegląd

Telekomunikacyjny i Wiadomości Telekomunikacyjne, nr 6/2013, str. 258 -261, ISSN 1230-3496

15. K. Ratajczak, Z. Długaszewski, K. Bąkowski, "Odbiornik MIMO dla systemu 3GPP LTE", Przegląd Telekomunikacyjny i Wiadomości Telekomunikacyjne, nr 6/2011, str. 381-384, ISSN 1230-3496

A.2 Journal Articles

1. K. Lenarska, K. Wesołowski, "Antijamming Schemes for the Generalized MIMO Y Channel", Sensors - 2024, vol. 24, iss. 10, s. 3237-1-3237-14, DOI 10.3390/s24103237

2. M. Sybis, V. Vukadinovic, M. Rodziewicz, P. Sroka, A. Langowski, K. Lenarska, K. Wesołowski, "Communication Aspects of a Modified Cooperative Adaptive Cruise Control Algorithm", IEEE Transactions on Intelligent Transportation Systems - 2019, vol. 20, no. 12, s. 4513-4523, DOI 10.1109/TITS.2018.2886883

A.3 Book chapters

1. R. Krenz, K. Lenarska, P. Sroka, M. Sybis, K. Wesołowski, "System łączności o dużej przepływności dla bezzałogowych platform powietrznych działających w środowisku miejskim", Nasze stulecie. Nauka dla obronności - Poznań, Polska, Wydawnictwo Politechniki Poznańskiej, 2018 - s. 323-335

Bibliography

[1] X. Lin. An overview of 5G advanced evolution in 3GPP Release 18. *IEEE Communications Standards Magazine*, 6(3):77–83, 2022.

[2] ITU-R. Framework and overall objectives of the future development of IMT for 2030 and beyond. *https://www.itu.int/rec/R-REC-M.2160-0-202311-I/en*, 2023.

[3] GSMA. The Mobile Economy 2024 report. *https://www.gsma.com/solutions-and-impact/connectivity-for-good/mobile-economy/wp-content/uploads/2024/02/260224-The-Mobile-Economy-2024.pdf*, 2024.

[4] ITU-R. IMT Vision–Framework and overall objectives of the future development of IMT for 2020 and beyond. Technical report, International Telecomunication Union, 2015.

[5] E. Dahlman, S. Parkvall, and J. Skold. *5G NR: The next generation wireless access technology.* Academic Press, 2018.

[6] ITUR WP5D. Minimum requirements related to technical performance for IMT-2020 radio interface (s), 2017.

[7] A. Alexiou. *5G Wireless Technologies.* Institution of Engineering and Technology, 2017.

[8] 3GPP TS 38.211. NR; Physical channels and modulation. 2024.

[9] A. Zaidi, F. Athley, J. Medbo, U. Gustavsson, G. Durisi, and X. Chen. *5G Physical Layer: Principles, Models and Technology Components.* Academic Press, 2018.

[10] 3GPP TS 38.213. NR; Physical layer procedures for control. 2024.

[11] 3GPP TS 38.212. NR; Multiplexing and channel coding. 2024.

[12] T. Richardson and R. Urbanke. *Modern coding theory.* Cambridge University Press, 2008.

[13] T. Cover and A. Gamal. Capacity theorems for the relay channel. *IEEE Transactions on Information Theory*, 25(5):572–584, 1979.

[14] D. P. Acharjya, M. Kalaiselvi Geetha, and S. Sanyal. *Internet of Things: novel advances and envisioned applications*, volume 25. Springer, 2017.

[15] A. Osseiran, J. F. Monserrat, and P. Marsch. *5G mobile and wireless communications technology*. Cambridge University Press, 2016.

[16] C. E. Shannon. Two-way communication channels. In *Proceedings of the Fourth Berkeley Symposium on Mathematical Statistics and Probability, Volume 1: Contributions to the Theory of Statistics*. The Regents of the University of California, 1961.

[17] R. Ahlswede, N. Cai, S.-Y.R. Li, and R. W. Yeung. Network information flow. *IEEE Transactions on Information Theory*, 46(4):1204–1216, 2000.

[18] S. Althunibat, H. Hassan, T. Khattab, and N. Zorba. A new NOMA-based two-way relaying scheme. *IEEE Transactions on Vehicular Technology*, 72(9):12300–12310, 2023.

[19] S. Zhang, S. C. Liew, and P. P. Lam. Physical-layer network coding. In *Proceedings of the 12th Annual International Conference on Mobile Computing and Networking*, pages 358–365, 2006.

[20] S. C. Liew, S. Zhang, and L. Lu. Physical-layer network coding: Tutorial, survey, and beyond. *Physical Communication*, 6:4–42, 2013.

[21] N. Lee, J.-B. Lim, and J. Chun. Degrees of freedom of the MIMO Y channel: Signal space alignment for network coding. *IEEE Transactions on Information Theory*, 56(7):3332–3342, 2010.

[22] K. Wesołowski. Application of MIMO and network coding in two-way relaying applied in LTE. In *21st Annual IEEE International Symposium on Personal, Indoor and Mobile Radio Communications*, pages 619–624. IEEE, 2010.

[23] M. Peng, H. Liu, W. Wang, and H.-H. Chen. Cooperative network coding with MIMO transmission in wireless decode-and-forward relay networks. *IEEE Transactions on Vehicular Technology*, 59(7):3577–3588, 2010.

[24] R. Zhang, Y.-C. Liang, C. C. Chai, and S. Cui. Optimal beamforming for two-way multi-antenna relay channel with analogue network coding. *IEEE Journal on Selected Areas in Communications*, 27(5):699–712, 2009.

[25] R. Wang and M. Tao. Joint source and relay precoding designs for MIMO two-way relaying based on MSE criterion. *IEEE Transactions on Signal Processing*, 60(3):1352–1365, 2011.

[26] D. Xu, Z. Bai, A. Waadt, G. H. Bruck, and P. Jung. Combining MIMO with network coding: A viable means to provide multiplexing and diversity in wireless relay networks. In *2010 IEEE International Conference on Communications*, pages 1–5. IEEE, 2010.

[27] K. Ratajczak and K. Bąkowski. Analiza wydajności techniki MU-MIMO w systemie LTE-Advanced dla modelu kanału radiowego IMT-Advanced. *Przegląd Telekomunikacyjny i Wiadomości Telekomunikacyjne*, (6):258–261, 2013.

[28] K. Ratajczak, K. Bąkowski, and K. Wesolowski. Two-way relaying for 5G systems: Comparison of network coding and MIMO techniques. In *2014 IEEE Wireless Communications and Networking Conference (WCNC)*, pages 376–381. IEEE, 2014.

[29] K. Bąkowski and K. Ratajczak. Porównanie kodowania sieciowego z techniką MU-MIMO w transmisji dwukierunkowej przez przekaźnik dla modelu kanału radiowego IMT-Advanced. *Przegląd Telekomunikacyjny i Wiadomości Telekomunikacyjne*, (6):605–608, 2016.

[30] A. Chockalingam and B. Sundar Rajan. *Large MIMO systems*. Cambridge University Press, 2014.

[31] P. Li, D. Paul, R. Narasimhan, and J. Cioffi. On the distribution of SINR for the MMSE MIMO receiver and performance analysis. *IEEE Transactions on Information Theory*, 52(1):271–286, 2006.

[32] N. Kim, Y. Lee, and H. Park. Performance analysis of MIMO system with linear MMSE receiver. *IEEE Transactions on Wireless Communications*, 7(11):4474, 2008.

[33] R. Corvaja and A. G. Armada. SINR degradation in MIMO-OFDM systems with channel estimation errors and partial phase noise compensation. *IEEE Transactions on Communications*, 58(8):2199–2203, 2010.

[34] E. Eraslan, B. Daneshrad, and C.-Y. Lou. Performance indicator for MIMO MMSE receivers in the presence of channel estimation error. *IEEE Wireless Communications Letters*, 2(2):211–214, 2013.

[35] S. M. Alamouti. A simple transmit diversity technique for wireless communications. *IEEE Journal on Selected Areas in Communications*, 16(8):1451–1458, 1998.

[36] S. Sesia, I. Toufik, and M. Baker. *LTE-the UMTS long term evolution: from theory to practice*. John Wiley & Sons, 2011.

[37] M. Costa. Writing on dirty paper (corresp.). *IEEE Transactions on Information Theory*, 29(3):439–441, 1983.

[38] F. Kaltenberger, M. Kountouris, L. Cardoso, R. Knopp, and D. Gesbert. Capacity of linear multi-user MIMO precoding schemes with measured channel data. In *2008 IEEE 9th Workshop on Signal Processing Advances in Wireless Communications*, pages 580–584. IEEE, 2008.

[39] T. Haustein, C. Von Helmolt, E. Jorswieck, V. Jungnickel, and V. Pohl. Performance of MIMO systems with channel inversion. In *Vehicular Technology Conference. IEEE 55th Vehicular Technology Conference. VTC Spring 2002 (Cat. No. 02CH37367)*, volume 1, pages 35–39. IEEE, 2002.

[40] L.-U. Choi and R. D. Murch. A transmit preprocessing technique for multiuser MIMO systems using a decomposition approach. *IEEE Transactions on Wireless Communications*, 3(1):20–24, 2004.

[41] A. Wiesel, Y. C. Eldar, and S. Shamai. Zero-Forcing precoding and generalized inverses. *IEEE Transactions on Signal Processing*, 56(9):4409–4418, 2008.

[42] F. Wang, Y. Chang, Y. Wang, J. Jin, and D. Yang. Interference suppression based beamforming scheme for LTE downlink MIMO. In *2010 IEEE 72nd Vehicular Technology Conference-Fall*, pages 1–5. IEEE, 2010.

[43] D. J. Love and R. W. Heath. Limited feedback unitary precoding for spatial multiplexing systems. *IEEE Transactions on Information theory*, 51(8):2967–2976, 2005.

[44] 3GPP TS 136 101 V8.15.0. Evolved Universal Terrestrial Radio Access (E-UTRA); User Equipment (UE) radio transmission and reception. *ETSI*, pages 1–171, 2011.

[45] S. A. Jafar and S. Shamai. Degrees of freedom region of the MIMO X channel. *IEEE Transactions on Information Theory*, 54(1):151–170, 2008.

[46] M. Chen and A. Yener. Multiuser two-way relaying for interference limited systems. In *2008 IEEE International Conference on Communications*, pages 3883–3887. IEEE, 2008.

[47] N. Lee and J.-B. Lim. A novel signaling for communication on MIMO Y channel: Signal space alignment for network coding. In *2009 IEEE International Symposium on Information Theory*, pages 2892–2896. IEEE, 2009.

[48] K. Lee, N. Lee, and I. Lee. Feasibility conditions of signal space alignment for network coding on K-user MIMO Y channels. In *2011 IEEE International Conference on Communications (ICC)*, pages 1–5. IEEE, 2011.

[49] Z. Wang, N.and Ding, X. Dai, and A. V. Vasilakos. On generalized MIMO Y channels: Precoding design, mapping, and diversity gain. *IEEE Transactions on Vehicular Technology*, 60(7):3525–3532, 2011.

[50] K. K. Teav, Z. Zhou, and B. Vucetic. Throughput optimization for MIMO Y channels with physical network coding and adaptive modulation. In *2012 IEEE 75th Vehicular Technology Conference (VTC Spring)*, pages 1–5. IEEE, 2012.

[51] K. K. Teav, Z. Zhou, and B. Vucetic. Performance optimization of MIMO Y channels: Interference alignment and signal detection. *IEEE Communications Letters*, 18(1):66–69, 2014.

[52] Q. Li, H. Li, G. Wu, and S. Li. Retrospective Network Coding Alignment over K-User MIMO Y Channel. *IEEE Communications Letters*, 20(3):502–505, 2016.

[53] Q. Li, G. Wu, H. Li, and S. Li. Degrees of freedom of MIMO Y channel with three semi-blind users. In *2016 25th Wireless and Optical Communication Conference (WOCC)*, pages 1–5. IEEE, 2016.

[54] R. Zhou, Z. Li, C. Wu, and C. Williamson. Signal alignment: Enabling physical layer network coding for MIMO networking. *IEEE Transactions on Wireless Communications*, 12(6):3012–3023, 2013.

[55] K. Liu, Z. Xiang, M. Tao, and X. Wang. An efficient beamforming scheme for generalized MIMO two-way X relay channels. In *2013 IEEE International Conference on Communications (ICC)*, pages 5306–5310. IEEE, 2013.

[56] K. Liu, M. Tao, Z. Xiang, and X. Long. Generalized signal alignment for MIMO two-way X relay channels. In *2014 IEEE International Conference on Communications (ICC)*, pages 4436–4441. IEEE, 2014.

[57] K. Liu, M. Tao, and D. Yang. Generalized signal alignment for arbitrary MIMO two-way relay channels. In *2014 IEEE Global Communications Conference*, pages 1661–1666. IEEE, 2014.

[58] K. Liu and M. Tao. Generalized signal alignment: On the achievable DoF for multi-user MIMO two-way relay channels. *IEEE Transactions on Information Theory*, 61(6):3365–3386, 2015.

[59] W. Long, H. Gao, and T. Lv. Asymmetric signal space alignment for multi-pair two-way relaying network. In *2014 IEEE International Conference on Communications Workshops (ICC)*, pages 308–313. IEEE, 2014.

[60] S. S. Ali, D. Castanheira, A. Silva, and A. Gameiro. Joint signal alignment and physical network coding for heterogeneous networks. In *2016 23rd International Conference on Telecommunications (ICT)*, pages 1–5. IEEE, 2016.

[61] T.-T. Chan and T.-M. Lok. Signal-aligned network coding in interference channels with limited receiver cooperation. In *2018 IEEE/CIC International Conference on Communications in China (ICCC)*, pages 573–577. IEEE, 2018.

[62] T.-T. Chan and T.-M. Lok. Reverse signal-aligned network coding in interference channels with limited transmitter cooperation. In *2018 IEEE International Conference on Signal Processing, Communications and Computing (ICSPCC)*, pages 1–6. IEEE, 2018.

[63] Z. Zhou and B. Vucetic. Beamforming optimization for generalized MIMO Y channels with both multiplexing and diversity. In *2012 IEEE 75th Vehicular Technology Conference (VTC Spring)*, pages 1–5. IEEE, 2012.

[64] Z. Zhou and B. Vucetic. An iterative beamforming optimization algorithm for generalized MIMO Y channels. In *2012 IEEE International Conference on Communications (ICC)*, pages 4595–4599. IEEE, 2012.

[65] W. Xu, Ke. Ma, W. Trappe, and Y. Zhang. Jamming sensor networks: attack and defense strategies. *IEEE Network*, 20(3):41–47, 2006.

[66] K. Pelechrinis, M. Iliofotou, and S. V. Krishnamurthy. Denial of service attacks in wireless networks: The case of jammers. *IEEE Communications Surveys & Tutorials*, 13(2):245–257, 2011.

[67] Y. Zhang and J. Dill. An anti-jamming algorithm using wavelet packet modulated spread spectrum. In *MILCOM 1999. IEEE Military Communications. Conference Proceedings (Cat. No. 99CH36341)*, volume 2, pages 846–850. IEEE, 1999.

[68] C. Popper, M. Strasser, and S. Capkun. Anti-jamming broadcast communication using uncoordinated spread spectrum techniques. *IEEE Journal on Selected Areas in Communications*, 28(5):703–715, 2010.

[69] B. Wang, Y. Wu, K. J. R. Liu, and T. C. Clancy. An anti-jamming stochastic game for cognitive radio networks. *IEEE Journal on Selected Areas in Communications*, 29(4):877–889, 2011.

[70] X. He, H. Dai, and P. Ning. Dynamic adaptive anti-jamming via controlled mobility. *IEEE Transactions on Wireless Communications*, 13(8):4374–4388, 2014.

[71] S. Fang, Y. Liu, and P. Ning. Wireless communications under broadband reactive jamming attacks. *IEEE Transactions on Dependable and Secure Computing*, 13(3):394–408, 2016.

[72] H. Pirayesh and H. Zeng. Jamming attacks and anti-jamming strategies in wireless networks: A comprehensive survey. *IEEE Communications Surveys & Tutorials*, 24(2):767–809, 2022.

[73] J. Guo, N. Zhao, F. R. Yu, M. Li, and V. C. M. Leung. A novel anti-jamming scheme for interference alignment (IA)-based wireless networks. In *2015 IEEE/CIC International Conference on Communications in China (ICCC)*, pages 1–5. IEEE, 2015.

[74] N. Zhao, J. Guo, F. R. Yu, M. Li, and V. C. M. Leung. Antijamming schemes for interference-alignment-based wireless networks. *IEEE Transactions on Vehicular Technology*, 66(2):1271–1283, 2017.

[75] J. Guo, Y. Cao, Z. Yang, N. Zhao, F. R. Yu, Y. Chen, and V. C. M. Leung. Beneficial jamming design for interference alignment networks. In *2017 9th International Conference on Wireless Communications and Signal Processing (WCSP)*, pages 1–6. IEEE, 2017.

[76] N. Kumar and P. M. Pradhan. Development of a minimum interference leakage based interference aligned network in presence of jammers. In *2018 IEEE International Conference on Advanced Networks and Telecommunications Systems (ANTS)*, pages 1–5. IEEE, 2018.

[77] K. Lenarska and K. Wesołowski. Antijamming Schemes for the Generalized MIMO Y Channel. *Sensors*, 24(10):3237, 2024.

[78] Z. Zhou and B. Vucetic. An orthogonal projection optimization algorithm for multi-user MIMO channels. In *2010 IEEE 71st Vehicular Technology Conference*, pages 1–5. IEEE, 2010.

[79] L. Tong and Q. Zhao. Joint order detection and blind channel estimation by least squares smoothing. *IEEE Transactions on Signal Processing*, 47(9):2345–2355, 1999.

[80] A. Scaglione, G. B. Giannakis, and S. Barbarossa. Redundant filterbank precoders and equalizers. II. Blind channel estimation, synchronization, and direct equalization. *IEEE Transactions on Signal Processing*, 47(7):2007–2022, 1999.

[81] D. Darsena, G. Gelli, I. Iudice, and F. Verde. Detection and blind channel estimation for UAV-aided wireless sensor networks in smart cities under mobile jamming attack. *IEEE Internet of Things Journal*, 9(14):11932–11950, 2021.

[82] C. Lu and P. Chen. Robust channel estimation scheme for multi-UAV mmWave MIMO communication with jittering. *Electronics*, 12(9):2102, 2023.

[83] K. Muranov, B. Smida, and N. Devroye. On blind channel estimation in full-duplex wireless relay systems. *IEEE Transactions on Wireless Communications*, 20(7):4685–4701, 2021.

[84] T.-C. Lin and S.-M. Phoong. Blind channel estimation in OFDM-based amplify-and-forward two-way relay networks. In *2016 IEEE International Conference on Acoustics, Speech and Signal Processing (ICASSP)*, pages 3816–3820. IEEE, 2016.

[85] C. W. Chiong, Y. Rong, and Y. Xiang. Blind estimation of MIMO relay channels. In *2014 IEEE Workshop on Statistical Signal Processing (SSP)*, pages 400–403. IEEE, 2014.

List of Figures